Fakultät für Physik
Technische Universität München

DISSERTATION

3D Nonlinear Magnetohydrodynamic Simulations of Macroscopic Internal Instabilities in Tokamak Plasmas

Isabel Krebs

Research conducted at
Max-Planck-Institut für Plasmaphysik
Princeton Plasma Physics Laboratory

Technische Universität München
Fakultät für Physik
Max-Planck-Institut für Plasmaphysik

3D Nonlinear Magnetohydrodynamic Simulations of Macroscopic Internal Instabilities in Tokamak Plasmas

Isabel Krebs

Vollständiger Abdruck der von der Fakultät für Physik der Technischen Universität München zur Erlangung des akademischen Grades eines Doktors der Naturwissenschaften (Dr. rer. nat.) genehmigten Dissertation.

Vositzende/-r: Prof. Dr. W. Petry

Prüfende der Dissertation:

1. Hon.-Prof. Dr. S. Günter
2. Prof. Dr. K. Krischer

Die Dissertation wurde am 1. Juni 2017 bei der Technischen Universität München eingereicht und durch die Fakultät für Physik am 8. August 2017 angenommen.

Abstract

The Hybrid tokamak scenario provides favorable confinement and stability properties and is a candidate for an ITER Advanced tokamak scenario. It is characterized by low magnetic shear and a value of the safety factor (q) close to unity in the plasma core resulting in the absence of sawteeth. As transport calculations for some Hybrid discharges predict that the applied heat and current sources drive the value of q on axis below unity, there seems to be an unexplained mechanism which leads to a redistribution of the toroidal current density such that $q \approx 1$ is maintained in the center of the discharge. This mechanism is referred to as magnetic flux pumping. Besides the advantageous effect of preventing sawtoothing which also prevents the seeding of neoclassical tearing modes by sawteeth, magnetic flux pumping as well facilitates the drive of plasma current through external current sources. As the current density is automatically redistributed, current sources can be applied in the plasma center, where they are most efficient.

The aim of this work is to contribute to the understanding of magnetic flux pumping in Hybrid discharges. As described in [1], a flux pumping mechanism is found in 3D non-linear MHD simulations leading to stationary states with a helically perturbed core and a flat central safety factor profile with values close to unity. It is proposed in [1] that the main effect responsible for this flux pumping mechanism is that the magnetic field and velocity perturbations resulting from a saturated quasi-interchange instability combine to generate an effective negative loop voltage via a dynamo effect. In this thesis, a large set of long-term 3D nonlinear single-fluid MHD simulations in toroidal geometry are presented which have been performed by means of the high-order finite element code M3D-C^1. The simulations result in asymptotic states that either exhibit sawtooth-like reconnection cycles, or correspond to sawtooth-free stationary states where the central safety factor is kept from decreasing below unity by flux pumping. A detailed analysis of this flux pumping mechanism is presented,

and it is discussed under which conditions the mechanism is able to sustain itself. This includes a linear stability analysis of an equilibrium with low central magnetic shear and a central $q \approx 1$. Furthermore, a step towards more realistic simulations of Hybrid discharges has been made by performing 3D nonlinear MHD simulations based on ASDEX Upgrade geometry in which some features of the current ramp-up phase in realistic Hybrid discharges are imitated.

Although in the framework of single-fluid MHD and with the used parameters it is not expected that all features of realistic sawtooth cycles are reproduced, the reconnection events obtained in the simulations share some of their characteristics and two interesting phenomena are found for specific sets of parameters. First, in some cases, the reconnection process during these sawtooth-like events does not complete but stops and reverses. And second, in one case the sawtooth-like reconnection events are separated by quiescent phases showing similar characteristics as the sawtooth-free stationary states.

Zusammenfassung

Das Hybrid-Tokamak-Szenario verfügt über gute Einschluss- und Stabilitätseigenschaften und stellt ein mögliches Advanced-Tokamak-Szenario für ITER dar. Das Hybrid-Szenario ist charakterisiert durch niedrige magnetische Verscherung und einen Wert des Sicherheitsfaktors (q) nahe an Eins im Zentrum der Entladung, was zu der Vermeidung von Sägezähnen führt. Transportsimulationen für einige solcher Hybrid-Entladungen sagen voraus, dass der Wert von q an der Achse aufgrund der verwendeten Heiz- und Stromquellen unter Eins absinken sollte. Da dies nicht geschieht, scheint es einen noch nicht erklärten Mechanismus zu geben, der die toroidale Stromdichte im Zentrum so umverteilt, dass dort q ungefähr auf Eins gehalten wird. Dieser Mechanismus wird auch als magnetisches Flux-Pumping bezeichnet. Zusätzlich dazu, dass der Mechanismus zur Vermeidung von Sägezähnen führt und damit auch das Seeding von neoklassischen Tearing-Moden durch Sägezähne verhindert, erleichtert er auch den externen Stromtrieb. Externer Stromtrieb ist am effizientesten, wenn er im Zentrum eingesetzt wird, was durch die automatische Umverteilung der Stromdichte durch das Flux-Pumping ermöglicht wird.

Das Ziel der vorliegenden Arbeit ist es, zu einem verbesserten Verständnis von magnetischem Flux-Pumping in Hybrid-Entladungen beizutragen. Wie in [1] beschrieben, wurde in dreidimensionalen nichtlinearen MHD-Simulationen ein Flux-Pumping-Mechanismus gefunden, der zu stationären Zuständen führt, bei welchen sich im Zentrum des Plasmas eine helikale Störung befindet und der Sicherheitsfaktor Werte nahe Eins annimmt. Die in [1] vorgeschlagene Erklärung für den Mechanismus ist, dass die von einer gesättigten Quasi-Interchange-Instabilität verursachten Störungen des Magnet- und Geschwindigkeitsfeldes über einen Dynamo-Effekt zu einer effektiven negativen Umfangsspannung führen. In der vorliegenden Arbeit werden eine große Anzahl von nichtlinearen Langzeitsimulationen in dreidimensionaler, toroidaler Geometrie diskutiert, die auf dem magnetohydrodynamischen Einflüssigkeitsmodell

basieren und mit Hilfe des Finite-Elemente-Codes M3D-C[1] berechnet wurden. Das Ergebnis der Simulationen sind entweder Zustände, die von wiederkehrenden sägezahnähnlichen Rekonnexionszyklen geprägt sind, oder stationäre, sägezahnfreie Zustände, bei denen der zentrale Wert des Sicherheitsfaktors von magnetischem Flux-Pumping davon abgehalten wird, unter Eins abzusinken. Der Flux-Pumping-Mechanismus wird im Detail analysiert und es wird erläutert, unter welchen Bedingungen der Mechanismus in der Lage ist, sich selbst aufrechtzuerhalten. Dazu wird unter Anderem eine lineare Stabilitätsanalyse eines Gleichgewichts mit niedriger magnetischer Verscherung und einem Wert von $q \approx 1$ im Zentrum diskutiert. Außerdem wurden nichtlineare Simulationen in der Geometrie von ASDEX Upgrade durchgeführt, in welchen einige Merkmale der Stromaufbauphase in realistischen Hybrid-Entladungen nachgeahmt werden. Diese Simulationen stellen einen Schritt auf dem Weg zu realistischeren Simulationen von Hybrid-Entladungen dar.

Auch wenn aufgrund des verwendeten Einflüssigkeitsmodells und der gewählten Parameter nicht zu erwarten ist, dass in den Simulationen alle Merkmale von realistischen Sägezahnzyklen wiedergegeben werden, finden sich doch einige grundsätzliche Eigenschaften von Sägezähnen in den Simulationen wieder. Zudem fielen bei speziellen Kombinationen von Parametern zwei interessante Phänomene auf. Zum einen ist in einigen Fällen der Rekonnexionsprozess nicht vollständig. Das Wachstum der Insel stoppt in diesen Fällen bevor sie den Plasmakern vollständig verdrängt hat, und die Breite der Insel nimmt wieder ab. Zum anderen liegen zwischen den sägezahnähnlichen Zyklen in einer Simulation längere Phasen, die den stationären, sägezahnfreien Zuständen ähneln.

Contents

Chapter 1

Introduction

The sun gains its energy from nuclear fusion reactions in which the difference in mass between the fusing nuclei and the reaction products is released in the form of kinetic energy. In order to harness energy from nuclear fusion on earth, the necessary conditions have to be provided for sufficient fusion reactions to occur in a controllable way. While in the sun, the dominant fusion process is a chain of reactions in which helium is produced from four protons, this process would not be suitable for a nuclear fusion reactor because of its low probability. Instead, a more suitable reaction is fusion of deuterium and tritium. In a nuclear fusion reactor, a large number of fuel atoms at high enough energies so that their nuclei can overcome their mutual repulsion, would have to be confined for a sufficiently long period of time. A confinement configuration which has been very successful on the path towards achieving this goal is the tokamak. In a tokamak, the necessary energy is provided in the form of thermal energy. As a result of the high temperatures, the fuel atoms are ionized and thus constitute a plasma. The plasma particles are confined to a toroidal volume by means of a magnetic field which is set up such that the magnetic field lines helically wind around nested toroidal surfaces. This magnetic field configuration results from a combination of a strong toroidal magnetic field produced by magnetic field coils and a weaker poloidal magnetic field mainly generated by a toroidal electric current inside the plasma which is driven by a transformer.

Over the course of the history of tokamak research, which began in the 1950s, a large number of tokamaks has been built and operated in many different countries. As the confinement time increases with the machine size,

larger and larger tokamaks have been built in order to approach the necessary conditions of a future fusion reactor. The largest tokamaks currently in operation are JET [2] in the UK, DIII-D [3] in the US, ASDEX Upgrade [4] in Germany, EAST [5] in China and KSTAR [6] in South Korea. A tokamak of even larger size, called ITER [7], is currently being built in France by an international collaboration. The main objective of the ITER program is to demonstrate the scientific and technical feasibility of a nuclear fusion reactor. ITER is expected to reach a ratio between power from fusion reactions and external heating power of up to ten, which corresponds to a plasma state close to ignition[1].

In order to maximize the performance of plasma discharges, they have to be optimized to provide good confinement of particles and energy while ensuring macroscopic stability of the plasma equilibrium. This is done by carefully tailoring the magnetic field configuration and adjusting the use of different external heat and current sources leading to the development of different operational scenarios. An important quantity used to characterize the magnetic field configuration in a tokamak is the safety factor which describes the local angle of the magnetic field lines by giving the number of toroidal turns a magnetic field line undergoes during one poloidal turn around the torus. The safety factor is closely related to the radial profile of the toroidal plasma current density, a large current density implying a small value of the safety factor. Note that a detailed as well as extensive discussion of the physics of tokamaks can be found in [8].

Another important feature of an operational scenario alongside its confinement and stability properties is the maximum possible duration of a discharge. As for the standard operation of a tokamak, the plasma current is generated inductively by a transformer, a continuous operation which would be desirable for a commercial fusion reactor is not possible that way. Therefore, methods of driving the plasma current non-inductively are being explored, e.g., external current sources or the enhancement of the bootstrap current, a diffusion-driven current caused by temperature and density gradients due to the toroidal geometry. Scenarios that allow for extended discharge lengths or even steady-state operation by a partly or fully non-inductive generation of the plasma current are referred to as Advanced tokamak scenarios. The study of Advanced sce-

[1]Ignition is reached when the heating necessary to sustain the plasma is provided by the fusion reactions only, without the need for additional external heating.

narios is one of the objectives of the ITER program.

Standard operational scenarios with inductive current drive are characterized by a current density profile that is largest in the center of the plasma. A centrally peaked current density profile leads to a further concentration of current in the plasma center, as in a region with larger current, Ohmic heating is stronger leading to higher temperatures and thus to a lower resistivity which raises the current density even more. This process is intercepted when the central value of the safety factor profile reaches a value below unity which results in the onset of sawteeth, periodic relaxation events in the plasma core in each of which the central temperature and current density profiles are flattened. Sawteeth can have the unfavorable effect of seeding a different kind of instability, so called neoclassical tearing modes [9], which can degrade the confinement and even lead to a disruption of the entire discharge. An example of a high performance standard operational scenario is the H-mode which is characterized by the use of strong additional external heating sources and a transport barrier at the edge of the plasma enhancing the confinement.

In contrast to the standard operational scenarios, Advanced steady-state scenarios are characterized by a current density profile that peaks off the plasma center, leading to a safety factor profile above unity which has a negative slope in the plasma core and then increases towards the plasma edge. This magnetic field configuration yields improved confinement in the region where the safety factor profile has a small or negative slope, which enhances the contribution of the bootstrap current. However, it has not yet been possible to reach performance levels comparable to standard H-mode discharges because Advanced steady-state discharges are more prone to instabilities.

Another kind of Advanced tokamak scenario is the Improved H-mode which allows for extended discharge durations at high performance. It was first found in ASDEX Upgrade and has by now been generated in most large tokamaks. The Improved H-mode became known as the Hybrid scenario as it represents a mode of operation in between the inductive standard H-mode and the fully non-inductive steady-state scenario. It is characterized by a safety factor profile which is flat and has values close to unity in the central region of the plasma, leading to favorable confinement and stability properties. More details on Advanced scenarios, in particular with regard to the preparation of the operation of ITER is given in [10].

Calculations for some Hybrid discharges predict [11–13] that according to

the heat and current sources, the current density profile should centrally peak, leading to a central value of the safety factor below unity and the occurrence of sawteeth. However, an unexplained mechanism, often referred to as magnetic flux pumping, seems to flatten the central current density profile such that the safety factor is clamped to a value close to unity in the plasma core. In order to be able to extrapolate the accessibility and properties of the Hybrid scenario in present-day tokamaks to ITER, it is crucial to understand in detail the mechanism behind magnetic flux pumping. For more information on magnetic flux pumping in Hybrid discharges it is referred to [11–13].

This work is aimed at advancing the understanding of magnetic flux pumping in Hybrid tokamak discharges by means of 3D nonlinear magnetohydrodynamic simulations in toroidal geometry which have been performed using the high-order finite element code M3D-C^1. The magnetohydrodynamic model describes the plasma as a magnetized, electrically conducting fluid and represents a widely used framework for addressing the subjects of equilibrium and stability in tokamak plasmas. The presented simulations are set up such that the central value of the safety factor profile is driven towards values below unity. The resulting evolution of the plasma is either characterized by sawtooth-like periodic relaxation events, or sawteeth are prevented by a flux pumping mechanism that keeps the central value of the safety factor close to unity.

In Chapter 2, an overview of the theoretical background of the presented work as well as a brief description of the M3D-C^1 code are given. A summary of some experimental observations on the sawtooth instability and approaches for its theoretical description as well as a summary of the physics of Hybrid discharges are presented in Chapter 3.

In Chapter 4, it is analyzed in detail how the flux pumping mechanism in the presented simulations works, and under which conditions it sustains itself. In Chapter 5, simulations in ASDEX Upgrade geometry are presented which mimic some features of the set-up of realistic Hybrid discharges and represent a first step on the path towards a more realistic modeling of Hybrid discharges.

Chapter 2

Magnetohydrodynamics

2.1 Ideal MHD equations

The ideal magnetohydrodynamic (MHD) equations are given by

$$\frac{\partial \rho}{\partial t} + \nabla \cdot (\rho \mathbf{v}) = 0 \tag{2.1}$$

$$\rho \frac{d\mathbf{v}}{dt} = -\nabla p + \mathbf{J} \times \mathbf{B} \tag{2.2}$$

$$\mathbf{E} + \mathbf{v} \times \mathbf{B} = 0 \tag{2.3}$$

$$\frac{d}{dt}\left(\frac{p}{\rho^{\gamma_0}}\right) = 0 \tag{2.4}$$

complemented by a low-frequency, long-wavelength version of Maxwell's equations

$$\nabla \times \mathbf{E} = -\frac{\partial \mathbf{B}}{\partial t} \tag{2.5}$$

$$\nabla \times \mathbf{B} = \mu_0 \mathbf{J} \tag{2.6}$$

$$\nabla \cdot \mathbf{B} = 0\,. \tag{2.7}$$

Here, ρ describes the mass density, $\mathbf{v}$ the fluid velocity, $\mathbf{J}$ the electric current density, $\mathbf{B}$ the magnetic field, p the pressure, $\mathbf{E}$ the electric field, $\gamma_0 = 5/3$ is the ratio of specific heats, μ_0 is the vacuum permeability and $\frac{d}{dt}$ stands for the convective derivative $(\frac{\partial}{\partial t} + \mathbf{v} \cdot \nabla)$. A detailed description and derivation of this model are, for example, presented in [14, 15] which are the references this section is based on.

The MHD model consists of an equation describing the conservation of

mass (2.1), the force balance equation (2.2) giving the time evolution of momentum, Ohm's law (2.3) and the adiabatic equation of state (2.4). Ohm's law combined with Faraday's law (2.5) yields the time evolution of the magnetic field. Note that by using Equation (2.1), the adiabatic equation (2.4) can be rewritten as

$$\frac{3}{2}n\frac{\partial T}{\partial t} + \frac{3}{2}n\mathbf{v}\cdot\nabla T + nT\nabla\cdot\mathbf{v} = 0\,, \tag{2.8}$$

where n is the particle density and T is the temperature. This equation is often called energy equation.

The ideal MHD model describes a magnetized perfectly conducting fluid. One of its important applications is the study of macroscopic equilibrium and stability of plasmas in nuclear fusion devices that use magnetic confinement. Within the wide range of time scales that need to be accounted for in the theoretical treatment of these plasmas, the MHD model covers an intermediate regime. It neither includes high-frequency microscopic effects nor low-frequency transport phenomena.

Equations (2.1)-(2.7) can be derived starting from the original set of Maxwell's equations together with the first three moments of the Boltzmann equation for ions and for electrons as described in [14]. Equation (2.1) follows from the zeroth moment equation for ions, Equations (2.2) and (2.3) result from combinations of the first order moments for ions and electrons, and the sum of the second order moments for ions and electrons leads to Equation (2.4). Note that in terms of the corresponding quantities referring to the ions and the electrons, the single-fluid variables used here are defined as

$$n = n_i = n_e \tag{2.9}$$

$$\rho = m_i n \tag{2.10}$$

$$T = \frac{1}{2}(T_e + T_i) \tag{2.11}$$

$$p = 2nk_BT = p_e + p_i \tag{2.12}$$

$$\mathbf{v} = \mathbf{v}_i \tag{2.13}$$

$$\mathbf{J} = en\left(\mathbf{v}_i - \mathbf{v}_e\right)\,. \tag{2.14}$$

These equations imply that $m_e \ll m_i$ and that quasi-neutrality ($n_i = n_e$) is assumed. Note that $T_e = T_i$ and $p_e = p_i$ for the single-fluid MHD model to

be valid. m_i and m_e denote the ion and electron masses, k_B is the Boltzmann constant and e the electron charge.

The derivation of the ideal MHD model involves the following assumptions which represent the conditions under which the model is valid:

(1) *High collisionality.* This means that on the time scales of interest, both ions and electrons undergo sufficient collisions so that their distribution function is nearly Maxwellian. Furthermore, their mean free path has to be much shorter than the characteristic length scale of the system, and the energy equilibration time has to be short compared to the characteristic time scale so that $T_i \approx T_e$.

(2) *Small gyro radius.* The ion gyro radius has to be much smaller than the characteristic length scale.

(3) *Small resistivity.* Despite the high collisionality, the resistive diffusion time has to be large compared to the characteristic time scale.

For typical plasmas in nuclear fusion devices, conditions (2) and (3) are satisfied. For the requirement of high collisionality this is not in general the case. However, it can be shown that the equation for mass conservation, Ohm's law and the component of the momentum equation that is perpendicular to the magnetic field lines are valid without this condition and that the parallel component of the momentum equation as well as the energy equation do not play an important role if the plasma motion is incompressible, i.e. $\nabla \cdot \mathbf{v} = 0$, which is usually the case for problems involving MHD equilibrium and stability.

It can be shown that the ideal MHD model conserves mass, momentum, energy and magnetic flux. The latter is defined by

$$\psi = \int \mathbf{B} \cdot d\mathbf{A}\,, \tag{2.15}$$

where $d\mathbf{A}$ denotes a surface element. Conservation of magnetic flux means that the amount of flux passing through an arbitrary open surface which moves along with the fluid is constant. As this also applies to the cross section of an arbitrarily thin flux tube enclosing a single magnetic field line, it follows that magnetic field lines are not allowed to cross, tear and reconnect. At the same time, the magnetic field lines are constrained to move with the fluid, so ideal MHD only allows for fluid motions that conserve the topology of the magnetic field lines. This is called the *frozen-in condition.* The inclusion of non-ideal effects into Ohm's law makes it possible that this constraint can

be violated which can have important implications for the stability of plasma configurations as will be discussed in the following section.

2.2 Magnetic reconnection

The model that has been used for the calculations presented in this work includes non-ideal dissipative terms. Including the effect of resistivity, Ohm's law (2.3) becomes

$$\mathbf{E} + \mathbf{v} \times \mathbf{B} = \eta \mathbf{J} \,. \tag{2.16}$$

In order to discuss the effect of a finite resistivity, the time evolution equation for the magnetic field is examined in more detail. Inserting Ohm's law (2.16) into Faraday's law (2.5) yields

$$\frac{\partial \mathbf{B}}{\partial t} = \nabla \times (\mathbf{v} \times \mathbf{B}) - \nabla \times (\eta \mathbf{J}) \,. \tag{2.17}$$

Using Equation (2.6) to eliminate the current density leads to

$$\frac{\partial \mathbf{B}}{\partial t} = \nabla \times (\mathbf{v} \times \mathbf{B}) + \frac{\eta}{\mu_0} \nabla^2 \mathbf{B} \,, \tag{2.18}$$

where it has been used that $\nabla \cdot \mathbf{B} = 0$ and η has been assumed to be spatially constant for simplicity. From the second term on the right side of Equation (2.18), it can be seen that η/μ_0 has the role of a diffusion coefficient for the magnetic field. Magnetic diffusion allows for a violation of the frozen-in condition. However, the magnetic diffusion in the plasma core of modern tokamaks is very small. Typically, η/μ_0 has values in the order of $10^{-3}\mathrm{m}^2/\mathrm{s}$. For typical length scales of 1m, this gives a diffusion time scale of about 10^3s. As MHD instabilities in tokamaks occur on a much shorter time scale, magnetic diffusion seems to be too slow to have any impact on these processes.

However, in the presence of large gradients, significantly smaller length scales have to be considered, so that magnetic diffusion can become important locally. It then allows for *magnetic reconnection* which means that magnetic field lines that are close can tear and reconnect in a different configuration as sketched in Figure 2.1. This localized process can have an important impact on the global configuration of the magnetic field as it allows the magnetic field to

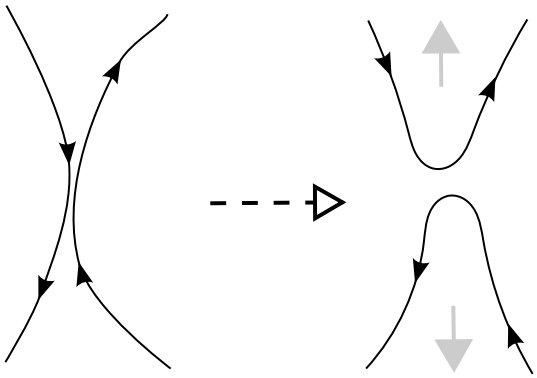

Figure 2.1: Sketch of two reconnecting magnetic field lines. The grey arrows indicate the direction into which the plasma is accelerated. Based on Figures 1.1 and 4.3 in [16].

relax to a lower energy state which would not be accessible without resistivity. As, globally, the frozen-in condition is still valid, the plasma is accelerated by the motion of the magnetic field, leading to a conversion of magnetic energy into kinetic energy.

It should be mentioned that there are also other non-ideal terms that can lead to magnetic reconnection. Those appear in Ohm's law in more complete models than the resistive MHD model as, for example, the two-fluid model where the ion and the electron fluid are treated separately. Such effects can become important and have to be taken into account in cases where the resistivity is very small. More precisely, this is the case if the width of a resistive current sheet becomes smaller than the microscopic length scales of single particle motion which is not included into the MHD model. In fact, this is also true for the plasma core of modern tokamaks as discussed in Section 3.1.3. The discussion presented in this section is based on [17] and [16].

2.3 Dynamos

The first term on the right side of Equation (2.18) indicates that there might be a possibility that a certain velocity field is able to sustain the magnetic field against the resistive decay or even amplify it. The study of amplification of magnetic fields by motions in conducting fluids is the subject of *dynamo theory*. It has its most important applications in the field of astrophysics as dynamos are believed to be responsible for the sustainment of magnetic fields in many astrophysical objects like planets, stars or galaxies. An introduction

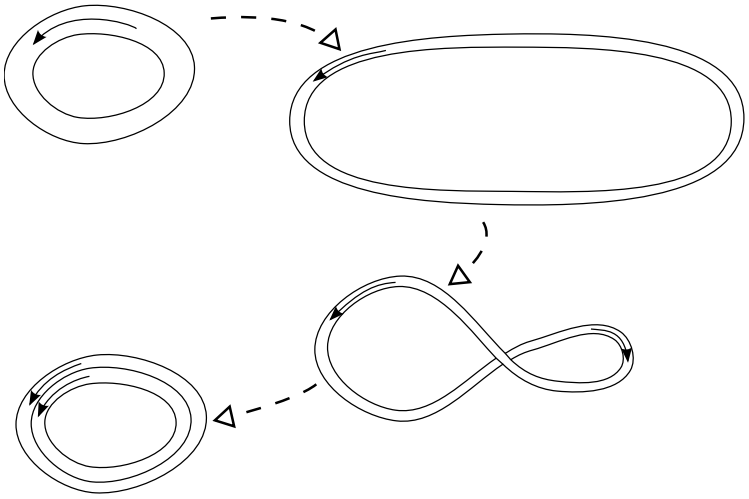

Figure 2.2: Sketch of the rope dynamo. Based on Figure 5.4 in [16].

into dynamo theory is given in [16] which is the reference this section is based on.

The essential idea of how a flow could amplify a magnetic field is illustrated by the rope dynamo [18]. In this model, a closed flux tube is considered. As sketched in Figure 2.2 the flux tube is stretched such that its length is doubled and its cross section is reduced to half of its original value, then it is twisted and folded. The resulting flux tube has the same length and cross section as the original one, but carries twice the amount of magnetic flux.

In kinematic dynamo theory, which is the simplest level dynamo theory, only the equation for the evolution of the magnetic field (2.18) is considered and the velocity field is given, which means that any back reaction of the magnetic field evolution onto the velocity field is neglected. It is examined which kind of flows are needed to sustain different magnetic fields. A series of so called anti-dynamo theorems were developed that proved that a dynamo is not possible in certain configurations. For example, it has been proven that a steady-state axisymmetric magnetic field cannot be maintained via a dynamo action [19]. The same is true for a plane 2D geometry [16], but it is not true for more general geometries with one ignorable coordinate such as helical symmetry for which a dynamo solution has been explicitly calculated [20].

2.4 Tokamak equilibrium configuration

Omitting time-dependent terms and setting $\mathbf{v} = 0$ in Equations (2.1)-(2.7), yields the set of equations that describe a static ideal MHD equilibrium:

$$\nabla p = \mathbf{J} \times \mathbf{B} \tag{2.19}$$

$$\nabla \times \mathbf{B} = \mu_0 \mathbf{J} \tag{2.20}$$

$$\nabla \cdot \mathbf{B} = 0\,. \tag{2.21}$$

In an equilibrium state, the magnetic force $\mathbf{J} \times \mathbf{B}$ balances the pressure gradient force ∇p. This section is based on [14], where an extensive discussion of ideal MHD equilibrium theory can be found.

For a nuclear fusion device using magnetic confinement, an equilibrium configuration is needed that provides good particle and energy confinement properties as well as macroscopic stability. The motion of charged particles perpendicular to the magnetic field is restricted to a gyration by the Lorentz force, but along the magnetic field lines the particles can move freely. Thus, the condition of good confinement leads to toroidal configurations where all of the magnetic field lines inside a certain toroidal domain remain inside this domain. The *tokamak* is the most commonly realized toroidal plasma confinement configuration. It is characterized by axisymmetry.

The tokamak geometry is usually described in cylindrical coordinates (R, ϕ, Z) where R is referred to as the major radius and ϕ is the toroidal angle. To describe a cross section of the torus at a fixed toroidal angle in cases when this cross section is circular, the minor radius r and the poloidal angle θ are often used. The coordinate systems are shown in Figure 2.3. By axisymmetry it is meant that scalar quantities do not depend on ϕ.

The ratio of the major radius of the center of the plasma column R_0 and the minor radius of its boundary a is called the *aspect ratio*. The larger it is, the closer the geometry is to the geometry of a periodic cylinder which is often used as an approximation.

The basic set-up of a tokamak is depicted in Figure 2.4. The main component of the magnetic field is the toroidal field generated by the toroidal field coils. A solely toroidal magnetic field cannot maintain the plasma in a toroidal equilibrium as the inhomogeneous magnetic field leads to a drift motion of the plasma particles in Z-direction that separates ions from electrons and the re-

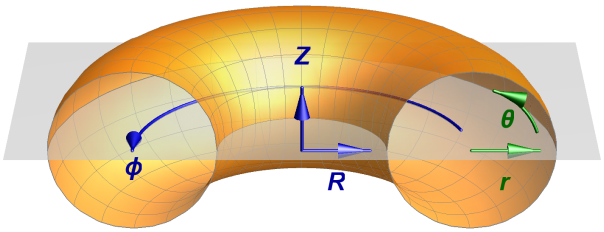

Figure 2.3: Cylindrical coordinates R, ϕ and Z (blue), and additional poloidal coordinates r and θ (green).

sulting electric field leads to an outward motion of the entire plasma [15]. This is prevented by adding a poloidal magnetic field which is mainly generated by a toroidal electric current inside the plasma. The current is driven by a toroidal loop voltage induced by a transformer. The outer poloidal field coils which are necessary to control the plasma shape and position, provide an additional small contribution to the poloidal magnetic field.

The superposition of the toroidal and the poloidal magnetic field results in magnetic field lines that wind helically around the torus. From axisymmetry, it follows that they span nested toroidal surfaces, called *magnetic flux surfaces*. These surfaces are also surfaces of constant pressure and the same surfaces are spanned by $\mathbf{J}$, as can be seen from

$$\mathbf{B} \cdot \nabla p = 0 \quad \text{and} \tag{2.22}$$

$$\mathbf{J} \cdot \nabla p = 0\,, \tag{2.23}$$

which result from Equation (2.19). The innermost magnetic flux surface reduces to a line and is called *magnetic axis*. In modern tokamaks the last closed magnetic flux surface is defined by the magnetic field configuration itself rather than by a solid surface touching the plasma. It is then called *separatrix*. In these configurations, the plasma cross section (at constant ϕ) is usually not circular, but can have different shapes which are typically vertically elongated.

Two quantities that are often used to label the flux surfaces are the *poloidal*

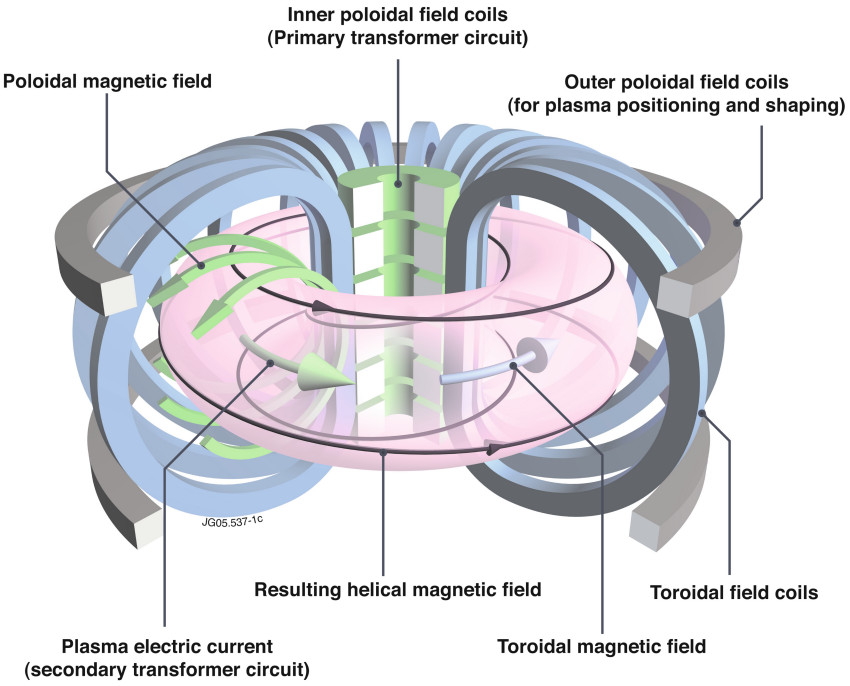

Figure 2.4: Basic set-up of a tokamak. Source: EUROfusion.

magnetic flux ψ_p and the *toroidal magnetic flux* ψ_t defined as

$$\psi_p = \int \mathbf{B} \cdot d\mathbf{A}_p \tag{2.24}$$

$$\psi_t = \int \mathbf{B} \cdot d\mathbf{A}_t \tag{2.25}$$

where the area $\mathbf{A}_p$ is a ribbon spanned between the magnetic axis and a cut through a chosen flux surface at constant θ, and the area $\mathbf{A}_t$ is the area inside a chosen flux surface at constant ϕ. Note that in the remainder of this work the quantities $\Psi = \psi_p/2\pi$ and $\Phi = \psi_t/2\pi$ are referred to as poloidal and toroidal magnetic flux, respectively.

In the case of toroidal axisymmetry, the ideal MHD equilibrium equations (2.19)-(2.21) can be reduced to a two-dimensional, nonlinear, elliptic partial differential equation, called *Grad-Shafranov equation*. To this end, the magnetic field is expressed in terms of Ψ as

$$\mathbf{B} = B_\phi \hat{\phi} + \frac{1}{R} \nabla \Psi \times \hat{\phi} \,. \tag{2.26}$$

Note that Ψ has the role of a stream function for the poloidal magnetic field.

Inserting this expression into Equation (2.20) yields

$$\mathbf{J} = -\frac{1}{\mu_0 R}\Delta^*\Psi\hat{\phi} + \frac{1}{\mu_0 R}\nabla\left(RB_\phi\right) \times \hat{\phi}\,, \tag{2.27}$$

where Δ^* is defined as

$$\Delta^*\Psi = R^2\nabla\cdot\left(\frac{1}{R^2}\nabla\Psi\right)\,. \tag{2.28}$$

The components of Equation (2.19) in the direction of $\mathbf{B}$ and $\mathbf{J}$ imply that both p and RB_ϕ are constant on flux surfaces so that they can be expressed as $p(\Psi)$ and $F(\Psi)$, where

$$F\left(\Psi\right) = RB_\phi\,. \tag{2.29}$$

Inserting Equations (2.26), (2.27) and (2.29) into the component of Equation (2.19) which is perpendicular to the flux surfaces, $\nabla\Psi\cdot[\nabla p = \mathbf{J}\times\mathbf{B}]$, yields the Grad-Shafranov equation

$$\Delta^*\Psi = -\mu_0 R^2\frac{dp}{d\Psi} - F\frac{dF}{d\Psi}\,. \tag{2.30}$$

A specific equilibrium configuration is determined by the choice of $p(\Psi)$, $F(\Psi)$ and the boundary conditions.

2.5 Magnetic field structure in tokamaks

As described in the previous section, in a tokamak configuration the magnetic field lines wind helically around the torus on nested toroidal surfaces. The number of times the field lines on a specific surface turn around the torus toroidally during one poloidal turn is given by the *safety factor*

$$q = \frac{\Delta\phi}{2\pi}\,. \tag{2.31}$$

If the value of the safety factor on the surface is rational, i.e. $q = m/n$, a field line in this surface closes on itself after m toroidal turns and n poloidal turns. If q is irrational, the field line never closes. Assuming a circular cross section,

the *magnetic shear* s defined as

$$s = \frac{r}{q}\frac{dq}{dr} \tag{2.32}$$

describes how much the inclination angle of the field lines changes between neighboring flux surfaces.

For a large aspect ratio tokamak with circular cross section, the safety factor profile can be approximated by

$$q(r) = \frac{rB_\phi}{R_0 B_\theta} = \frac{2\pi r^2 B_\phi}{\mu_0 I(r) R_0}\,, \tag{2.33}$$

where R_0 is the major radius of the magnetic axis, the total toroidal current inside r is given by

$$I(r) = 2\pi \int_0^r J_\phi\left(r'\right) r' dr'\,, \tag{2.34}$$

and Ampère's law (2.6) has been used to obtain the second expression [8]. This shows that the toroidal current density profile plays an important role in determining the safety factor profile. In particular, the values of the safety factor at the plasma boundary and on the magnetic axis are approximately given by $q_a = 2\pi a^2 B_\phi/(\mu_0 I_{\rm tot} R_0)$ and $q_0 = 2B_\phi/(\mu_0 J_{\phi,0} R_0)$, respectively, where $I_{\rm tot}$ is the total toroidal plasma current and $J_{\phi,0}$ is the toroidal current density on axis.

The magnetic field structure of an axisymmetric equilibrium configuration can be significantly modified by non-axisymmetric perturbations in case of non-vanishing resistivity. Consider a perturbation of the form

$$\boldsymbol{\xi} = \boldsymbol{\xi}(r)\exp\left(im\lambda\right)\,, \tag{2.35}$$

where λ is defined as

$$\lambda = \theta - \frac{n}{m}\phi\,. \tag{2.36}$$

This perturbation is resonant with the magnetic field on the flux surface which is characterized by $q = m/n$. Note that $\hat{\boldsymbol{\lambda}}$ is tangent to this flux surface and is orthogonal to the field lines on the surface as shown in Figure 2.5. The

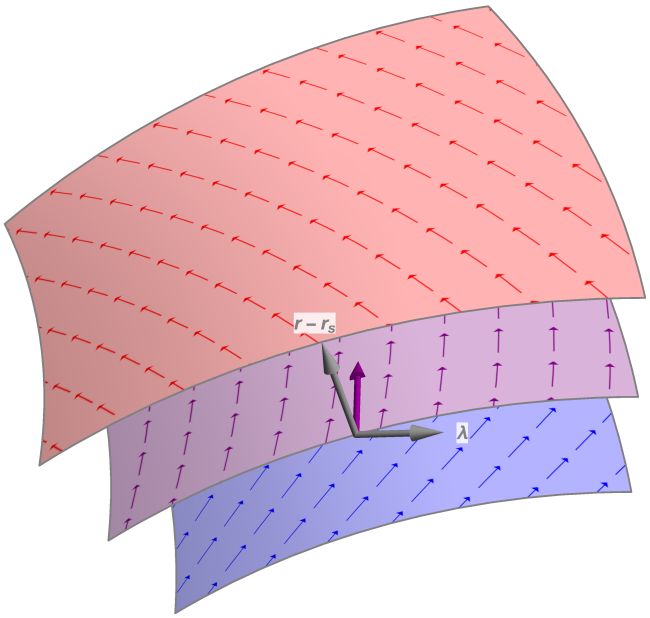

Figure 2.5: A local coordinate system aligned to the magnetic field lines on the resonant surface at radius r_s. Based on Fig. 4.3 in [17].

equilibrium magnetic field along λ is

$$B^* = B_\theta \left(1 - \frac{n}{m} q(r)\right) . \tag{2.37}$$

Thus, B^* vanishes at the resonant surface at $r = r_s$ where $q(r_s) = m/n$, and has a different sign for $r < r_s$ than for $r > r_s$ as illustrated in Figure 2.6. For an ideal plasma, the perturbation $\boldsymbol{\xi}$ would only deform the magnetic field, but resistivity allows the field lines to reconnect yielding a different magnetic topology. A chain of *magnetic islands* is created at the resonant surface where each island consists in nested toroidal surfaces around a magnetic axis and is limited by a separatrix. The island magnetic axis and the crossing lines of the separatrix are called *O-point* and *X-point*, respectively. Note that the island X-points are the sites of reconnection.

The magnetic islands wind helically around the plasma core and close in themselves after m toroidal turns and n poloidal turns. This means that in a plane of constant ϕ there are m magnetic islands. More information about the magnetic field structure in tokamaks and magnetic islands can be found in [17] and [8], which are the references this section is based on.

A special case of magnetic field topology results from a perturbation with

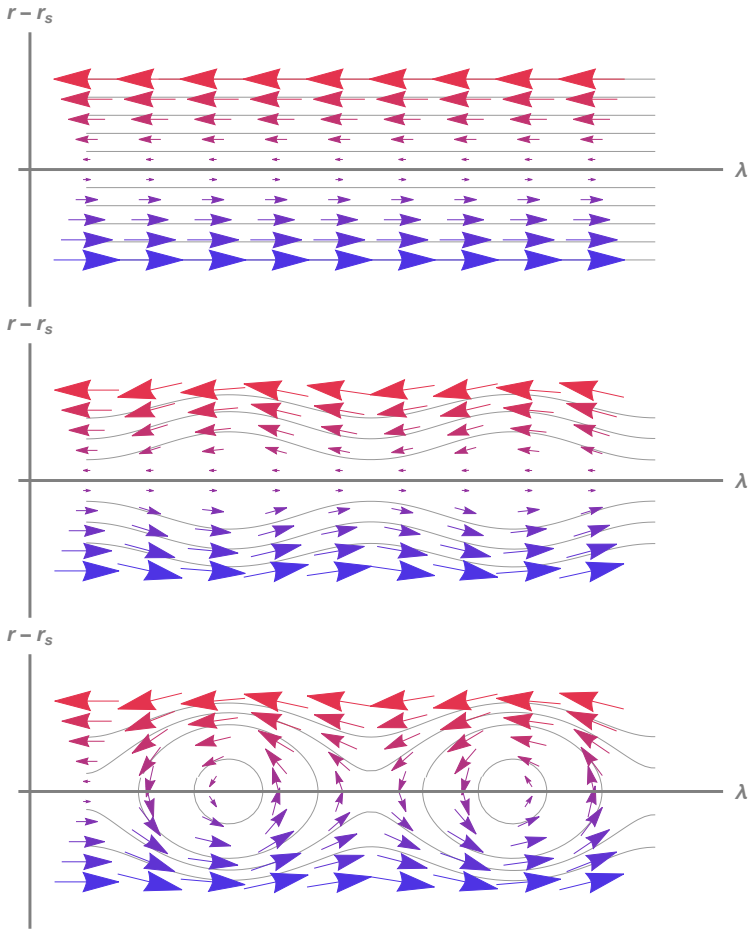

Figure 2.6: *Top*: Illustration of the equilibrium magnetic field configuration in the λ-r plane. On the resonant surface at $r - r_s = 0$, the magnetic field component along λ vanishes. *Center*: A perturbation only compresses the magnetic field if the plasma is ideal. *Bottom*: Resistivity allows for magnetic reconnection leading to the formation of magnetic islands. Based on Fig. 4.4 in [17].

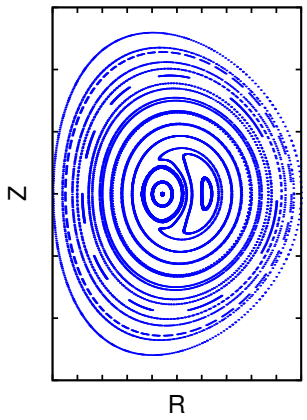

Figure 2.7: Poincaré plot showing a $(m = 1, n = 1)$ magnetic island.

$m = 1$ and $n = 1$. In this case, a single magnetic island winds once around the core. The core and the island have the same topological structure. If the magnetic axis of the island is taken as a reference, the core can be seen as winding helically around the island.

The magnetic field structure can be visualized in *Poincaré plots*. Poincaré plots are generated by tracing field lines on different surfaces and marking the points where the field lines cut a chosen plane. On irrational surfaces the field line will trace out the entire surface after a sufficient amount of toroidal turns. An example of a cut of constant ϕ featuring a $(m = 1, n = 1)$ magnetic island is shown in Figure 2.7.

Field line tracing can also be used to calculate safety factor profiles by counting the number of toroidal and poloidal turns around the magnetic axis the field lines undergo. If, for the calculation of the safety factor profile, field lines are started inside a magnetic island, it results in a flat region where $q = m/n$. This is because relative to the magnetic axis, the island winds around helically as a whole. It does not necessarily mean that the safety factor profile inside the island, calculated with respect to its own magnetic axis, is flat. This becomes important when a safety factor profile in a configuration as the one shown in Figure 2.7 needs to be calculated. The result in the central region of the plasma then depends on which magnetic axis is chosen to be the reference and in which region field lines are started.

A possibility of obtaining an approximation of a safety factor profile in such non-axisymmetric configurations is to toroidally average the magnetic field yielding a configuration of nested magnetic surfaces around a single magnetic

axis before calculating the safety factor profile. This method will be used in this thesis for the magnetic field structures that result from a nonlinear evolution to find out how the axisymmetric field is modified by the perturbations.

2.6 Ideal MHD stability

As mentioned in Section 2.4, for a plasma configuration to be suitable for a nuclear fusion device, it needs to provide good stability properties. Stability means that perturbations result in forces that restore the equilibrium rather than amplifying the initial perturbation. In this section, a framework for studying the linear stability of ideal MHD equilibria will be outlined following the discussion presented in [14]. In doing so, only the most essential steps will be highlighted, for the detailed algebra it is referred to this reference.

The linear analysis of stability represents a useful starting point for a treatment of MHD instabilities as it predicts if an instability will occur at all. For those types of instabilities which need to be entirely avoided, in some cases this information might be all that is needed. Other types of instabilities, like the ones discussed in this thesis, can be tolerated as they do not necessarily lead to an immediate termination of the plasma discharge. Thus, their nonlinear evolution is of interest and needs to be analyzed numerically. However, in these cases, the linear analysis will also provide important insight into the basic characteristics of the instability at its onset.

The analysis presented in this and the following two sections is based on the ideal MHD equations. Including resistivity does not lead to stability when a configuration is ideally unstable, but it can extend the region of instability as it allows for changes of the magnetic topology that would otherwise be prohibited by the frozen-in condition. Resistivity can also play a role during the nonlinear evolution of an ideal instability which is the case for the internal kink instability discussed in Section 2.7.

As mentioned in Section 2.4, a static ideal MHD equilibrium satisfies

$$\nabla p_0 = \mathbf{J}_0 \times \mathbf{B}_0 \tag{2.38}$$

$$\nabla \times \mathbf{B}_0 = \mu_0 \mathbf{J}_0 \tag{2.39}$$

$$\nabla \cdot \mathbf{B}_0 = 0 \tag{2.40}$$

$$\mathbf{v}_0 = 0\,. \tag{2.41}$$

All variables $Q(\mathbf{x}, t)$ are linearized around this equilibrium, so that

$$Q(\mathbf{x}, t) = Q_0(\mathbf{x}) + \tilde{Q}_1(\mathbf{x}, t)\,, \tag{2.42}$$

where $\tilde{Q}_1(\mathbf{x}, t)$ represents a small perturbation. The quantity $\tilde{\boldsymbol{\xi}}$ defined by

$$\frac{\partial \tilde{\boldsymbol{\xi}}}{\partial t} = \tilde{\mathbf{v}}_1 \tag{2.43}$$

is introduced to describe the displacement of the plasma. By inserting the linearized variables into Equations (2.1), (2.4) and Equation (2.5) combined with Equation (2.3), neglecting terms beyond first order, integrating the obtained equations with respect to time, and choosing the initial conditions to be $\tilde{\boldsymbol{\xi}}(\mathbf{x}, 0) = \tilde{\mathbf{B}}_1(\mathbf{x}, 0) = \tilde{\rho}_1(\mathbf{x}, 0) = \tilde{p}_1(\mathbf{x}, 0) = 0$ and $\tilde{\mathbf{v}}_1(\mathbf{x}, 0) \neq 0$, the perturbations $\tilde{\rho}_1$, $\tilde{p}_1$ and $\tilde{\mathbf{B}}_1$ can be expressed in terms of $\tilde{\boldsymbol{\xi}}$. They are then substituted into the linearized version of the momentum equation (2.2) yielding

$$\rho_0 \frac{\partial^2 \tilde{\boldsymbol{\xi}}}{\partial t^2} = \mathbf{F}\left(\tilde{\boldsymbol{\xi}}\right)\,. \tag{2.44}$$

Here, the *force operator* $\mathbf{F}$ is defined as

$$\begin{aligned}\mathbf{F}\left(\tilde{\boldsymbol{\xi}}\right) =& \frac{1}{\mu_0}\left(\nabla \times \mathbf{B}_0\right) \times \left[\nabla \times \left(\tilde{\boldsymbol{\xi}} \times \mathbf{B}_0\right)\right] \\ &+ \frac{1}{\mu_0}\left(\nabla \times \left[\nabla \times \left(\tilde{\boldsymbol{\xi}} \times \mathbf{B}_0\right)\right]\right) \times \mathbf{B}_0 \\ &+ \nabla\left(\tilde{\boldsymbol{\xi}} \cdot \nabla p_0 + \gamma_0 p_0 \nabla \cdot \tilde{\boldsymbol{\xi}}\right)\,,\end{aligned} \tag{2.45}$$

where Equation (2.6) has been used used to eliminate $\mathbf{J}$. The *normal-mode formulation* of the initial value problem given by Equation (2.44) is obtained by separating the time-dependency of $\tilde{\boldsymbol{\xi}}$ by expressing it as

$$\tilde{\boldsymbol{\xi}}(\mathbf{x}, t) = \boldsymbol{\xi}(\mathbf{x}) \exp\left(-i\omega t\right)\,, \tag{2.46}$$

which leads to

$$-\omega^2 \rho_0 \boldsymbol{\xi} = \mathbf{F}\left(\boldsymbol{\xi}\right)\,, \tag{2.47}$$

representing an eigenvalue equation with eigenvalues ω^2 which can be shown to be real. If $\omega^2 < 0$, the perturbation grows exponentially with a growth rate

$\gamma = i\omega$. Otherwise, the system is stable and oscillates around its equilibrium position with the frequency ω.

In order to simplify the analytical treatment of this problem, it is useful to cast it into a variational formulation by multiplying Equation (2.47) with $\boldsymbol{\xi}$ and integrating it over the plasma volume which yields

$$\frac{1}{2}\omega^2 \int \rho_0 \boldsymbol{\xi}^2 \, dV = -\frac{1}{2} \int \boldsymbol{\xi} \cdot \mathbf{F}\left(\boldsymbol{\xi}\right) \, dV \, . \tag{2.48}$$

Here, the left side of the equation represents the kinetic energy of the plasma and the right side corresponds to the potential energy, denoted δW in the following. The latter decides about the stability of the system as $\int \rho_0 \boldsymbol{\xi}^2 \, dV$ is always positive. It can be shown that the system is unstable if some trial function $\boldsymbol{\xi}$ can be found which yields $\delta W < 0$. In this case, the corresponding γ is a lower limit for the growth rate of the actual eigenfunction. This facilitates the linear stability analysis significantly, as it is in general not necessary to determine the exact eigenfunctions in order to prove instability. In the following, expressions for δW in the geometry of interest are presented that allow for efficient analysis and it is discussed under which conditions trial functions can be found that yield $\delta W < 0$, focusing on long-wavelength perturbations that are localized in the plasma core.

An expression for δW can be derived, that splits into a term describing the magnetic field energy in the vacuum region around the plasma, a term describing the contribution of a perturbation of the boundary between the plasma and the vacuum region, and a term δW_F corresponding to the contribution of the plasma volume itself. As this discussion aims at instabilities in the plasma core, only the latter contribution is taken into account in the following. It reads

$$\begin{aligned} \delta W_F =& \frac{1}{2} \int \left[\frac{1}{\mu_0} |\mathbf{Q}_\perp|^2 + \frac{1}{\mu_0} B_0^2 |\nabla \cdot \boldsymbol{\xi}_\perp + 2\boldsymbol{\xi}_\perp \cdot \boldsymbol{\kappa}|^2 + \gamma_0 p_0 |\nabla \cdot \boldsymbol{\xi}|^2 \right] \, dV \\ &+ \frac{1}{2} \int \left[-2 \left(\boldsymbol{\xi}_\perp \cdot \nabla p_0\right) \left(\boldsymbol{\kappa} \cdot \boldsymbol{\xi}_\perp\right) - J_{0,\parallel} \left(\boldsymbol{\xi}_\perp \times \mathbf{b}\right) \cdot \mathbf{Q}_\perp \right] \, dV \end{aligned} \tag{2.49}$$

where the integral is carried out over the plasma volume. Here, $\boldsymbol{\xi} = \boldsymbol{\xi}_\perp + \xi_\parallel \mathbf{b}$, $\mathbf{J}_0 = \mathbf{J}_{0,\perp} + J_{0,\parallel}\mathbf{b}$, $\mathbf{Q} = \mathbf{Q}_\perp + Q_\parallel \mathbf{b}$, where $\mathbf{b} = \mathbf{B}_0 / B_0^2$ and

$$\mathbf{Q} = \mathbf{B}_1 = \nabla \times \left(\boldsymbol{\xi} \times \mathbf{B}_0\right) \, , \tag{2.50}$$

and the curvature of the equilibrium magnetic field is given by

$$\kappa = (\mathbf{b} \cdot \nabla)\, \mathbf{b}\,. \tag{2.51}$$

The first three terms of Equation (2.49) are all positive and thus act stabilizing. From left to right, they correspond to the energy required to bend the magnetic field lines, the energy required for a compression of the magnetic field, and the energy required to compress the plasma. The remaining two terms can become negative and therefore represent possible sources for instabilities. Instabilities that are driven by the term that contains ∇p_0 are called *pressure-driven*, and instabilities that are due to the term that is proportional to $J_{0,\parallel}$ are called *current-driven*. In many cases, instabilities are driven by both the pressure gradient and the parallel current density.

2.7 Internal kink instability

Equation (2.49) gives a general expression for δW_F that does not depend on the geometry. In the following, an expression for δW_F in the geometry of a tokamak plasma with a circular cross section is discussed. The perturbation $\boldsymbol{\xi}$ is written as a component of a Fourier series, yielding

$$\boldsymbol{\xi}(\mathbf{x}) = \boldsymbol{\xi}(r) \exp\left[i\left(m\theta + n\phi\right)\right]\,, \tag{2.52}$$

where m and n are called the poloidal and the toroidal mode number. The large aspect ratio approximation is used, so that the equation for δW_F can be expanded in orders of $\epsilon = a/R_0 \ll 1$. As for tokamaks $q \sim rB_\phi/(R_0 B_\theta) \sim 1$, it follows that $B_\theta/B_\phi \sim \epsilon$. Furthermore, it is assumed that $s \sim 1$, $\beta_p \sim 2\mu_0 p/B_\theta^2 \sim 1$ and the safety factor profile is an increasing function of r. Again, any terms depending on a perturbation of the plasma boundary are neglected. The expansion results in a series of terms of the form

$$\delta W_F = \delta W_0 + \delta W_2 + \delta W_4 + \ldots\,,$$

where $\delta W_n \sim \epsilon^n$. The term δW_0 vanishes and the next term reads

$$\delta W_2 = \frac{2\pi^2 B_{0,\phi}^2}{\mu_0 R_0} \int_0^a \left(\frac{n}{m} - \frac{1}{q}\right)^2 \left[r^2 \left(\frac{d\xi_r}{dr}\right)^2 + \left(m^2 - 1\right)\xi_r^2\right] r\, dr\,. \tag{2.53}$$

Here, ξ_r is the radial component of $\boldsymbol{\xi}$, and the other components have been eliminated using the symmetry of the system. For $m \geq 2$, it is not possible to find a trial function ξ_r that leads to $\delta W_2 \leq 0$, thus the plasma is stable for modes with $m \geq 2$. For $m = 1$, the term proportional to ξ_r^2 vanishes. Hence, choosing a ξ_r that is constant in r would make δW_2 vanish, but this perturbation is not allowed as only modes with $\xi_r(a) = 0$ are considered. As ξ_r has to vanish at the boundary, its derivative has to be non-zero for some radius. This means that if $q_0 > 1$, the system is stable, as in this case the factor $(n/m - 1/q)^2$ never vanishes. This factor represents the stabilizing effect due to the fact that energy is required to bend the field lines. It vanishes for $q = m/n$, i.e. if the perturbation has the same structure as the equilibrium magnetic field.

However, if a $q = 1$ surface exists inside the plasma, a trial function ξ_r can be constructed that avoids the stabilizing effect of field line bending and leads to $\delta W_2 = 0$. This perturbation corresponds to a rigid helical shift of the plasma, where ξ_r is constant inside the $q = 1$ surface and vanishes for $q > 1$. The radial derivative of this trial function has the form of a δ-function vanishing everywhere except at $q = 1$ where $(n/m - 1/q)^2 = 0$. As this leads to $\delta W_2 = 0$, the term of fourth order in ϵ decides about the stability. For $m = n = 1$, a parabolic current density profile and a value of q_0 below, but not too far from unity, δW_4 can be approximated by

$$\delta W_4 \approx \frac{6\pi^2 B_{0,\phi}^2 r_s^4 \xi_0^2}{\mu_0 R_0^3} (1 - q_0) \left(\frac{13}{144} - \beta_{p1}^2 \right) , \tag{2.54}$$

where $\xi_0 = \xi_r(0)$, r_s is the radius of the $q = 1$ surface and β_{p1} is defined as

$$\beta_{p1} = \frac{2\mu_0}{B_{0,\theta}^2} \int_0^{r_s} \left(\frac{r}{r_s} \right)^2 \left(-\frac{dp}{dr} \right) dr \, . \tag{2.55}$$

Hence, the mode with $m = n = 1$ is indeed unstable for sufficiently large values of β_{p1}. The instability is not only driven by the central current density, but also by the pressure gradient inside the resonant surface. Note that the stabilization at low values of β_{p1} is due to the toroidicity and does not arise if the calculation is done for a straight cylinder.

In summary, the linear analysis of the ideal MHD equations in a geometry approximating that of a tokamak plasma predicts an internal instability, if

$q_0 < 1$ (for $s > 0$) and if β is sufficiently large. The unstable mode has a helical structure defined by the mode numbers $m = n = 1$ and radially extends over the region inside the $q = 1$ surface. The displacement corresponds to a helical kinking of the plasma core which is why the instability is called *internal kink*.

During the nonlinear evolution of the internal kink, the displacement of the plasma core leads to large gradients of the magnetic field at the $q = 1$ surface. At this stage, resistivity becomes important as it leads to the formation of a $(m = 1, n = 1)$ magnetic island (see Figure 2.7) through magnetic reconnection. The ideal internal kink instability and its resistive, nonlinear evolution are believed to be responsible for the experimentally observed sawtooth oscillations which will be discussed in Section 3.1.

This section mainly follows the discussion in [14], additional information can be found in [8] and [17]. The original work it is based on is [21].

2.8 Quasi-interchange instability

The analysis that lead to the prediction of the internal kink instability presented in the previous section is based on the assumption of finite magnetic shear. However, a flat central safety factor profile results in a different kind of instability. If the safety factor profile is sufficiently flat inside the $q = 1$ surface, the factor $(1 - 1/q)^2$ in Equation (2.53) (for $m = n = 1$) reduces to the order of ϵ^4. In this case, the separation of the term given by Equation (2.53) from the contributions of order ϵ^4 is not valid any more.

When the stability analysis is carried out taking this into account, a different type of instability is found. It is pressure-driven [22], and the velocity perturbation of the most unstable mode has the form of a convection cell rather than causing a rigid shift like for the internal kink. A comparison between the two is sketched in Figure 2.8.

This can be understood by considering the role of the stabilizing effect of field line bending. Having $q \approx 1$ inside the entire plasma core weakens this effect, so that, in contrast to the internal kink, in this case, it is not so important for the displacement to be exactly constant within the plasma core in order to avoid this stabilizing contribution. The resulting instability is called *quasi-interchange* because the convective motion almost interchanges field lines. In contrast to the internal kink instability, it does not have a threshold with regard to β [22]. This section is based on the discussion of

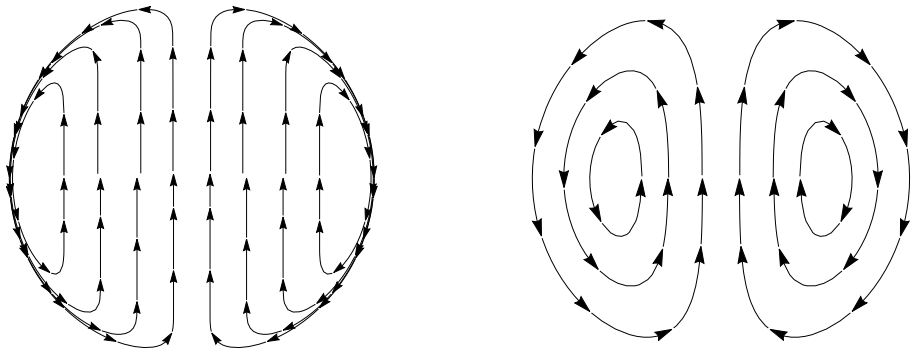

Figure 2.8: Sketch of the velocity perturbation in the r-θ plane for an ideal internal kink instability (left) and for a quasi-interchange instability (right). Based on Figure 6.10.3 in [8].

the quasi-interchange instability in [8]. An analytical linear analysis of the stability of tokamak plasmas with low central magnetic shear and $q_0 \approx 1$ can be found in [22] and [23].

2.9 The M3D-C^1 code

As mentioned before, the analysis of the nonlinear evolution of MHD instabilities requires numerical tools. The numerical simulations presented in this thesis have been performed using the M3D-C^1 code. It is a high-order finite element code that solves the time-dependent nonlinear extended MHD equations [24]. The code uses a split-implicit time advance for long-time integrations allowing for simulations that span the time scales of MHD instabilities as well as those of transport phenomena. It provides a choice of different physics models and geometries. For the simulations presented in this work, the following set of differential equations (here translated into SI units) is solved in

toroidal geometry:

$$\frac{\partial n}{\partial t} + \nabla \cdot (n\mathbf{v}) = d_n \nabla^2 n + S_n \tag{2.56}$$

$$\frac{\partial \mathbf{B}}{\partial t} = -\nabla \times \mathbf{E} \tag{2.57}$$

$$nm_i \left(\frac{\partial \mathbf{v}}{\partial t} + \mathbf{v} \cdot \nabla \mathbf{v} \right) = -\nabla p + \mathbf{J} \times \mathbf{B} + \nu \nabla^2 \mathbf{v} \tag{2.58}$$

$$\begin{aligned} &\frac{3}{2} n \frac{\partial T}{\partial t} + \frac{3}{2} n \mathbf{v} \cdot \nabla T + nT \nabla \cdot \mathbf{v} \\ &\quad = \nu |\nabla \mathbf{v}|^2 + \eta \mathbf{J}^2 + \nabla \cdot \left(\chi_\perp n \nabla T + \chi_\parallel n \frac{\mathbf{BB}}{B^2} \cdot \nabla T \right) + S \,. \end{aligned} \tag{2.59}$$

These equations correspond to Equations (2.1), (2.5), (2.2) and (2.8) with additional terms describing dissipative effects and sources. Momentum diffusion is reflected by the term $\nu \nabla^2 \mathbf{v}$ in the force balance equation, where ν denotes the dynamic viscosity. A heat diffusion term $\nabla \cdot (\chi n \nabla T)$, where χ is a tensor describing the heat diffusivity, is added to the energy equation. As, in tokamak plasmas, the heat transport is significantly different along and across the magnetic field, this term is split into two parts with the scalar coefficients $\chi_\parallel$ and $\chi_\perp$ describing heat diffusion parallel and perpendicular to the magnetic field lines.

The generation of heat by viscous and magnetic dissipation is reflected by additional terms in the energy equation which are $\nu |\nabla \mathbf{v}|^2$ and $\eta \mathbf{J}^2$, respectively. The latter is called *Ohmic heating*. The particle and energy sources are denoted by S_n and S, respectively. The term $d_n \nabla^2 n$ is an additional particle diffusion which provides numerical stability and allows to account for enhanced particle diffusion due to turbulence on microscopic scales not described by the MHD model. The ion mass m_i is set to the mass of a proton for the presented calculations.

The magnetic field, the electric field and the electric current density are defined as

$$\mathbf{B} = \nabla \times \mathbf{A} \tag{2.60}$$

$$\mathbf{E} = -\mathbf{v} \times \mathbf{B} + \eta \mathbf{J} \tag{2.61}$$

$$\mathbf{J} = \frac{1}{\mu_0} \nabla \times \mathbf{B} \,. \tag{2.62}$$

Solving for the magnetic vector potential $\mathbf{A}$ instead of the magnetic field en-

sures that $\nabla \cdot \mathbf{B} = 0$ is automatically satisfied. The magnetic vector potential and the velocity field are represented as

$$\mathbf{A} = R^2 \nabla\phi \times \nabla f + \Psi \nabla\phi - F_0 \ln R\hat{Z} \tag{2.63}$$

$$\mathbf{v} = R_N^2 \nabla U \times \nabla\phi + \omega R^2 \nabla\phi + R_N^{-2} \nabla_\perp \chi \,, \tag{2.64}$$

where f, Ψ, U, ω and χ are scalar fields, and F_0 is a constant. Here, Ψ corresponds to $-\psi_p/2\pi$ and the quantity $F = RB_\phi$ in the Grad-Shafranov equation (2.30) can be recovered as $F = F_0 + R^2 \nabla \cdot \nabla_\perp f$. U is the poloidal velocity stream function, ω corresponds to the toroidal angular velocity and the term involving χ describes the compressible part of the velocity. Cylindrical coordinates (R, ϕ, Z) are used, $R_N = R/R_{\text{axis}}$, $\nabla\phi = \hat{\phi}/R$ and $\nabla_\perp$ acts on a scalar field Q or a vector field $\mathbf{Q}$ as

$$\nabla_\perp Q = \hat{R}\partial_R Q + \hat{Z}\partial_Z Q \quad \text{and} \tag{2.65}$$

$$\nabla_\perp \cdot \mathbf{Q} = \frac{1}{R}\partial_R R\mathbf{Q} \cdot \hat{R} + \partial_Z \mathbf{Q} \cdot \hat{Z} \,, \tag{2.66}$$

respectively. Note that Equation (2.63) implies the gauge condition

$$R^2 \nabla_\perp \cdot \frac{1}{R^2}\mathbf{A} = 0 \,. \tag{2.67}$$

In summary, the quantities that are evolved in time in this model are n, T, U, ω, χ, Ψ and f. Other models that are provided, but have not been used for the simulations presented here, include reduced resistive single-fluid models using different subsets of this set of fields, and a two-fluid model described in [24].

At the beginning of each simulation the Grad-Shafranov equation (2.30) is solved to compute the axisymmetric equilibrium on the provided R-Z grid. The time evolution that follows can either be calculated using the linear, the 2D axisymmetric nonlinear, or the 3D nonlinear version of the code. The 2D nonlinear version does not allow for variations in the toroidal direction. In cases like the ones discussed here, the plasma configuration is stable with respect to $n = 0$ instabilities. This means that the 2D code version can be used to evolve the initial equilibrium to its asymptotic state where the profiles are determined by the diffusion coefficients, sources and the boundary conditions. It is possible to use the 2D nonlinear version first, and later restart the simulation using the 3D nonlinear code version.

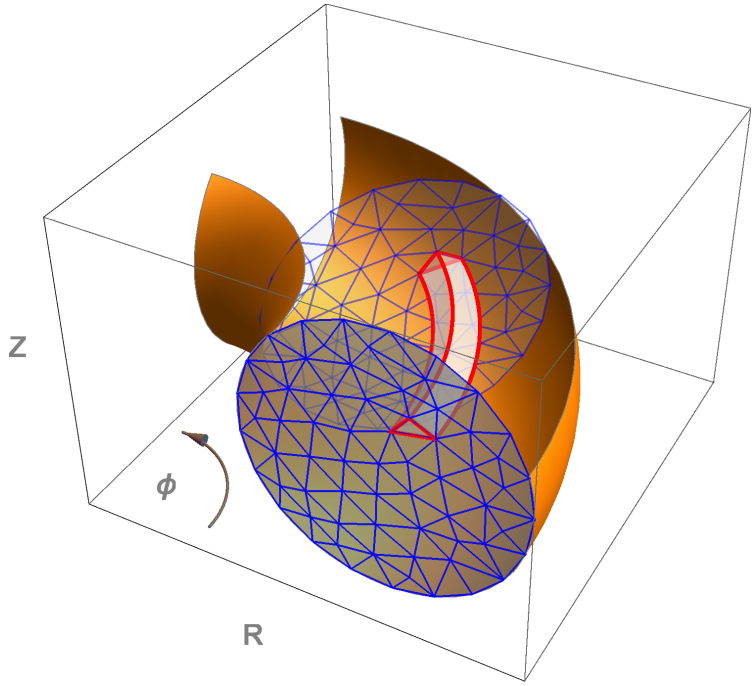

Figure 2.9: A sketch of a triangular wedge element is shown in red.

For the 3D nonlinear version, triangular wedge finite elements as shown in Figure 2.9 are used. They represent a tensor product of reduced quintic triangular elements [25, 26] in the R-Z plane and Hermite cubic elements [27] in the toroidal direction. Both the reduced quintic and the Hermite cubic elements ensure continuity between neighboring wedges not only for the values of the variables, but also for their first derivatives (C^1 continuity). A variable Q is expressed as

$$Q = \sum_{i=1}^{18} \sum_{j=1}^{4} Q_{ij}\, \alpha_i(R, Z)\, \beta_j(\phi)\,, \tag{2.68}$$

where α_i and β_j are the reduced quintic and the Hermite cubic basis functions, respectively. Quintic 2D elements have 21 degrees of freedom, this number has been reduced to 18 by applying constraints resulting from the requirement of C^1 continuity. The remaining degrees of freedom correspond to the value of the variable Q and its derivatives $\partial_R Q$, $\partial_Z Q$, $\partial_R \partial_Z Q$, $\partial_R^2 Q$, $\partial_Z^2 Q$ at each node of a triangle.

For the linear code version, the same triangular elements are used in the R-Z plane, but the dependency on the toroidal angle is described by a single

Fourier mode with a chosen toroidal mode number[1]. In contrast to the 2D and 3D nonlinear code versions, in this case the $n = 0$ background does not change in time.

The mesh in the R-Z plane is unstructured and can be refined locally as shown in Figure 5.1. For the simulations presented here, the boundary of the computational domain coincides with a closed flux surface, but it is as well possible to chose a boundary that lies outside the separatrix. A thick, resistive wall can also be included [29]. More detailed information on the M3D-C^1 code can be found in [24, 30–33].

[1]This decomposition makes use of the fact that other than modes characterized by different poloidal mode numbers m which are coupled by the effect of toroidicity and shaping [28], modes with different toroidal mode numbers n only couple nonlinearly.

Chapter 3

The sawtooth instability and the sawtooth-free Hybrid scenario

3.1 Sawteeth

3.1.1 Experimental observations

Sawteeth are periodic relaxation events in each of which a part of the plasma pressure stored in the core of a tokamak discharge is ejected. First reported in [34], sawteeth have been routinely observed in most tokamak experiments [35]. While they have the beneficial effect of removing impurities from the plasma core, they have also been observed to seed neoclassical tearing modes, an instability that can have a detrimental influence on energy and particle confinement and can even lead to disruptions of the entire plasma [36].

A sawtooth cycle is characterized by three phases. During the *ramp phase* the plasma density and temperature in the center rise slowly. It is usually followed by the *precursor oscillation phase* where a growing $(m = 1, n = 1)$ helical magnetic perturbation is observed in the core region which results in a sinusoidal oscillation of the measured signal due to the rotation of the plasma. Subsequently the central plasma density and temperature suddenly and very quickly drop during what is called the *crash phase*. A typical signature of sawtooth cycles is shown in Figure 3.1. It should be mentioned that also sawteeth without precursor oscillations as well as sawteeth with postcursor oscillations have been observed [37].

In modern, large tokamaks the sawtooth period is usually in the order of $10^{-2}..10^{-1}$ s, e.g. [35, 38–40]. Crash times are typically in the order of 10^{-4} s,

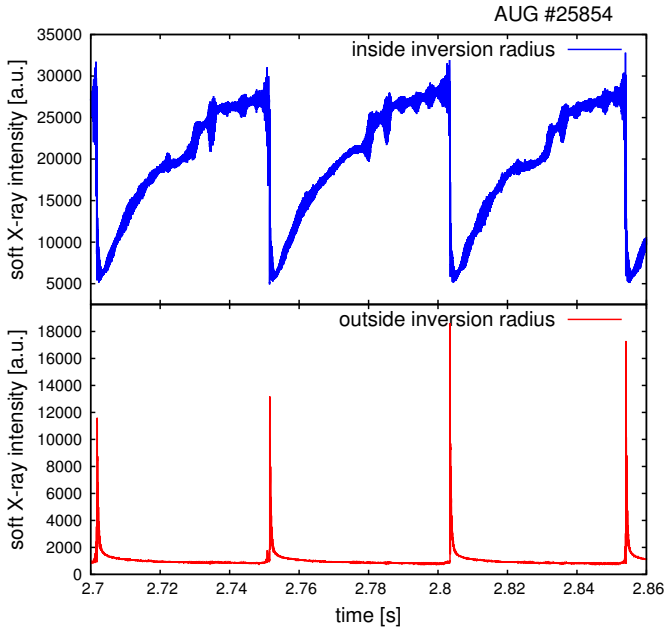

Figure 3.1: Soft X-ray signals measured at radial locations inside and outside the inversion radius during a sawtoothing ASDEX Upgrade discharge. The soft X-ray emission is a measure of a combination of electron temperature and impurity density (in this case mainly tungsten). With kind permission of V. Igochine.

e.g. [39, 41–43] and do not show a strong dependence on resistivity [17].

Further outside the core plasma, the sawtooth signature is inverted, a fast rise of the plasma temperature and density are measured at the time of the crash [34]. The minor radius where the signature changes is called the *inversion radius*. Sawteeth only occur if the value of the safety factor on the magnetic axis is below unity. The inversion radius is found close to the radius of the $q = 1$ surface of the pre-crash safety factor profile [44]. 2D measurements of electron temperature fluctuations for a fixed toroidal angle during sawtooth cycles show that the hot plasma core seems to be expelled through a poloidally localized region [45–47].

As will be discussed in the following sections, a key quantity for the validation of theoretical models put forward to explain the sawtooth instability is the evolution of the central value of the safety factor during sawtooth cycles. The results on this differ. Whereas some measurement results suggest that the current density profile is entirely flattened by the crashes so that the central safety factor becomes unity after a crash, e.g. [48, 49], others indicate that q_0 remains below unity throughout the entire cycle, e.g. [43, 48, 50–52].

A detailed, although somewhat dated, review on the sawtooth instability,

focusing on both experimental observations and theoretical modeling can be found in [35].

3.1.2 Kadomtsev model

While a complete theoretical model of the sawtooth instability has not yet been developed, the description proposed by B.B. Kadomtsev in 1975 [53] is a widely used starting point for attempts to explain the dynamics of sawteeth seen in experiments. The following description of Kadomtsev's model and the discussion in Section 3.1.3 are based on [17] and [35].

The model treats the internal kink instability within the framework of reduced resistive MHD [54, 55] in cylindrical geometry. As discussed in Section 2.7, the internal kink is unstable when the value of the safety factor at the magnetic axis is smaller than unity which corresponds to the experimentally observed occurrence of sawteeth. The resulting growth of a $(m = 1, n = 1)$ magnetic island can explain the experimentally observed precursor oscillation. As the island grows, the core is pushed aside and shrinks, the contained plasma is expelled through the magnetic reconnection site at the X-point of the island. This matches the experimental observation of a poloidally localized heat flux during the crash phase. The reconnection process is complete when the entire positive contribution to the helical magnetic flux Ψ^* is eliminated. The helical magnetic flux is given by

$$\Psi^* = \int_0^r B^*(r')r'\,dr' \tag{3.1}$$

where B^* is defined by Equation (2.37) for $m = n = 1$. The helical flux describes the magnetic flux through a helical ribbon that begins at the magnetic axis and is shaped such that its cut with the $q = 1$ surface corresponds to a magnetic field line on that surface.

After completion of the process the magnetic island has replaced the original plasma core so that axisymmetry is restored. The island O-point has become the new magnetic axis and $q_0 \approx 1$. The configuration does not have a $q = 1$ surface any more and is thus stable with respect to the internal kink. The temperature and density profiles have been flattened as the hot, dense plasma contained inside the original $q = 1$ surface has been expelled and replaced by colder, less dense plasma from inside the magnetic island. This explains the

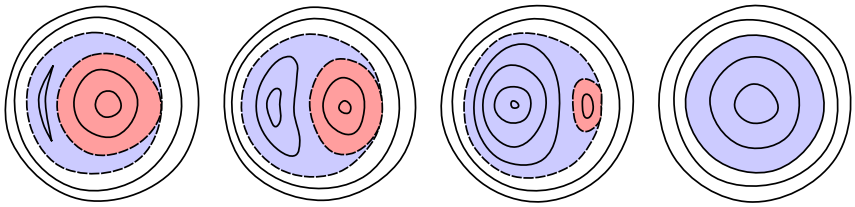

Figure 3.2: Sketch of the evolution of the plasma core according to Kadomtsev's full sawtooth reconnection model. The $(m = 1, n = 1)$ magnetic island (blue) grows until it has replaced the original core (red). Based on [56].

experimentally observed location of the inversion radius. The evolution of the core magnetic field structure according to Kadomtsev's model is sketched in Figure 3.2.

The time the reconnection process needs to complete is given by

$$\tau_{\mathrm{K}} \approx (\tau_\eta \tau_A^*)^{1/2} \tag{3.2}$$

where $\tau_\eta = \mu_0 r_1^2/\eta$ is the resistive time, $\tau_A^* = r_1(\mu_0\rho)^{1/2}/(B_\theta(r_1)(1-q_0))$ is the Alfvén time with respect to the helical magnetic field and r_1 is the radius of the $q = 1$ surface.

During the ramp phase after the crash, Ohmic heating and, if present, additional central heating sources increase the core temperature causing the core resistivity to decrease[1]. This leads to a central peaking of the electric current density and thus to a decrease of the central safety factor profile. The configuration becomes internal kink unstable again and the cycle starts over.

3.1.3 Beyond the Kadomtsev model

Many numerical simulations, the first ones having been presented in [57–59], have confirmed that the dynamics described by Kadomtsev's model do occur within resistive MHD. However, some features of the experimental observations cannot be explained by this model, indicating that effects that lie outside the scope of the resistive MHD model have to be taken into account in order to describe the sawtooth instability correctly.

One of these features is the time scale of the temperature crash. The reconnection time according to the Kadomtsev model given by Equation (3.2) is more than an order of magnitude too slow compared to measured values

[1] A commonly used expression for the plasma resistivity is given by Spitzer's model predicting $\eta \sim T^{-3/2}$ [8].

for large high-temperature tokamaks and increases with decreasing resistivity which also does not correspond to the observations [17].

Several mechanisms have been proposed that could speed up the reconnection process. One of them is the plasmoid instability. This instability already occurs within the resistive MHD model, but only at resistivities close to experimental values which are difficult to achieve in simulations. At these low resistivities the thin current sheet at the reconnection site becomes tearing unstable and secondary islands are formed [60]. It has been shown in resistive MHD simulations that the occurrence of plasmoids can speed up sawtooth reconnection and lead to a reconnection time that is only weakly dependent on resistivity [61–64].

Beyond resistive MHD, some two-fluid effects have been shown to accelerate the reconnection process. As mentioned in Section 2.2, two-fluid effects lead to a modification of Ohm's law as, for example, described in [16]. At high temperatures where resistive diffusion becomes less dominant, these modifications can play an important role. Examples for such effects that can enable fast reconnection are electron inertia [65], the Hall term [66, 67], parallel electron viscosity [68] and the parallel electron pressure gradient [64].

Another feature of the experimental observations that is not reflected by the Kadomtsev model is the long quiescent ramp-up phase. According to the resistive cylindrical MHD model, the internal kink is destabilized as soon as there is a $q = 1$ surface inside the plasma. Hence the model does not explain the long ramp-up phase that appears to be MHD stable until q_0 reaches values significantly lower than unity. The stabilization of the internal kink mode by toroidicity at low β cannot explain this phenomenon for all different experimentally observed cases [17]. Thus, the internal kink seems to be stabilized by a mechanism that resistive MHD misses. Various candidates for this mechanism like diamagnetic effects [69], finite ion Larmor radius effects [70] and stabilization from energetic ions [71] have been proposed.

A different experimental observation that has not yet been theoretically explained is the process of *incomplete sawtooth reconnection*. As discussed in Section 3.1.1, in many cases it is found that the safety factor on axis stays below unity during the entire sawtooth cycle. In contrast to complete Kadomtsev reconnection, where the original plasma core is entirely expelled and $q_0 = 1$ is restored after each crash, these observations seem to suggest that the magnetic reconnection process stops before completing.

A model for incomplete sawtooth reconnection would need to provide a stabilizing mechanism that prevents the reconnection process from completing as well as an explanation for the efficient heat transport given that the magnetic topology only changes partly. Although some approaches have been brought forward, e.g. [17, 47, 67, 72, 73], incomplete reconnection has not yet been reproduced in realistic 3D nonlinear simulations.

3.2 Hybrid scenario

As mentioned before, in the standard mode of operation, the plasma current in a tokamak is generated by a transformer. This implies an upper limit for the length of a discharge which represents a disadvantage of the tokamak configuration with regard to its suitability for future nuclear fusion reactors. For this reason, so called *Advanced scenarios* are being developed which allow for extended discharge lengths or even continuous, also called *steady-state*, operation. The exploration of Advanced tokamak scenarios is one of the objectives of the ITER program. This discussion of Advanced tokamak scenarios is based on [10] where more detailed information, especially with regard to the preparation for the operation of ITER, can be found.

In order to increase the possible length of a discharge, plasma current has to be driven non-inductively. This can be done by creating the conditions that maximize the *bootstrap current*, a diffusion-driven toroidal current caused by temperature and density gradients [8], or by external current sources like the injection of neutral beams or radio-frequency waves.

The standard inductive operational scenarios, called *L-mode* and *H-mode*, the latter providing improved confinement due to a transport barrier at the edge of the plasma, are characterized by positive magnetic shear and $q_0 \leq 1$ (and exhibit sawteeth). In contrast, the fully non-inductive, steady-state Advanced scenario has reversed magnetic shear, i.e. an off-axis maximum of the current density, and $q_0 > 1.5$, leading to an internal transport barrier that improves confinement and thereby increases the contribution of the bootstrap current. However, as a result of the large pressure gradient and the negative magnetic shear, steady-state Advanced scenarios are prone to MHD instabilities which prevents them from reaching the performance of standard H-mode scenarios.

The *Hybrid scenario* is a different type of Advanced scenario that is not

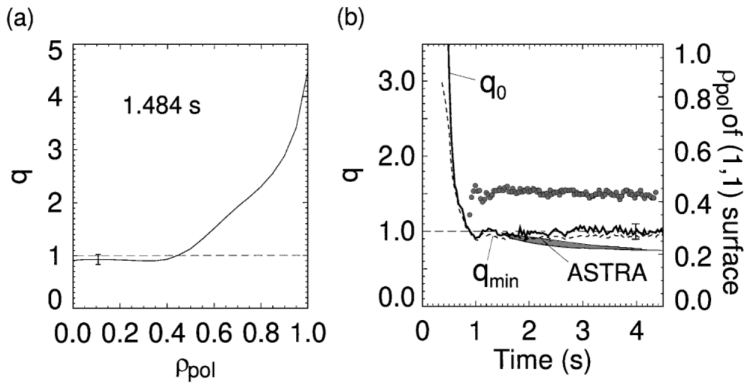

Figure 3.3: (a) Safety factor profile and (b) time evolution of the central and the minimum value of the safety factor as well as the radial position of the $q = 1$ surface in an ASDEX Upgrade Hybrid discharge. The grey line shows the predicted time evolution of q_0 according to a transport simulation by means of the ASTRA code [76]. Reprinted figure with permission from [O. Gruber et. al, Physical Review Letters, 83, 1787–1790 (1999)]. Copyright 1999 by the American Physical Society.

suitable for steady-state operation without external current drive, but allows for discharges of extended duration at high performance. It is characterized by low, sometimes slightly reversed, or vanishing magnetic shear in the central plasma and $q_0 \approx 1$. Originally called *Improved H-mode*, the scenario became known as Hybrid as it represents a mode of operation in between the inductive standard H-mode and the fully non-inductive steady-state scenario. Hybrid discharges provide good core confinement because of the low magnetic shear [74]. In addition, as $q_0 \approx 1$, they do not exhibit sawteeth which prevents the seeding of neoclassical tearing modes.

Often, current diffusion calculations based on the applied heat and current sources for Hybrid discharges predict q_0 to drop below unity [11–13] which would lead to sawtoothing. An example is shown in Figure 3.3. The discrepancy between prediction and measurements in these cases is due to an unexplained mechanism which broadens the central current density profile so that q_0 is clamped to a value close to unity. As this corresponds to a redistribution of poloidal magnetic flux, this phenomenon is sometimes called *magnetic flux pumping* [13]. This mechanism also facilitates the drive of plasma current by external sources as the current can be driven in the plasma center where the current drive efficiency is highest, and is then redistributed via flux pumping [75].

Hybrid discharges have been generated in most large tokamaks such as ASDEX Upgrade [11,12,77], DIII-D [13,75,78–80], JET [81] and JT60-U [82].

In order to set up a Hybrid discharge, the plasma center is additionally heated during the current ramp-up phase. During this phase at the beginning of a discharge, the current density diffuses from the edge towards the center of the plasma. Additional heating reduces the current diffusion leading to a broader central current density profile at the beginning of the discharge.

The necessary conditions for the occurrence of flux pumping seem to differ between tokamaks. In ASDEX Upgrade discharges, the clamping of q_0 close to unity was first thought to be linked to the presence of the fishbone instability [11, 83], a small-amplitude periodic relaxation oscillation driven by energetic particles [84, 85]. However in later experiments flux pumping was found to occur also when fishbones were absent [12]. In DIII-D discharges, flux pumping seems to be only possible at high enough β and in the presence of either a $(m = 3, n = 2)$ tearing mode or an externally excited $(m = 1, n = 1)$ perturbation of the plasma core [86].

Various attempts have been made to explain how Hybrid discharges are sustained [13, 87–89], but a self-consistent generally accepted explanation is still lacking. However, understanding the mechanism behind flux pumping is crucial in order to be able to extrapolate the properties and accessibility of the Hybrid scenario to larger future devices like ITER.

3.3 Tokamak plasmas with helical core in numerical simulations

In this thesis, 3D nonlinear resistive MHD simulations are presented in which magnetic flux pumping occurs due to a saturated quasi-interchange instability manifesting itself as a stationary helical $(m = 1, n = 1)$ perturbation of the core plasma and, in particular, a $(m = 1, n = 1)$ convection cell.

The phenomenon of a central helical $(m = 1, n = 1)$ convection cell that develops instead of sawtooth cycling has been seen before in nonlinear resistive MHD simulations. It was first reported in [90] in 2D reduced MHD simulations with helical symmetry. In [72], a similar model, but without temperature evolution, is used and it is pointed out that a dynamo effect might be the cause for the obtained stationary helical state. A stationary state featuring a helical $(m = 1, n = 1)$ core and convection cell has also been found in 3D MHD simulations which include two-fluid effects, but use a time-independent

resistivity [91]. In this reference, it is proposed that a saturated reconnecting mode is responsible for the absence of sawteeth.

Whereas in the mentioned works, the primary focus was set on analyzing the dynamics of sawtooth cycles, recently, the helical stationary states themselves have become a focal point of interest and are compared to some experimentally observed phenomena in tokamak discharges, e.g. [92, 93].

A different framework for examining tokamak plasma states with a helically perturbed core are calculations of 3D equilibria. Ideal MHD 3D equilibrium solver, originally developed for the analysis of stellarator[2] equilibria, are now also used to examine tokamak equilibria that feature 3D perturbations like helical cores, e.g. [94, 95]. It is found that at weak reversed magnetic shear and values of the safety factor in the neighborhood of unity in the plasma center, besides the axisymmetric equilibrium there is a second state of equilibrium at similar potential energy which has a 3D helical core [94]. In [96], this finding is applied to the Hybrid scenario in ITER. The results of ideal MHD 3D equilibrium calculations are compared to linear and nonlinear ideal MHD stability calculations in [97, 98].

In this thesis, emphasis is put on understanding how the helical states are sustained in 3D nonlinear resistive MHD simulations, under which conditions they occur, and how these helical states can give rise to magnetic flux pumping. This is done with the aim of contributing to a better understanding of magnetic flux pumping in Hybrid discharges.

[2] A stellarator is another toroidal confinement configuration that, in contrast to a tokamak, is not axisymmetric.

Chapter 4

Magnetic flux pumping in 3D magnetohydrodynamic simulations

As discussed in Section 3.2, there is a mechanism of magnetic flux pumping in Hybrid discharges which keeps the safety factor profile in the center of the plasma flat and close to unity despite current or heat sources that work towards centrally peaking the current density profile. As a result, these discharges do not exhibit sawtoothing. In Reference [1], 3D nonlinear MHD simulations in tokamak geometry have been presented in which sawtoothing is also prevented by a flux pumping mechanism. The following discussion is based on this finding. A detailed analysis of how the flux pumping mechanism in the simulations works is given in Section 4.2. Subsequently, the results of a large set of different 3D nonlinear MHD simulations run to their asymptotic states are characterized. Depending on certain parameters, flux pumping either prevents sawtoothing as in the cases presented in Section 4.3, or they exhibit sawtooth-like reconnection events as examined in Section 4.4. Based on this set of simulations, it is discussed in Section 4.5 under which conditions the flux pumping mechanism can be sufficiently strong to prevent sawtoothing in the simulations. In Section 4.6, some aspects of the flux pumping mechanism are examined in more detail based on a linear stability analysis of an equilibrium with low central magnetic shear.

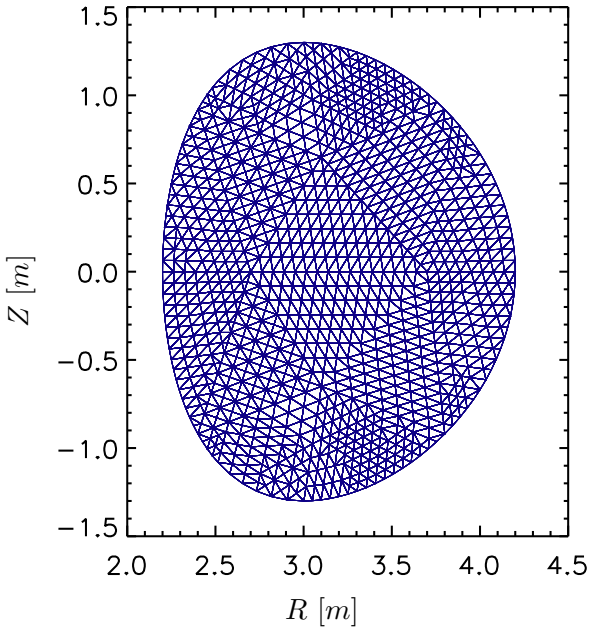

Figure 4.1: Mesh in the *R*-*Z* plane.

4.1 Simulation set-up

The presented calculations have been performed using the high-order finite-element MHD code M3D-C^1 described in Chapter 2.9. The resistive single-fluid MHD model in toroidal geometry is used. The number of toroidal elements is eight, and the mesh in each *R*-*Z* plane, shown in Figure 4.1, has about 1000 nodes. The boundary of the computational domain is up-down-symmetric and coincides with a contour of constant poloidal magnetic flux. The time resolution is $40\,\tau_A$[1]. For each of the 3D nonlinear simulations a corresponding 2D axisymmetric nonlinear calculation is done in order to isolate 3D phenomena.

As the focus is put on the asymptotic states of the simulations, they cover time spans of a few $10^5\,\tau_A$. Each has been run on 64 processors typically using about $7..15 \cdot 10^3$ core hours. A large set of calculations is analyzed, obtained by varying three parameters: the poloidal β, the perpendicular heat diffusion coefficient together with the strength of the heat source, and the peakedness of the heat source profile. All other parameters are held fixed. To keep the

[1]The Alfvén time is defined as $\tau_A = a\sqrt{\mu_0 n m_i}/B$ where a, n and B are a typical length scale, and typical values for the particle density and the magnetic field, respectively. It represents a characteristic time for MHD processes and is used as the time normalization in M3D-C^1 (see Table 4.1).

Spitzer resistivity similar between simulations with different values of β, it is rescaled accordingly. The chosen resistivity is a factor of $10^2..10^3$ higher than realistic resistivities in modern large tokamaks due to limited computational resources. Similarly, the viscosity is a little more than one order of magnitude higher than its realistic value[2].

As in the following analysis, different physical processes are compared whose time scales are set by either resistive diffusion or heat diffusion, it is important to ensure a realistic ratio of resistive and heat diffusion time scales. Therefore, the perpendicular heat diffusion coefficients are scaled up similarly as the resistivity. In order to examine the influence of varying the resistivity while keeping its ratio to the perpendicular heat diffusion coefficient fixed, one simulation (case 'n') has been rerun with both η as well as $\chi_\perp$ and the strength of the heat source scaled up by a factor of three (case 'nX3').

The heat diffusion anisotropy has values of $\chi_\parallel/\chi_\perp \approx 10^4..3 \cdot 10^6$ in the plasma center which is significantly smaller than realistic values. However, as $q \approx 1$ in the plasma core, a value of the heat diffusion anisotropy which would allow for the parallel heat diffusion to have an influence on perpendicular heat transport within the core[3] would not be achievable in the simulations due to computational limitations. The values of the toroidal magnetic field on axis and the total plasma current are realistic, although a little smaller than typical values in large, modern tokamaks. Details on the used parameters are given in Table 4.1.

The applied loop voltage as well as the strength of the particle source are feedback controlled to maintain the total current and the total number of particles, respectively. The safety factor profile and the temperature as well as the density profile reached in the asymptotic limit of the 2D simulations for two example cases are shown in Figure 4.2. For all cases, the asymptotic 2D safety factor profile has $q_0 < 1$, which means that in the corresponding 3D simulations the safety factor profile is driven towards an internal kink unstable state.

[2]This assumes a value of about $1\mathrm{m}^2/\mathrm{s}$ for a realistic kinematic viscosity.

[3]For typical magnetic field configurations in the central plasma region of sawtooth-free states in the simulations, $\chi_\parallel/\chi_\perp$ would need to have a value of about at least 10^9 for parallel diffusion to lead to a heat transport across the magnetic field over a distance of about 0.1 m that would be comparable to the transport due to $\chi_\perp$.

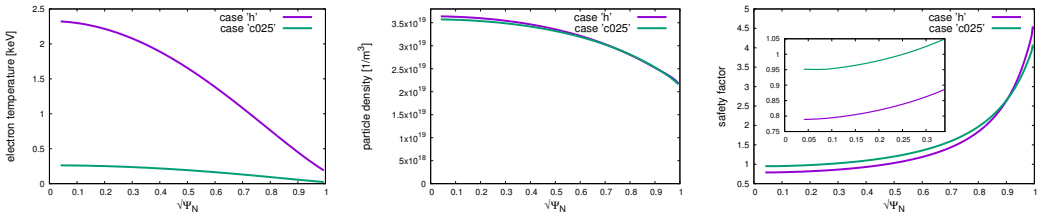

Figure 4.2: Electron temperature, particle density and safety factor profiles of the asymptotic state in the 2D simulations for two example cases. These profiles would be reached in the asymptotic state of the corresponding 3D simulations if they were not altered by MHD instabilities.

perpendicular thermal diffusivity	$\chi_\perp \approx 1.36 \cdot 10^{-9} \cdot \kappa_0 \cdot \frac{n[\mathrm{m}^{-3}]}{T[\mathrm{K}]^{1/2}}\ \mathrm{m}^2/\mathrm{s}$
parallel thermal diffusivity	$\chi_\parallel \approx 3.45 \cdot 10^7\ \mathrm{m}^2/\mathrm{s}$
energy source	$S = 1.25 \cdot 10^{-17} \cdot \frac{a_S}{d_S^2} \cdot \exp\left(\frac{(R-R_{\mathrm{axis}})^2+Z^2}{-2.03 \cdot d_S^2}\right)\ \mathrm{Pa/s}$
resistivity	$\eta = 4 \cdot 10^{-6} \cdot \left(\frac{T}{T_{\mathrm{axis}}}\right)^{-\frac{3}{2}}\ \Omega\,\mathrm{m}$
viscosity	$\nu = 2.3 \cdot 10^{-6}\,\mathrm{kg/(ms)}$
toroidal magnetic field on axis	$B_{\mathrm{axis}} = 1\,\mathrm{T}$
total current	$I_{\mathrm{tot}} = 6.4 \cdot 10^5\,\mathrm{A}$
total number of particles	$n_{\mathrm{tot}} = 2.3 \cdot 10^{21}$
shape of last closed flux surface	$R[\mathrm{m}] = 3.2 + \cos(\theta + 0.2 \sin\theta)$
	$Z[\mathrm{m}] = 1.3 \sin\theta$
time normalization	$\tau_A = 2.90 \cdot 10^{-7}\mathrm{s}$

Table 4.1: Parameters used for the presented set of simulations. The values for κ_0, a_S and d_S for the different cases are listed in Table 4.2.

4.2 The flux pumping mechanism

Similar to Hybrid discharges, the sawtooth-free state found in these 3D nonlinear MHD simulations is characterized by a central region with very low magnetic shear where the safety factor has a value close to unity. In the simulations, this state features a stationary $(m = 1, n = 1)$ perturbation in the core, in particular a $(m = 1, n = 1)$ helical flow as shown in Figure 4.3. The flow is generated by a saturated quasi-interchange instability allowed for by the low magnetic shear [22, 23, 99]. This is indicated by the flow pattern which is characteristic for such an instability (compare Figure 2.8) and by the dependency on β which will be discussed in Section 4.5. Also the linear stability analysis presented in Section 4.6 shows that such a low magnetic shear equilibrium is unstable with respect to a quasi-interchange instability.

The comparison of the safety factor profiles in such a 3D nonlinear simulation and in a corresponding 2D axisymmetric calculation in Figure 4.4 shows that a 3D effect is responsible for the observed flattening of the central current density. The 2D simulation can be seen as an analog to the transport simulations in [11–13], discussed in Section 3.2, which falsely predict $q_0 < 1$ for the described Hybrid discharges. This section is based on the ideas presented in [1] while adding a more detailed analysis on selected aspects.

In the following, it is illustrated which 3D effects can alter the background $(n = 0)$ toroidal current density by analyzing the induction equation

$$\partial_t \mathbf{B} = -\nabla \times \mathbf{E} \tag{4.1}$$

where $\mathbf{E}$ is the electric field. After replacing the magnetic field $\mathbf{B}$ by $\mathbf{B} = \nabla \times \mathbf{A}$, where $\mathbf{A}$ is the magnetic vector potential, integration of Equation (4.1) leads to

$$\partial_t \mathbf{A} = -\mathbf{E} - \nabla \Phi \,. \tag{4.2}$$

Here, Φ is a single valued potential. Using cylindrical coordinates (R, ϕ, Z), the projection of Equation (4.2) onto the toroidal direction yields

$$\partial_t \Psi = -R\eta J_\phi + R\hat{\phi} \cdot (\mathbf{v} \times \mathbf{B}) - R\hat{\phi} \cdot \nabla \Phi \,. \tag{4.3}$$

Here Ohm's law $\mathbf{E} = \eta \mathbf{J} - \mathbf{v} \times \mathbf{B}$ has been used to eliminate the electric

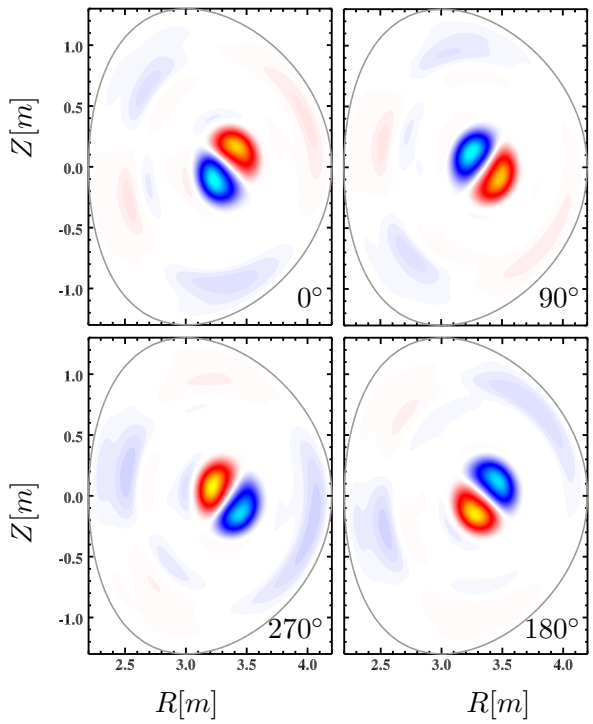

Figure 4.3: Difference between the poloidal velocity stream function in a stationary 3D simulation and in the corresponding 2D axisymmetric calculation for different toroidal angles. Negative values are indicated in blue and positive values in red. It can be seen that the velocity perturbation has the form of a $(m = 1, n = 1)$ convection cell in the plasma center. (Case 'n', $t = 160000\,\tau_A$).

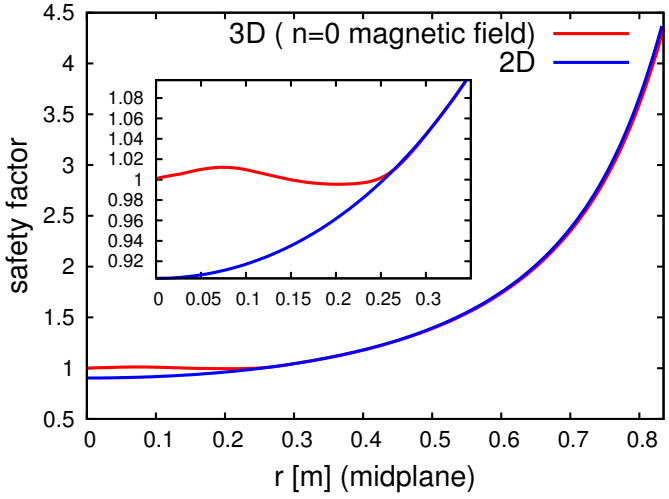

Figure 4.4: Comparison of the safety factor profile in the asymptotic state of a 3D and the corresponding 2D axisymmetric simulation. For the 3D case, the safety factor profile has been calculated using the toroidally averaged magnetic field. (Case 'n').

field, and the toroidal component of the magnetic vector potential has been replaced by $\Psi\nabla\phi$, where Ψ denotes the negative of the poloidal magnetic flux ψ_p per radian. All quantities are split into an axisymmetric part[4] and a non-axisymmetric part, and only the dominant $n = 1$ component of the latter is taken into account. The toroidal average of Equation (4.3) then gives

$$\partial_t \Psi_0 = -R\eta_0 J_{\phi,0} - R\left[\eta_1 J_{\phi,1}\right]_{n=0} + R\left[\hat{\phi}\cdot(\mathbf{v}_1 \times \mathbf{B}_1)\right]_{n=0} . \tag{4.4}$$

Note that $\nabla\Phi_0 = 0$ and it is assumed that $\mathbf{v}_0 = 0$. The $n = 0$ quantities can be expressed in terms of the corresponding quantities in the 2D axisymmetric system plus a deviation due to the influence of the 3D perturbation on the $n = 0$ background: $\Psi_0 = \Psi_{2D} + \Delta\Psi$, $\eta_0 = \eta_{2D} + \Delta\eta$ and $J_{\phi,0} = J_{\phi,2D} + \Delta J_\phi$. The toroidal component of the induction equation for the 2D system reads

$$\partial_t \Psi_{2D} = -R\eta_{2D} J_{\phi,2D} . \tag{4.5}$$

For a stationary state, $\partial_t \Psi_{2D}$ is given by $\frac{V_L}{2\pi}$, where V_L is a constant, corresponding to the externally applied tokamak loop voltage.

As the difference between the 2D and the 3D $n = 0$ state is not too large, Equation (4.4) can be linearized around the corresponding 2D solution in order to extract 3D effects. This yields

$$0 = -R\Delta\eta J_{\phi,2D} - R\eta_{2D}\Delta J_\phi + R\left[\hat{\phi}\cdot(\mathbf{v}_1 \times \mathbf{B}_1)\right]_{n=0} - R\left[\eta_1 J_{\phi,1}\right]_{n=0} \tag{4.6}$$

where the term $\partial_t \Delta\Psi$ has been dropped because it vanishes for stationary cases as well as for cases with a quasi-stationary periodic time evolution when it is time averaged over one period.

The last term on the right of Equation (4.6) is negligible in the simulations as will be shown later. Out of the three remaining terms, the second term on the right describes the observed difference in the toroidal current density between a 3D and a 2D calculation and the two other terms represent mechanisms which can potentially be responsible for this difference. One possibility to obtain a flattening of the central current density profile is via a flattening of the central resistivity profile as described by the term that is proportional

[4]Note, that in this and the following chapter the index 0 always refers to the $n = 0$ component of the indexed quantity, with the exception of q_0 which refers to the value of the safety factor on axis to be consistent with the common notation.

to $\Delta\eta$. In some of the simulations presented this is the leading effect as resistivity flattening is caused by a convective flattening of the temperature profile through the helical ($m = 1, n = 1$) flow described above. This flow is also crucial for the second current flattening effect described by the third term on the right of Equation (4.6). In this case the velocity perturbation combines with the perturbation of the magnetic field yielding a $n = 0$ reduction of the background current density in the plasma center via a dynamo mechanism. This effect corresponds to an effective negative loop voltage in the center of the tokamak opposing the externally applied loop voltage.

The strength of the different terms in Equation (4.6) in the plasma center is shown in Figure 4.5 for stationary states in two different simulations. In the case shown on the left the resistivity flattening effect is dominantly responsible for the diminished central toroidal current density, whereas in the other case the current flattening is predominantly caused by the dynamo loop voltage effect. The difference between these two cases is the value of the perpendicular heat diffusion coefficient $\chi_\perp$ and correspondingly the strength of the heat source. They are higher in the second case which leads to a stiffer temperature profile that cannot easily be altered by convection. Therefore, the resistivity flattening effect does not play a significant role in the second case. The temperature gradient remains large, driving the instability that results in the dynamo driven loop voltage. In modern large tokamaks, and in particular in Hybrid H-mode discharges which are characterized by strong heating and large turbulent heat flux, the ratio of the resistive time scale to the heat diffusion time scale $\mu_0\chi_\perp/\eta$ is in a regime where the dynamo effect is dominant in our simulations.

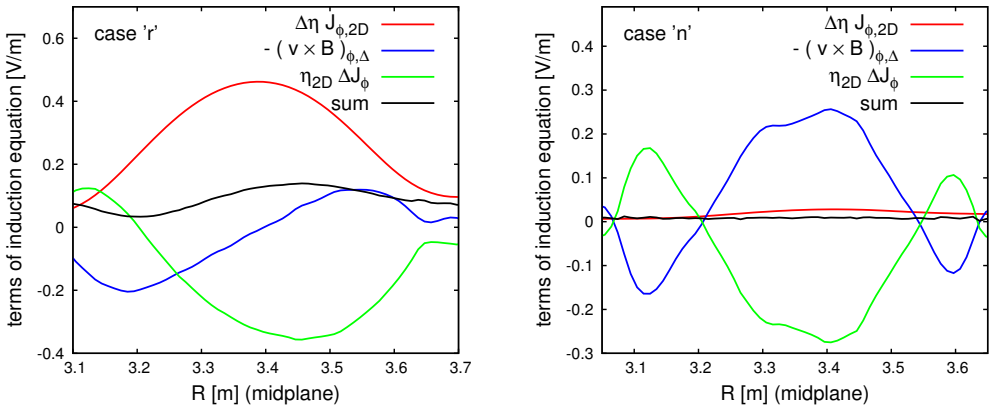

Figure 4.5: Terms of the linearized induction equation in the plasma center in two simulations with different values of $\mu_0\chi_\perp/\eta$. A flattening of the central $n = 0$ current density profile can be caused by a flattening of the resistivity profile described by $\Delta\eta J_{\phi,2D}$ and by a dynamo loop voltage described by $-(\mathbf{v} \times \mathbf{B})_{\phi,\Delta} = -[(\mathbf{v} \times \mathbf{B})_{\phi,3D,n=0} - (\mathbf{v} \times \mathbf{B})_{\phi,2D}]$. Note, that the sum of the three terms is negligible showing that these two effects fully account for the occurring change of the current density. The case on the right has a higher value of $\chi_\perp$ and a proportionately stronger heat source yielding a stiffer temperature profile which decreases the effectiveness of convective resistivity flattening.

4.3 Sawtooth-free cases

In the following, two typical examples of simulations resulting in sawtooth-free states are discussed. The first example reaches an asymptotic state that is entirely time-independent. The characteristic $(m = 1, n = 1)$ convection cell in the plasma center and the flat central safety factor profile close to unity for such a case have been shown in Figures 4.3 and 4.4. The Poincaré plots in Figure 4.6 show the magnetic field line structure for such a stationary state. Note, that these Poincaré plots have to be interpreted with care. The safety factor in the central region is flat and very close to unity, thus the informative value of the obtained structures is limited, as very small deviations in the safety factor profile have a great impact on the appearance of the Poincaré plot. For instance, in this case, the magnetic field line structure seems to be dominated by higher harmonics than $n = 1$ although the $n = 1$ harmonic contains the largest magnetic energy as can be seen in Figure 4.7.

The second example is a slight variation of this stationary case. It tends to occur at high values of $\mu_0\chi_\perp/\eta$ as will be seen in Figure 4.15. In this case, the asymptotic state features the same characteristics, but superimposed with an oscillation. The $n = 1$ magnetic and kinetic energies for such an oscillatory

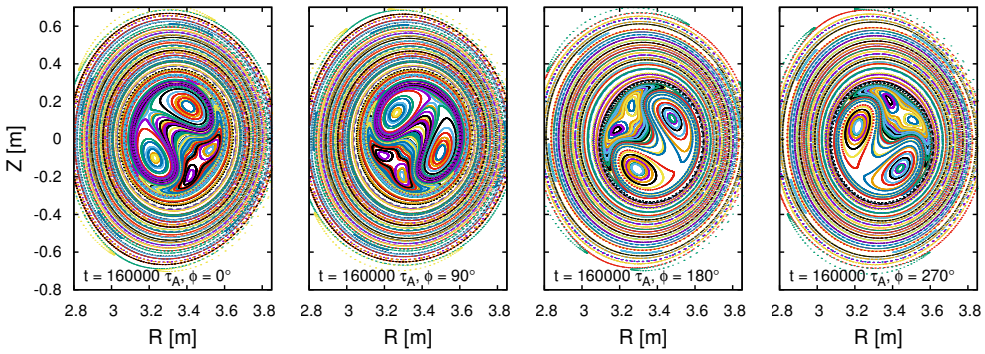

Figure 4.6: Case 'n': Poincaré plots of the central region for different toroidal angles.

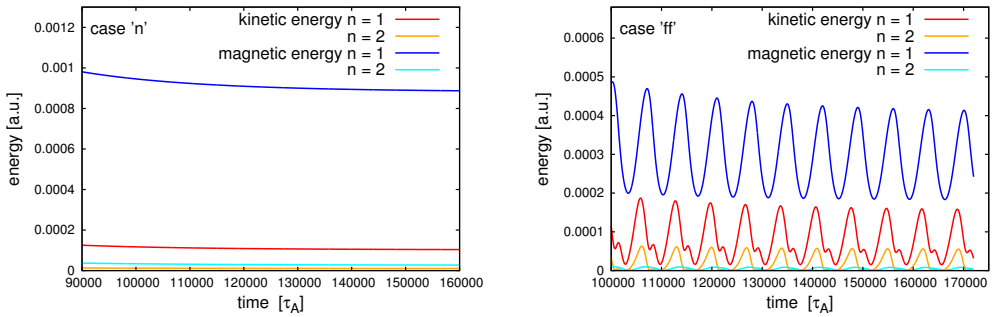

Figure 4.7: Kinetic and magnetic energies of the $n = 1$ and $n = 2$ harmonics for a stationary case (left) and for a quasi-stationary oscillatory case (right). In both cases sawtoothing is prevented.

case are shown in Figure 4.7. Figure 4.8 shows the strength of the dynamo loop voltage effect as well as the time evolution of the minimum value of the safety factor ($q_{\min}$) and q_0. It can be seen that despite the oscillation, the central safety factor profile is still very close to unity at all times so that sawtoothing is prevented. An oscillation is also seen in the magnetic field line structure also shown in Figure 4.8, but the structure is qualitatively similar to the stationary case.

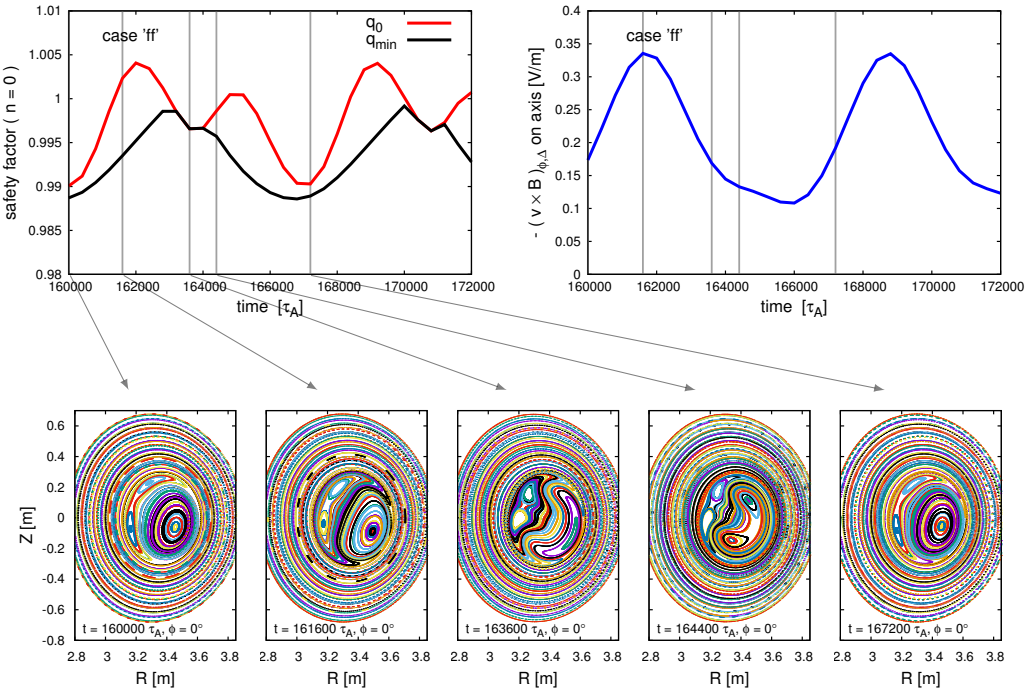

Figure 4.8: *Top*: Time evolution of the value of q on axis and the minimum value of q and of the strength of the dynamo loop voltage term on axis for a quasi-stationary case. Despite the oscillation, the dynamo loop voltage effect is strong enough to keep the safety factor profile in the central plasma region flat with values close to unity at all times. *Bottom*: Poincaré plots of the central region for different points in time.

4.4 Sawtoothing cases

In the sawtoothing cases, the safety factor on axis decreases to values significantly below unity such that $q_0 \approx 1$ is restored by magnetic reconnection in periodically repeating crashes. The time traces of the magnetic and kinetic energies for such a case are shown in Figure 4.9, and the time evolution of q_0 and $q_{\min}$ are shown in Figure 4.10. The evolution of the magnetic topology is in agreement with Kadomtsev's full reconnection model as can be seen from the Poincaré plots for different points in time during one cycle in Figure 4.11. As the resistivity used is significantly above its realistic value and two-fluid effects are not included into the calculations, several characteristics of realistic sawtooth crashes like the fast crash times as found in [64, 69, 100] are not expected to be reproduced in these simulations.

The time trace of the strength of the dynamo loop voltage on axis for this case, shown in Figure 4.10, reveals why this case behaves so differently than

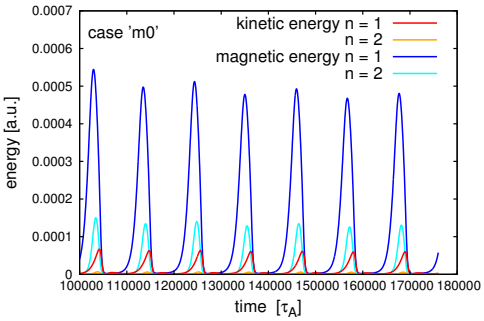

Figure 4.9: Kinetic and magnetic energies of the $n = 1$ and $n = 2$ harmonics for a case exhibiting a sawtooth-like behavior. After each crash axisymmetry is restored.

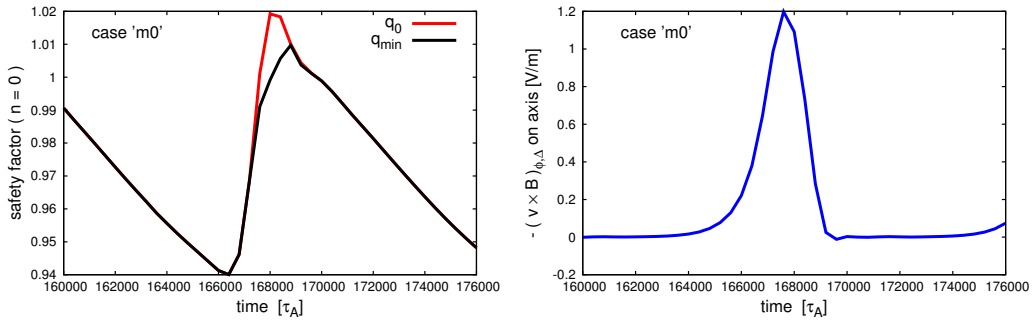

Figure 4.10: Time evolution of q_0 and the minimum value of q (left) and the strength of the dynamo loop voltage on axis (right) during about one cycle for a case exhibiting a sawtooth-like behavior.

the sawtooth-free cases. In between the crashes, the dynamo loop voltage vanishes, which means that it cannot compensate for the tendency of the current density to centrally peak. This leads to the decrease of q_0 and the onset of the reconnection process. Only during the sawtooth crashes, there is a spike in the central dynamo loop voltage due to the strong $(m = 1, n = 1)$ flow which is caused by the reconnection process reorganizing the central plasma and magnetic field line structure.

In another type of sawtoothing cases that is found, the sawtooth cycle starts similarly as described above with a decrease of q_0 destabilizing an internal kink, but instead of completing, the reconnection process stops and reverses. The corresponding evolution of the magnetic topology is shown in Figure 4.12. In these cases axisymmetry is not recovered after the crashes which manifests itself in an offset in the $n = 1$ magnetic energy as shown in Figure 4.13. Also the dynamo loop voltage on axis, shown in Figure 4.14, does not vanish completely.

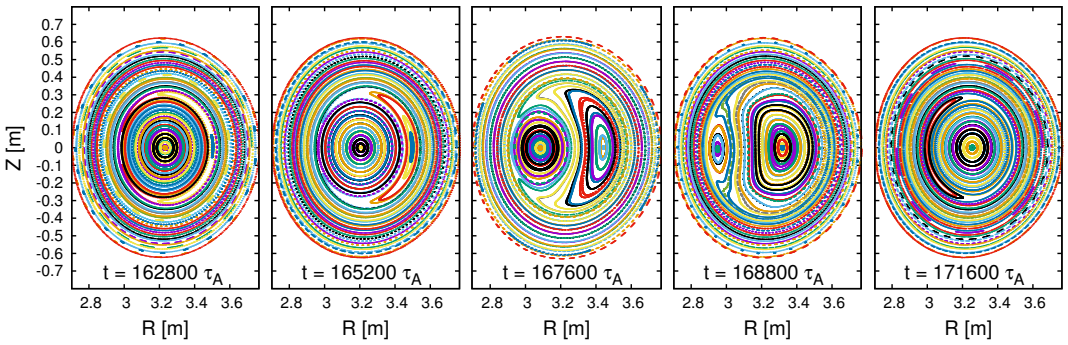

Figure 4.11: Poincaré plots showing the magnetic field line structure in the central plasma region at different points in time during a sawtooth cycle. As described in Kadomtsev's model, the $(m = 1, n = 1)$ magnetic island grows until it has entirely replaced the original plasma core. (Case 'm0').

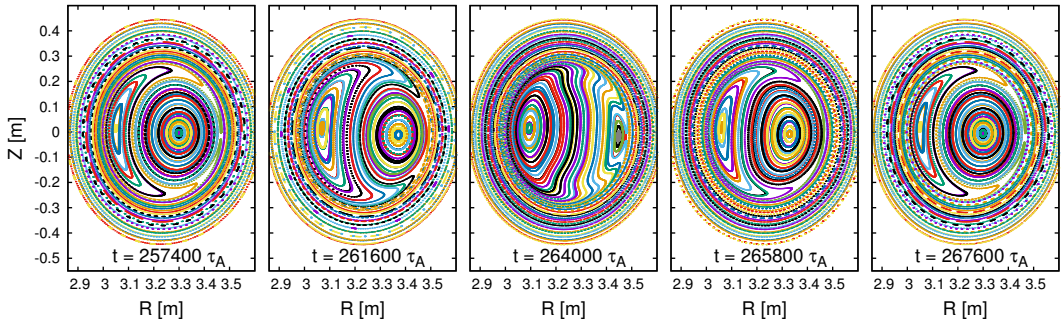

Figure 4.12: Poincaré plots showing the magnetic field line structure in the central plasma region at different points in time during an incomplete sawtooth cycle. Before the $(m = 1, n = 1)$ magnetic island can replace the original plasma core, the reconnection process stops and reverses. Note, that this series of plots cover one entire cycle showing that an axisymmetric state is not reached at any time. (Case 'm3').

Note, that these cases qualitatively differ from the oscillatory cases discussed in Section 4.3 in that q_0 falls significantly below unity. As seen on the Poincaré plots, the reconnection process lets the original core shrink and regrow, whereas in the oscillatory cases, the structures in the central region seem mainly to be deformed, but not to change in size.

As will be seen from the second plot in Figure 4.15, these incomplete sawtooth reconnection cases only occur if the tendency of the current density to centrally peak is relatively weak. This means that in these cases the linear drive for the internal kink instability is low. It is possible that in a more complete model than the one used for the presented calculations, a similar behavior occurs also for a more peaked current density profile if the internal

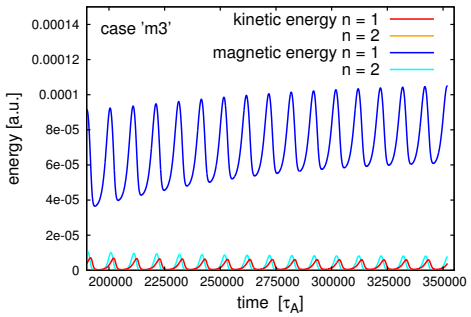

Figure 4.13: Kinetic and magnetic energies of the $n = 1$ and $n = 2$ harmonics for a case exhibiting incomplete sawtooth reconnection. Since the reconnection process does not complete, there is a finite offset in the $n = 1$ magnetic energy.

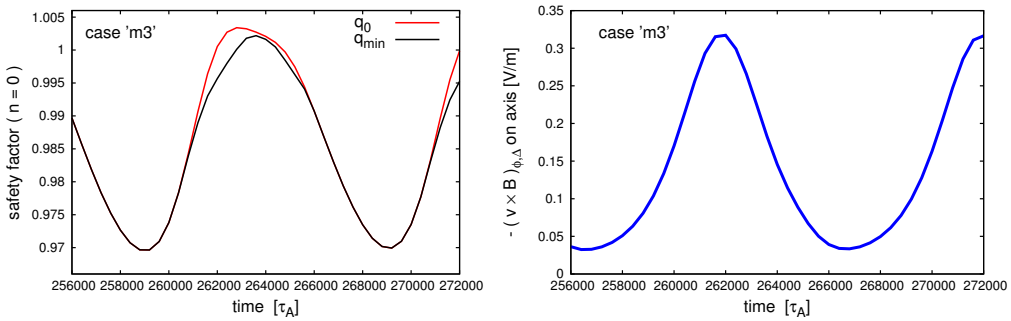

Figure 4.14: Time evolution of q_0 and $q_{\min}$ (left) and the strength of the dynamo loop voltage on axis (right) during about two cycles for a case exhibiting incomplete sawtooth reconnection.

kink is stabilized by a more realistic physics model including, for example, diamagnetic drift, finite Larmor radius or energetic particle effects [101]. It is to be investigated if this might then provide a possible explanation for the experimental observations indicating incomplete sawtooth reconnection.

4.5 Conditions for the prevention of sawteeth

As a next step, it is examined under which conditions the flux pumping mechanisms are strong enough to be able to prevent sawtoothing in the simulations. For this purpose, the entire set of 3D nonlinear MHD simulations is analyzed. The three parameters parameters that have been varied to generate the set of simulations are described in more detail in the following.

(1) The poloidal beta is defined as

$$\beta_{p1} = \frac{2\mu_0}{B_\theta^2} \int_0^{r_1} \left(\frac{r}{r_1}\right)^2 \left(-\frac{dp}{dr}\right) dr \tag{4.7}$$

where r is the midplane minor radius and r_1 is the radius where the velocity perturbation vanishes. The value of β_{p1} determines the drive of the instability that enables flux pumping by generating the necessary helical flow.

(2) The ratio of the resistive time scale to the heat diffusion time scale $\mu_0\chi_\perp/\eta$ has been varied by varying $\chi_\perp$ at the same rate as the strength of the applied heat source while keeping η fixed. As mentioned before, this quantity controls the stiffness of the temperature profile and thus the effectiveness of the resistivity flattening effect.

(3) The third parameter varied is the peakedness of the heat source. In a 2D simulation this parameter determines the value of q_0 which is a measure for how strong the current flattening mechanism in a 3D simulation needs to be in order to keep $q_0 = 1$. We define Δ_{2D} as the corresponding rate of magnetic flux pumping:

$$\begin{aligned} \Delta_{2D} &= -\frac{2\eta B_{\phi,\text{axis}}}{\mu_0 R_{\text{axis}}} \frac{(1 - q_{0,2D})}{q_{0,2D}} \\ &\approx \eta J_{\phi,\text{axis}}(q_0 = 1) - \eta J_{\phi,\text{axis}}(q_0 = q_{0,2D}) \,. \end{aligned} \tag{4.8}$$

In Figures 4.15-4.17, each data point corresponds to one of the 3D nonlinear MHD simulations run to their asymptotic states. As mentioned before, the first plot in Figure 4.15 shows that oscillatory cases tend to occur at high values of $\mu_0\chi_\perp/\eta$. Note that the case 'nX3' being a stationary case despite the fact that it has a three times larger value of $\chi_\perp$ than case 'n', confirms that it is not $\chi_\perp$, but really its ratio to η which is crucial.

According to both plots in Figure 4.15, sawtooth-free states only occur at sufficiently high β_{p1}. Below that threshold in β_{p1}, the pressure-driven instability at low magnetic shear is not strong enough to provide the helical flow necessary for the flux pumping mechanisms to work. The existence of a threshold in β is consistent both with the simulation results presented in [91] and with Hybrid discharges being characterized by high values of β.

In order to verify the idea that only in the sawtooth-free cases, the provided amount of flux pumping suffices to keep the central safety factor close

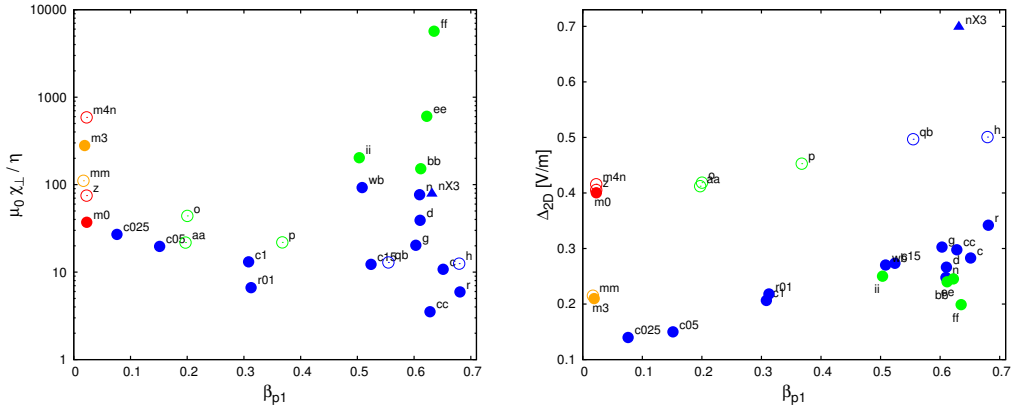

Figure 4.15: Overview of the covered parameter space. Each data point corresponds to a 3D nonlinear simulation run to its asymptotic state. Stationary and quasi-stationary sawtooth-free cases are marked in blue and green, respectively. Cases exhibiting complete and incomplete sawtooth reconnection are marked in red and orange, respectively. Open symbols correspond to cases with a more peaked heat source profile. The case marked by a triangle has a three times larger resistivity. Note, that for cases with $\beta_{p1} < 0.03$ and $\mu_0 \chi_\perp / \eta < 1.5 \cdot 10^2$, Ohmic heating plays a role in determining the heating profile.

case	r	c	g	bb	ee	cc	c025	c05	c1
κ_0	1.75e-6	3.5e-6	7.e-6	5.6e-5	1.1e-4	1.2e-6	3.5e-6	3.5e-6	3.5e-6
a_S	5.e22	1.0e23	2.0e23	1.6e24	3.2e24	2.5e22	2.2e22	3.7e22	5.8e22
d_S	0.5	0.5	0.5	0.5	0.5	0.5	0.5	0.5	0.5

case	r01	m3	m0	n	d	c15	ff	wb	ii
κ_0	1.75e-6	1.76e-5	2.2e-6	2.8e-5	1.4e-5	3.5e-6	2.18e-3	2.8e-5	5.6e-5
a_S	2.3e22	8.e22	0.0	8.e23	4.e23	8.7e22	6.40e25	7.4e23	1.48e24
d_S	0.5	0.5	–	0.5	0.5	0.5	0.5	0.5	0.5

case	p	o	aa	qb	h	m4n	z	mm	nX3
κ_0	5.e-6	7.e-6	3.5e-6	3.5e-6	3.5e-6	3.52e-5	4.4e-6	5.5e-6	8.4e-5
a_S	8.e22	8.e22	3.5e22	7.1e22	8.0e22	1.4e23	9.5e21	1.15e22	2.4e24
d_S	0.4	0.4	0.4	0.4	0.4	0.4	0.4	0.4	0.5

Table 4.2: Parameters κ_0, a_S and d_S as defined in Table 4.1 for the different cases. Note that case 'nX3' has a three times larger resistivity.

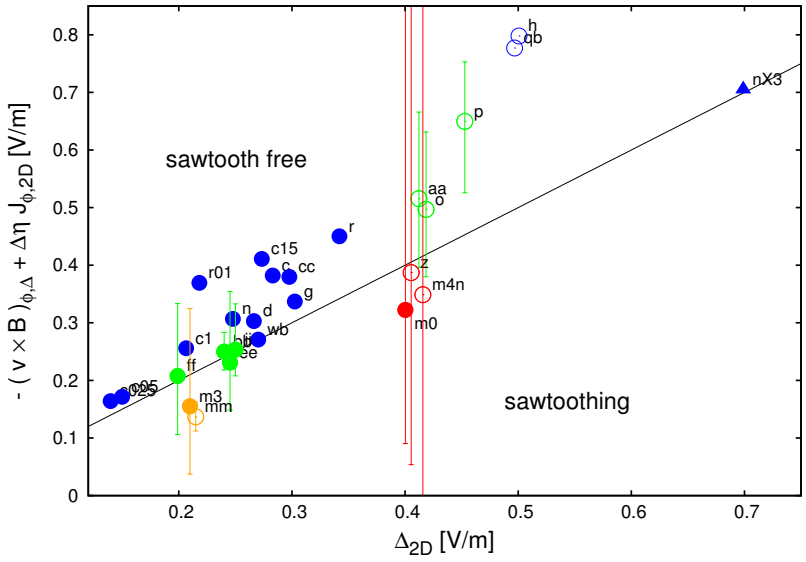

Figure 4.16: Combined strength of magnetic flux pumping effects on axis versus the amount of flux pumping which is necessary to keep $q_0 = 1$ for the different 3D nonlinear simulations. The black line indicates where the two quantities are equal. The sawtooth-free cases (blue and green) lie at or above this threshold, whereas the sawtoothing cases (red and orange) are found below. As the strength of the flux pumping effects varies with time for the oscillating and the sawtoothing cases, error bars indicate the range of their oscillation and the data points are set to their time-average over one period.

to unity at all times, this amount of flux pumping provided by the two current flattening mechanisms described in Section 4.2 is compared to the rate of magnetic flux change needed to keep $q_0 = 1$. The latter quantity is approximately given by Δ_{2D} defined by Equation (4.8). As in the cases with a periodic time evolution, the strength of the flux pumping mechanisms also varies with time (e.g., see Figures 4.8, 4.10 and 4.14), its time average over one period is used for the comparison. Figure 4.16 confirms that sawteeth are avoided only if the combined strength of the two current flattening mechanisms equals or exceeds the value of Δ_{2D}. Note that even for case 'nX3' which has a significantly larger value of Δ_{2D} because of the larger resistivity, the flux pumping mechanisms are sufficiently strong to compensate it.

As expected, the sawtoothing cases do not meet this condition. The flux pumping provided by the magnetic reconnection process during each crash is able to restore $q_0 \approx 1$ periodically, but $q_0 \approx 1$ is not maintained at all times.

In Figure 4.17 the two current flattening mechanisms are separated, show-

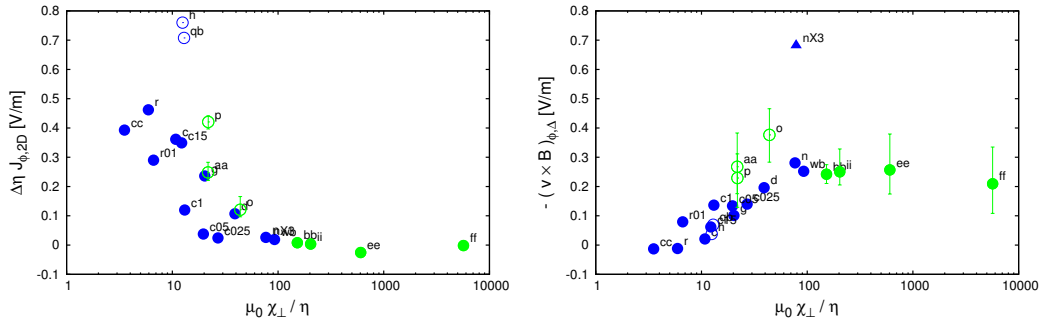

Figure 4.17: Strength of the resistivity flattening effect (left) and the dynamo loop voltage (right) on axis for different sawtooth-free cases. The value of $\chi_\perp$ which is varied together with the strength of the heat source controls the stiffness of the temperature profile.

ing that for increasing $\mu_0\chi_\perp/\eta$ the strength of the resistivity flattening effect decreases whereas the dynamo loop voltage effect strengthens. As discussed before, the former trend is due to the decreased effectiveness of the convective flattening of the temperature profile for high values of $\chi_\perp$ and strong heat sources. The decrease of the strength of the dynamo voltage effect for low $\chi_\perp$ is due to the fact that the strong resistivity flattening effect already provides enough current flattening to keep $q_0 \approx 1$. An additional dynamo loop voltage would further increase the central value of the safety factor above unity. This would stabilize the low-shear pressure-driven instability which needs $q \approx 1$ and thus weaken the helical flow responsible for the dynamo voltage. In this way the strength of the dynamo loop voltage effect is self-regulated to always provide a flat safety factor profile close to unity in the plasma center.

4.6 Linear stability analysis of an equilibrium with low central magnetic shear and $q_0 \approx 1$

In the previous sections, it has been discussed how, in 3D nonlinear MHD simulations with low central magnetic shear and $q_0 \approx 1$, a saturated quasi-interchange instability can generate $(m = 1, n = 1)$ velocity and magnetic field perturbations which combine to give an effective negative loop voltage via a dynamo effect. In this section, the linear stability of an equilibrium with low central magnetic shear and $q_0 \approx 1$ is analyzed. It is confirmed that the resulting most unstable mode can be characterized as a quasi-interchange

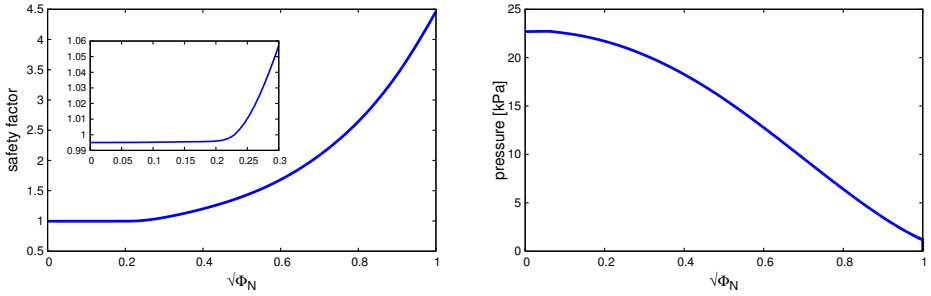

Figure 4.18: Safety factor profile and pressure profile of the analyzed equilibrium. Φ_N denotes the normalized toroidal magnetic flux.

instability and it is examined if by combining the linear velocity and magnetic field eigenfunctions a corresponding dynamo loop voltage can be obtained.

The calculations have been performed using the linear eigenvalue code CASTOR3D [102–104]. The analyzed equilibrium is defined by the pressure profile and the safety factor profile shown in Figure 4.18. The geometry and parameters are based on the 3D nonlinear case 'bb' discussed in the previous sections. However, diffusion coefficients are not included except for the resistivity. Note that as an exact equivalent to the safety factor profile in a 2D equilibrium cannot be calculated from a 3D state, a simple safety factor profile which is flat and close to unity in the plasma center has been chosen.

As discussed in Section 2.8, the quasi-interchange instability is an ideal, pressure-driven $(m = 1, n = 1)$ instability, located in the plasma center. Its velocity eigenfunction has the characteristic form of a $(m = 1, n = 1)$ convection cell featuring a significant flow on axis. As shown in Figure 4.19, the instability that is found in this case is indeed ideal as its growth rate is approximately independent of the resistivity for a wide range of resistivities.

The characteristic flow pattern is shown in Figure 4.20. For comparison, the flow pattern of an internal kink instability is shown in Figure 4.21. It has a different shape and in particular a significantly lower velocity on axis than near the $q = 1$ surface. The shapes of the velocity eigenfunctions for the two instabilities agree with Section 6.10 of [8] as discussed in Section 2.8.

The linear velocity and magnetic field perturbations of the quasi-interchange instability can be used to calculate a $(m = 0, n = 0)$ dynamo loop voltage $(\mathbf{v} \times \mathbf{B})_\phi$ in the plasma center as shown in Figure 4.22. In order to be able to estimate if this dynamo loop voltage has a strength that is comparable to the real dynamo loop voltage found in the 3D nonlinear simulations, $\mathbf{v}$ and $\mathbf{B}$ are

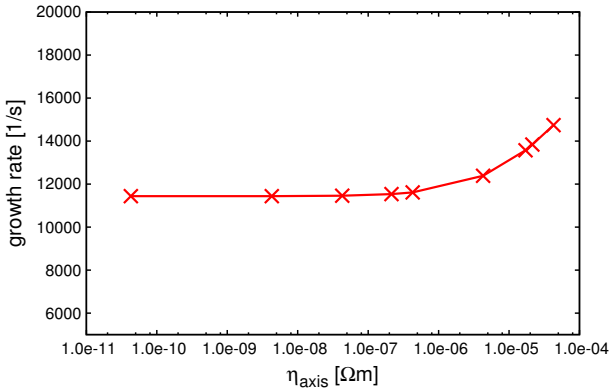

Figure 4.19: Growth rates of the most unstable mode for different resistivities.

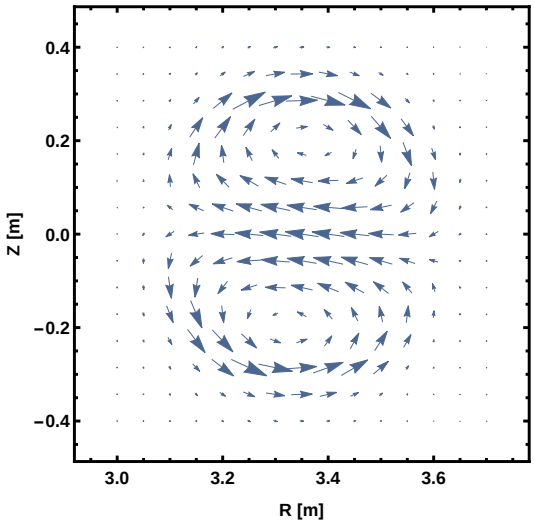

Figure 4.20: Velocity field in one R-Z plane in the plasma center.

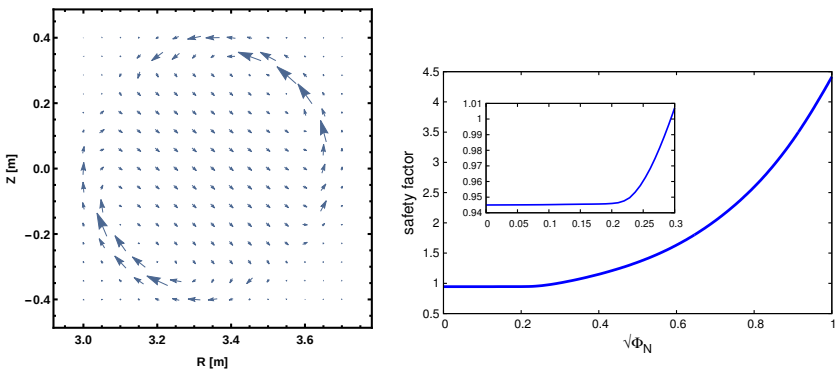

Figure 4.21: Velocity field in one R-Z plane in the plasma center for an internal kink instability obtained by using the safety factor profile shown on the right. (The pressure profile and all other parameters are the same as in the case discussed above.)

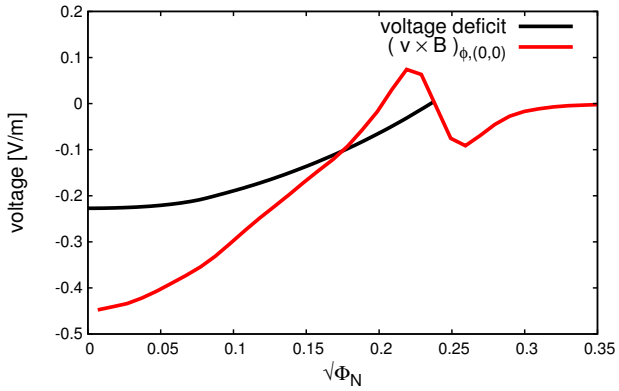

Figure 4.22: Red curve: $(m = 0, n = 0)$ component of the dynamo loop voltage term calculated using the linear eigenfunctions which have been scaled by a factor so that the maximum of $\sqrt{v_R^2 + v_Z^2}$ matches the same quantity in the 3D nonlinear simulation 'bb' ($t = 145600\,\tau_A$). Black curve: Voltage that is necessary to raise the safety factor profile in the center to unity in the 2D nonlinear simulation corresponding to case 'bb' ($t = 145600\,\tau_A$).

scaled such that the maximum of $\sqrt{v_R^2 + v_Z^2}$ is the same as in the 3D nonlinear case 'bb' which is used for the comparison. The scaled dynamo loop voltage is compared to the amount of loop voltage that needs to be provided in the 3D nonlinear simulation in order to maintain $q \approx 1$ within the central region of the plasma. This voltage deficit is calculated from the safety factor profile in the corresponding 2D nonlinear simulation as

$$\frac{2B_{\phi,2D}\eta_{2D}}{\mu_0 R}\left(1 - \frac{1}{q_{2D}}\right) . \tag{4.9}$$

The comparison shows that the strength of the dynamo loop voltage which has been calculated from the linear eigenfunctions is comparable with the dynamo loop voltage in the 3D nonlinear simulation. Note, that perfect agreement is not expected as the linear stability calculation is based on a 2D axisymmetric equilibrium whereas the sawtooth-free state in the 3D nonlinear calculation has a 3D helical core.

In contrast, the linear velocity and magnetic field eigenfunctions of the internal kink instability also give a dynamo loop voltage in the plasma center, but if it is scaled accordingly, it is significantly weaker than for the quasi-interchange instability as can be seen in Figure 4.23. This is due to the relatively lower velocity in the plasma center.

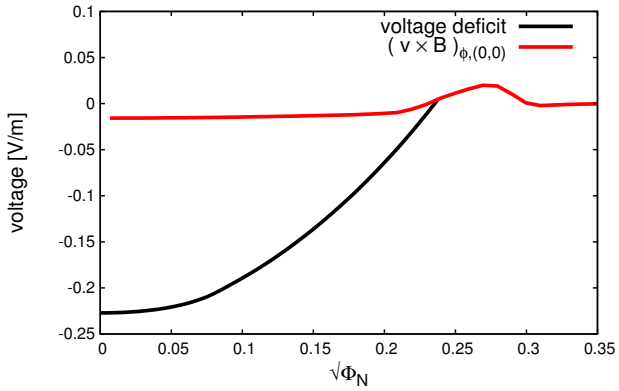

Figure 4.23: Red curve: $(m = 0, n = 0)$ component of the dynamo loop voltage term calculated using the linear eigenfunctions of an internal kink instability (see Fig. 4.21). $\mathbf{v}$ and $\mathbf{B}$ have been scaled by a factor so that the maximum of $\sqrt{v_R^2 + v_Z^2}$ matches the same quantity in the 3D nonlinear simulation 'bb' ($t = 145600\,\tau_A$). Black curve: Voltage that is necessary to raise the safety factor profile in the center to unity in the 2D nonlinear simulation corresponding to case 'bb' ($t = 145600\,\tau_A$).

If this dynamo loop voltage from the internal kink instability could have a significant influence in a 3D nonlinear simulation depends on the actual strength of the central $(m = 1, n = 1)$ flow. In the 3D nonlinear simulations presented in the previous sections, the typical velocities during sawteeth are not significantly larger than during the sawtooth-free states. However, when discussing the effect of the dynamo loop voltage during sawteeth, it also has to be kept in mind that the shape of the perturbations changes significantly during the nonlinear evolution of the internal kink instability.

Interestingly, it is found that for a slight variation of the low shear safety factor profile that has two $q = 1$ surfaces, the velocity and magnetic field perturbations do not combine to a dynamo loop voltage that would match the nonlinear results as can be seen in Figure 4.24. And this is despite the fact that the resulting instability is still a quasi-interchange instability featuring the characteristic $(m = 1, n = 1)$ convection cell. If this has any relevance for the 3D nonlinear simulations needs to be further investigated.

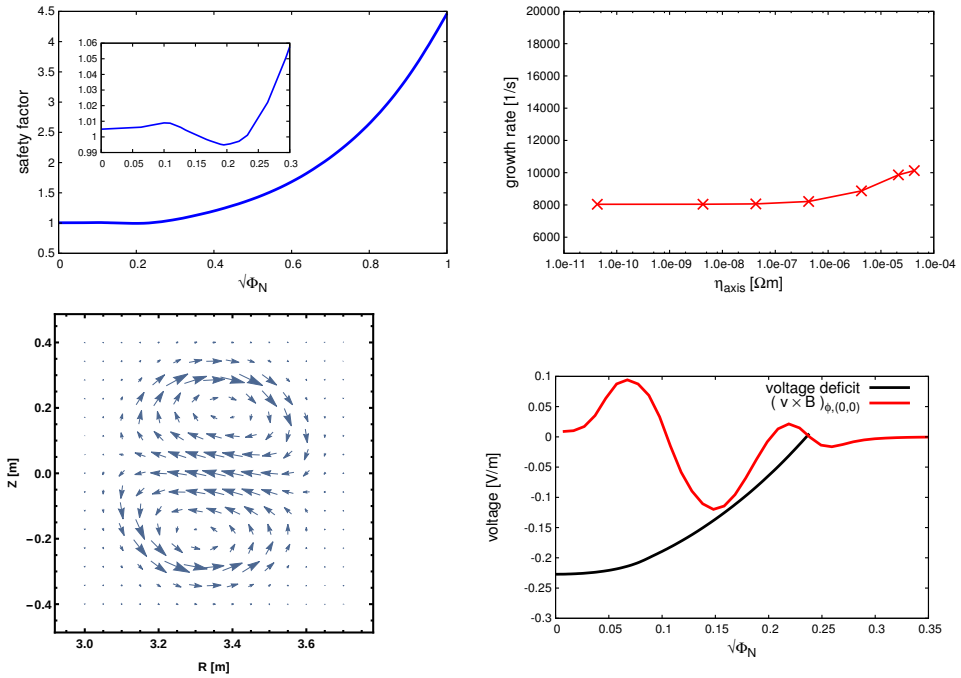

Figure 4.24: Top left: Safety factor profile which is slightly reversed in the center. Top right: Growth rates of the most unstable mode for an equilibrium with the shown safety factor profile. (Calculations have been done for deuterium, so the growth rates have to be multiplied by $\sqrt{2}$ in order to compare to the other calculations which use hydrogen.) Bottom left: Velocity field in one R-Z plane in the plasma center for this case. Bottom right: Comparison of the dynamo loop voltage calculated from the linear eigenfunctions scaled in the same way as described above and the voltage deficit in the nonlinear simulation (case 'bb', $t = 145600\,\tau_A$).

Chapter 5

Towards more realistic simulations of Hybrid discharges

In the previous chapter, the basic physics of magnetic flux pumping has been studied by means of 3D nonlinear MHD simulations using a relatively simple set-up. A simplified plasma shape has been used and parameters have been chosen to allow for relatively low spatial and temporal resolution.

Moreover, the conditions for a sawtooth-free state, namely a safety factor profile that is flat and close to unity in the center, have been set up by starting the simulation from a state that was strongly unstable with respect to the internal kink, with q_0 significantly below unity, leading to a sawtooth crash generating the desired safety factor profile. As the focus was put solely on the asymptotic time evolution of the simulations, this represented a fast and efficient way of starting the simulations. The described choices made it possible to analyze the basic physics mechanisms in relatively simple examples and helped to reduce the computational effort to a level that allowed for detailed parameters scans.

In the following, some aspects of the path towards more realistic 3D nonlinear MHD simulations of Hybrid discharges are explored. A set of simulations is presented that uses an ASDEX Upgrade like geometry and more realistic plasma parameters requiring higher temporal and spatial resolution. Instead of starting the simulation from a highly unstable state that the plasma might not have been able to achieve in the first place, the simulations are set up in a way that tries to mimic some aspects of the start-up of a realistic Hybrid tokamak discharge. During the current ramp-up at the beginning of a toka-

mak discharge the current density diffuses inwards, leading to a central safety factor profile that reaches the targeted value from above. In order to generate Hybrid discharges, the current diffusion during this phase is reduced by additional central heating, yielding a broader current density profile, as described in Section 3.2. Thus, the goal is to start the simulations from a safety factor profile that has low magnetic shear in the center and $q_0 > 1$, and let it decrease so that the plasma state self-consistently enters the region of instability for $(m = 1, n = 1)$ modes. Details about the simulation set-up and parameters are described in Section 5.1.

It is found that both types of behavior described in Chapter 4, the sawtooth-free states with helically perturbed core and the states that exhibit a sawtooth-like behavior, do occur within the presented set of more realistic simulations. These two types of simulation results are described and analyzed in Sections 5.2.1 and 5.2.2, respectively. Although detailed parameter scans could not be performed due to limited computational resources, it is shown that the way in which the two types of results are distributed over the parameter space is consistent with the previous finding. Furthermore, an additional variation of the sawtoothing cases is found where the sawtooth-like events are separated by quiescent phases that show the characteristics of sawtooth-free states.

5.1 Simulation set-up

The presented simulations have been performed using the resistive single-fluid model of the high-order finite-element code M3D-C^1 described in Chapter 2.9. For each of the 3D nonlinear calculations, a corresponding 2D axisymmetric calculation with the same set-up and parameters has been done in order to facilitate the identification of 3D effects. All simulations have been performed in toroidal geometry, the number of toroidal planes is eight and each R-Z plane has approximately 3700 nodes. The R-Z mesh has been refined in the center of the computational domain as shown in Figure 5.1. The temporal resolution is one Alfvén time. The boundary of the computational domain is up-down-symmetric and coincides with a contour of constant poloidal magnetic flux.

The plasma resistivity corresponds to Spitzer resistivity which has been scaled by a constant factor. It is about two to three orders of magnitude larger than realistic values in the plasma core of large, modern tokamaks due to limited computational resources. Parallel and perpendicular heat diffusion

perpendicular thermal diffusivity	$\chi_\perp \approx 2.7 \cdot 10^3\,\mathrm{m}^2/\mathrm{s}$
parallel thermal diffusivity	$\chi_\parallel \approx 2.7 \cdot 10^8\,\mathrm{m}^2/\mathrm{s}$
resistivity	$\eta \approx 5 \cdot 10^{-6} \cdot \left(\frac{T}{T_{\mathrm{axis}}}\right)^{-\frac{3}{2}}\,\Omega\,\mathrm{m}$
toroidal magnetic field on axis	$B_{\mathrm{axis}} \approx 1.8\,\mathrm{T}$
shape of last closed flux surface	$R[\mathrm{m}] = 1.659 + 0.46\cos(\theta + 0.2\sin\theta)$
	$Z[\mathrm{m}] = -0.025 + 0.8\sin\theta$
time normalization	$\tau_A = 4.6 \cdot 10^{-7}\,\mathrm{s}$

Table 5.1: Parameters used for the simulations.

coefficients are constant[1] both in time and space. Their ratio of 10^5 is significantly smaller than realistic values for the heat diffusion anisotropy so that in the simulations, parallel heat diffusion does not play a role in perpendicular heat transport within the plasma center as discussed in the previous chapter.

However, the ratio of the resistive and heat diffusion time scales $\mu_0\chi_\perp/\eta$ is in a range where in the simulations discussed in the previous chapter, the temperature profile is sufficiently stiff so that the dynamo loop voltage effect dominates over the resistivity flattening effect, which is the range where also realistic Hybrid discharges are in.

The values of the toroidal magnetic field on axis and the total plasma current correspond to typical values for ASDEX Upgrade discharges. Two different values for the viscosity have been used, the lower one being in the range of realistic values. Details on the parameters used in all of the simulations are listed in Table 5.1. Parameters that have been varied between the cases are listed in Table 5.2.

The simulations span a time of about $1..3 \cdot 10^4\tau_A$. Each has been run on 128 processors typically using about $3..6 \cdot 10^4$ core hours. The necessary amount of computational resources has been significantly reduced by using the 2D axisymmetric version of the code for the first part of each simulation. This is possible because the plasma stays approximately axisymmetric until the

[1] More precisely, $\kappa_\parallel = \chi_\parallel n_{\mathrm{axis}}$ and $\kappa_\perp = \chi_\perp n_{\mathrm{axis}}$ are constants.

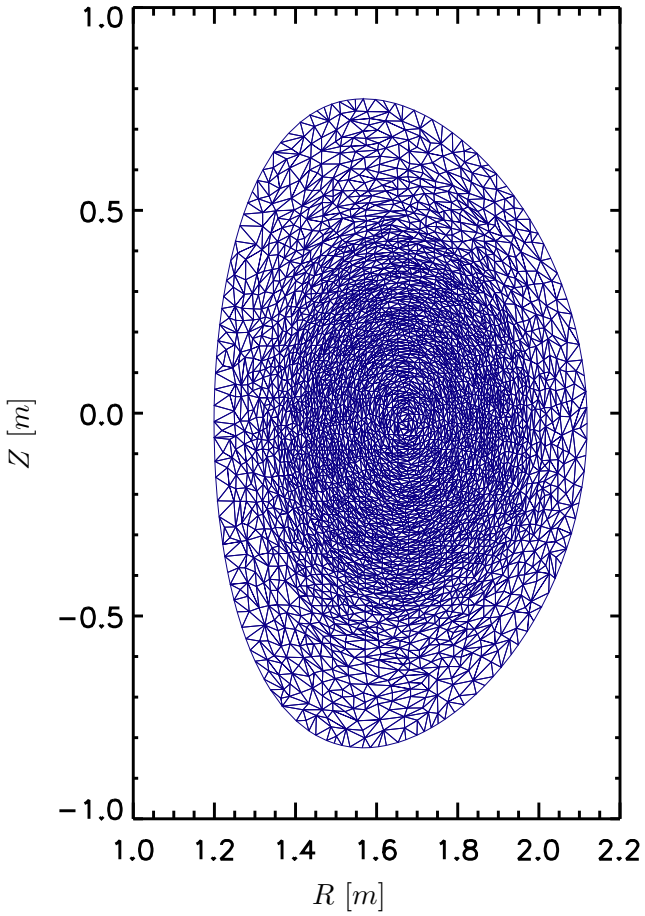

Figure 5.1: The mesh in the R-Z plane used for the simulations is refined in the center.

minimum value of the safety factor reaches unity. The simulations are restarted in 3D shortly before this is the case, the plasma then stays axisymmetric until the stability boundary is crossed. This will be seen from the time evolution of the kinetic and magnetic energies in the different toroidal harmonics which is shown in Figures 5.11 and 5.14 for the entire time range of the 3D part of the simulations.

All calculations start with a safety factor profile which is above unity and flat in the plasma center. The initial temperature profile is consistent with the initial q-profile via Spitzer resistivity. The safety factor is then ramped down by applying a heat source that leads to a temperature profile which is consistent with a q-profile with $q_0 < 1$. This is done in two different ways:

(1) A heat source profile is used that corresponds to the heat source profile which is consistent with the initial temperature profile scaled by a constant

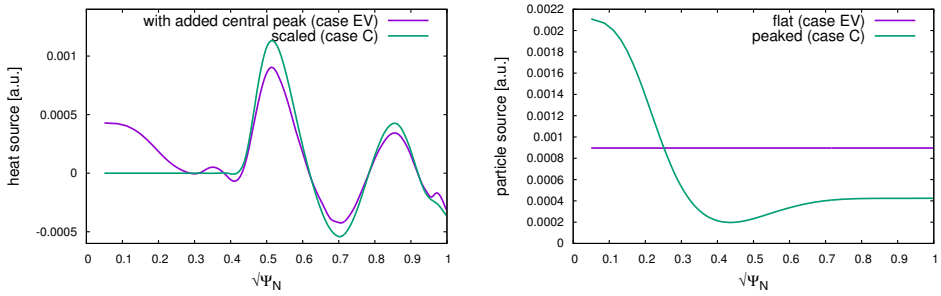

Figure 5.2: Heat and particle source profiles used for the different simulation set-ups. The heat source profile used in cases with a feedback controlled total current (violet) maintains the initial safety factor profile outside $\sqrt{\Psi_N} \approx 0.3$, but tends to peak the safety factor profile downwards in the plasma center. The heat source profile used in cases without feedback control of the total current via the loop voltage (turquoise) maintains the shape of the safety factor profile while shifting it downwards. For cases with a flat temperature profile, a peaked particle source profile (turquoise) can be used in order to generate a larger central pressure gradient.

(see Figure 5.2). The feedback control of the loop voltage which keeps the total current constant is switched off. As a consequence, the q-profile approximately maintains its shape and shifts downwards as shown in Figure 5.3.

(2) The used heat source profile corresponds to the sum of the heat source profile which is consistent with the initial temperature profile and a peaked one in the plasma center (see Figure 5.2). The total current is kept constant by the feedback control as in most experiments. The resulting evolution of the q-profile is shown in Figure 5.3. While q_0 decreases, the safety factor profile at the edge does not change.

Figure 5.2 also shows two examples of particle sources that are used. Different shapes and strengths of the particle source are used to vary the central pressure gradient and the plasma beta, respectively. Examples of pressure, particle density and temperature profiles resulting from combinations of the different heat and particle sources are shown in Figure 5.4.

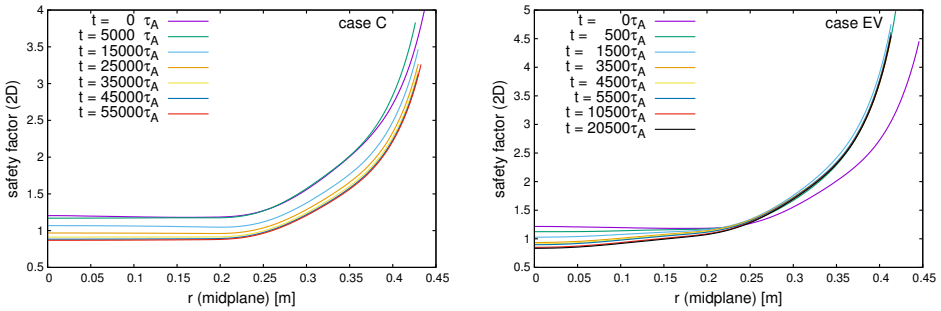

Figure 5.3: Time evolution of the safety factor profile in a 2D axisymmetric simulation for two different set-ups: In the case on the left side, the entire safety factor profile shifts downwards without changing its shape, whereas in the case on the right side, the value of the safety factor at the edge is kept approximately constant and the magnetic shear in the center changes. Note, that this is the time evolution the safety factor profile in the corresponding 3D simulation would follow if no instabilities were changing the safety factor.

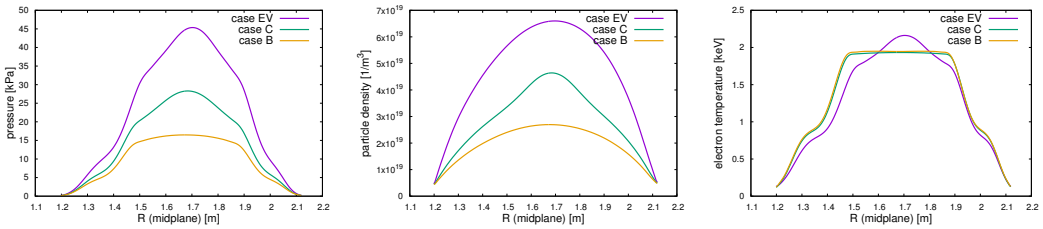

Figure 5.4: Pressure, particle density and electron temperature profiles of the asymptotic state in 2D simulations for different cases. These represent the profiles which would be consistent with the heat and particle sources in the corresponding 3D simulations, i.e. would result without the effect of instabilities.

Case	I_{tot} [A]	feedback control	heat source	particle source	viscosity [kg/ms]	β_{p1}
A	$6.6 \cdot 10^5$	on	peaked	flat	$3.6 \cdot 10^{-8}$	0.09
B	$\approx 9 \cdot 10^5$	off	scaled	flat	$3.6 \cdot 10^{-8}$	0.10
C	$\approx 9 \cdot 10^5$	off	scaled	peaked	$3.6 \cdot 10^{-8}$	0.13
D	$\approx 9 \cdot 10^5$	off	scaled	peaked	$3.6 \cdot 10^{-8}$	0.29
CV	$\approx 9 \cdot 10^5$	off	scaled	peaked	$3.6 \cdot 10^{-6}$	0.13
AV	$6.6 \cdot 10^5$	on	peaked	flat	$3.6 \cdot 10^{-6}$	0.10
HV	$6.6 \cdot 10^5$	on	peaked	flat	$3.6 \cdot 10^{-6}$	0.18
EV	$6.6 \cdot 10^5$	on	peaked	flat	$3.6 \cdot 10^{-6}$	0.25

Table 5.2: Overview of the simulation set-ups. The definition of β_{p1} is given in Equation (4.7).

5.2 Simulation results

Within the set of simulations discussed in Chapter 4, two different types of long-term behavior have been identified. Either the plasma exhibits a sawtooth-like behavior where $q_0 = 1$ is periodically restored, or the plasma goes into a sawtooth-free state with a helically perturbed core where the central safety factor profile is prevented from decreasing significantly below unity by magnetic flux pumping. Both types have as well been found in the set of more realistic simulations that is presented here.

An overview of the simulation results in β_{p1}-Δ_{2D} space is given in Figure 5.5. The quantities β_{p1} and Δ_{2D} are defined by Equations (4.7) and (4.8), respectively. As discussed in the previous chapter, Δ_{2D} describes how peaked the current density profile in the corresponding 2D simulation[2] is, by giving the amount of loop voltage needed to increase the safety factor on axis to unity. This gives a measure of how much flux pumping is needed to prevent sawtoothing in the 3D simulation.

It can be seen that cases with a higher central pressure gradient tend to be sawtooth-free, which is consistent with the results presented in Chapter 4. As some cases have significantly higher values of Δ_{2D} than the cases discussed in the previous chapter, it is now possible to see a dependency of the boundary between sawtoothing and sawtooth-free cases on this parameter. The larger Δ_{2D}, the more difficult it is to compensate the central peaking of the current density by flux pumping. Therefore, cases with large Δ_{2D} tend to exhibit sawtoothing. In the following, the individual cases are discussed in more detail.

[2]The value of q_0 has been taken from the 2D simulation at the point in time corresponding to the end of the respective 3D simulation.

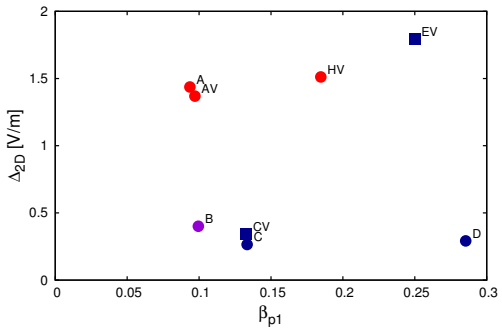

Figure 5.5: Overview of all simulations. Blue symbols represent cases that are sawtooth-free, red symbols represent cases with sawtoothing behavior and the violet symbol marks a case where sawtooth-like events are separated by phases that show the characteristics of a sawtooth-free state. Squares mark cases with higher viscosity (see Table 5.2). β_{p1} and Δ_{2D} are defined in Equations (4.7) and (4.8).

5.2.1 Sawtooth-free cases

As discussed in Chapter 4, sawtoothing is prevented in cases where the central safety factor can be kept from falling significantly below unity by flux pumping. Figure 5.6 compares the safety factor profile for one of these cases ('EV') to the safety factor profile in the corresponding 2D simulation. The flux pumping responsible for the difference between the two profiles, is due to the dynamo loop voltage in the plasma center. The plot on the right side of Figure 5.6 shows the strength of this dynamo loop voltage $-(\mathbf{v}\times\mathbf{B})_{\phi,\Delta} = -[(\mathbf{v}\times\mathbf{B})_{\phi,3D,n=0} - (\mathbf{v}\times\mathbf{B})_{\phi,2D}]$ and compares it to how much the central current density profile in the 3D simulation is flattened with respect to the 2D simulation. It can be seen that the dynamo loop voltage is entirely responsible for the current density flattening in this case. As expected from the large value of $\mu_0\chi_\perp/\eta = 680$, the dynamo loop voltage effect dominates over the resistivity flattening effect in all of the four sawtooth-free cases.

The characteristic $(m = 1, n = 1)$ convection cell that generates the dynamo loop voltage is shown in Figure 5.7 for case 'EV' and in Figure 5.9 for case 'C'. Figures 5.8 and 5.10 show the magnetic field line structure for the two cases and the respective points in time and toroidal angles. As mentioned before, these Poincaré plots have to be interpreted with care as very small deviations in the safety factor profile have a great impact on the appearance of the Poincaré plot. For instance, in these cases the $n = 2$ harmonic appears to be dominant although the $n = 1$ harmonic contains a much higher magnetic

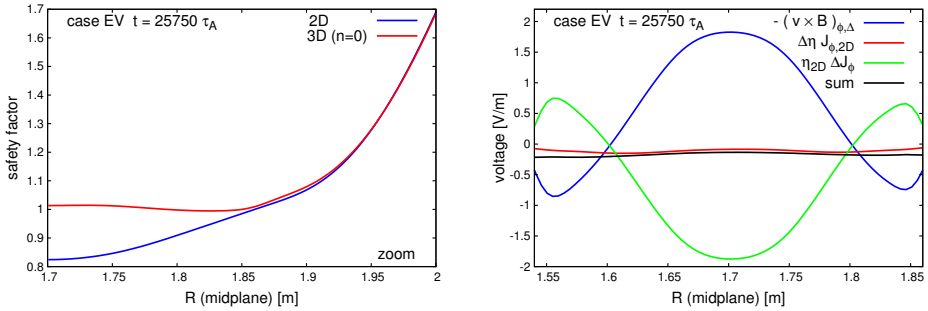

Figure 5.6: Left: Safety factor profile during sawtooth-free stationary state in a 3D simulation and safety factor profile of the corresponding 2D simulation at the same point in time. Right: The strength of the dynamo loop voltage (blue) is compared to the amount of voltage that is necessary to account for the difference in central current density between the 3D and the 2D simulation (green). Resistivity flattening (red) does not play a role in this case. This plot only shows the plasma center where $q \approx 1$. The quantities $\Delta\eta J_{\phi,2D}$ and $\eta_{2D}\Delta J_\phi$ are defined as in Equation (4.6).

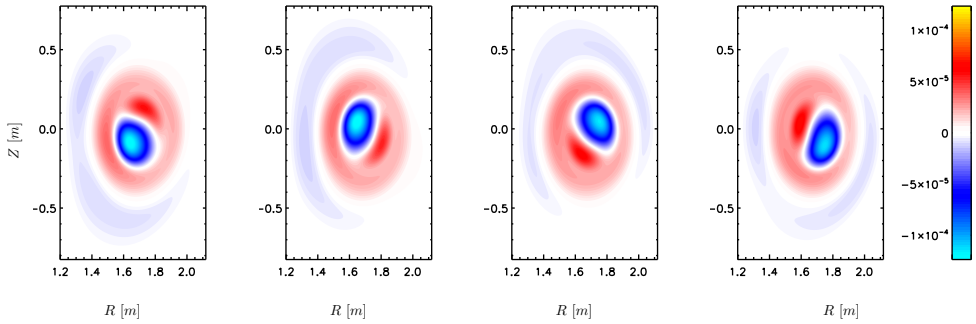

Figure 5.7: Case 'EV': $(m = 1, n = 1)$ convection cell. Plots show the difference between the poloidal velocity stream function U in the 3D simulation and the corresponding 2D simulation for toroidal angles $0°, 90°, 180°, 270°$ ($t = 25750\tau_A$, M3D-C^1 units).

energy as will be seen in the following.

The main characteristics of all sawtooth-free cases are summarized in Figure 5.11. The kinetic and magnetic energies are dominated by the $n = 1$ toroidal Fourier harmonic. Shortly after the onset of the instability, the $n = 1$ mode becomes approximately stationary, except for case 'CV' where it exhibits oscillations. Note that in cases 'C', 'D' and 'CV', the plasma state does not become perfectly stationary because in these cases, the safety factor at the edge still changes in time as the loop voltage is not feedback controlled. When run out further, the decreasing value of q at the edge eventually causes the simulations to crash. In future studies, this could be avoided by switching on the feedback control on the applied loop voltage at some point during the

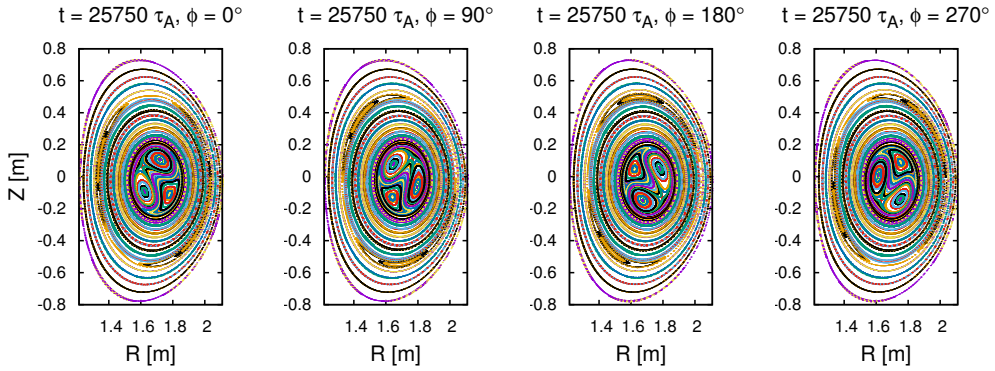

Figure 5.8: Case 'EV': Poincaré plots for different toroidal angles.

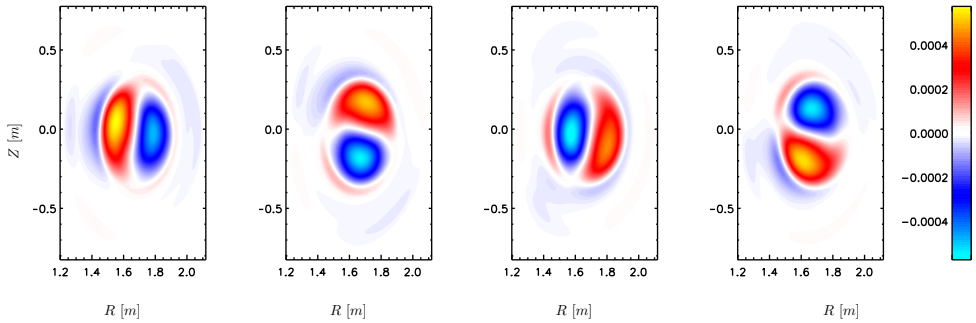

Figure 5.9: Case 'C': $(m = 1, n = 1)$ convection cell. Plots show the difference between the poloidal velocity stream function U in the 3D simulation and the corresponding 2D simulation for toroidal angles 0°, 90°, 180°, 270° ($t = 23000\tau_A$, M3D-C^1 units).

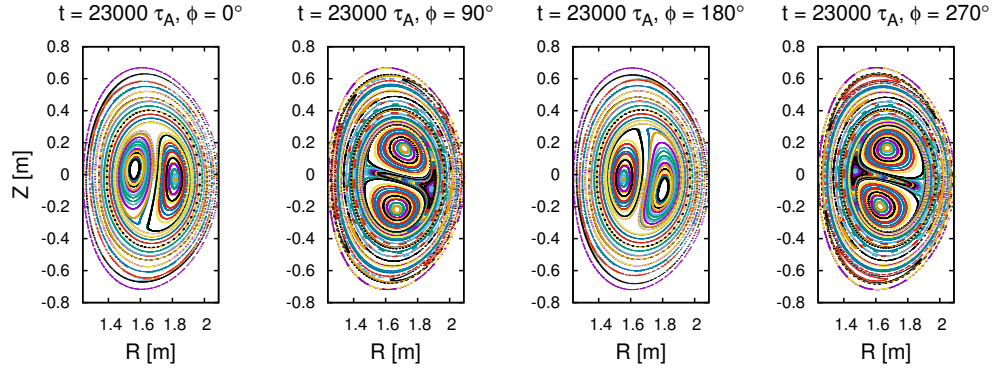

Figure 5.10: Case 'C': Poincaré plots for different toroidal angles.

simulations, which would be consistent with experiments.

As can be seen from the time evolution of the safety factor profile, case 'EV' does not go into the stationary state as soon as q_0 reaches unity, instead q_0 continues to decrease until a large amplitude sawtooth restores $q_0 = 1$. This is due to the fact that in case 'EV', q_0 is decreased by increasing the magnetic shear in the central region of the plasma (see Figure 5.3). Thus, when q_0 reaches unity, the magnetic shear is already too high to allow for a quasi-interchange instability to set in. Only after the sawtooth has flattened the central safety factor profile, the conditions for the stationary state are set.

However, as the time evolution of the minimal value of the safety factor in case 'C' shows, this first large amplitude sawtooth is not necessary for the stationary state to develop. In this case the magnetic shear in the central plasma region is low when the safety factor approaches unity, so that as soon as $q_{\min} = 1$, it is kept at this value.

As expected, the cases with lower viscosity ('C', 'D') have a larger $n = 1$ kinetic energy because the $(m = 1, n = 1)$ flow is less damped. As a consequence, the dynamo loop voltage effect is stronger than in the cases with higher viscosity (by a factor two in the case of 'C' and 'CV').

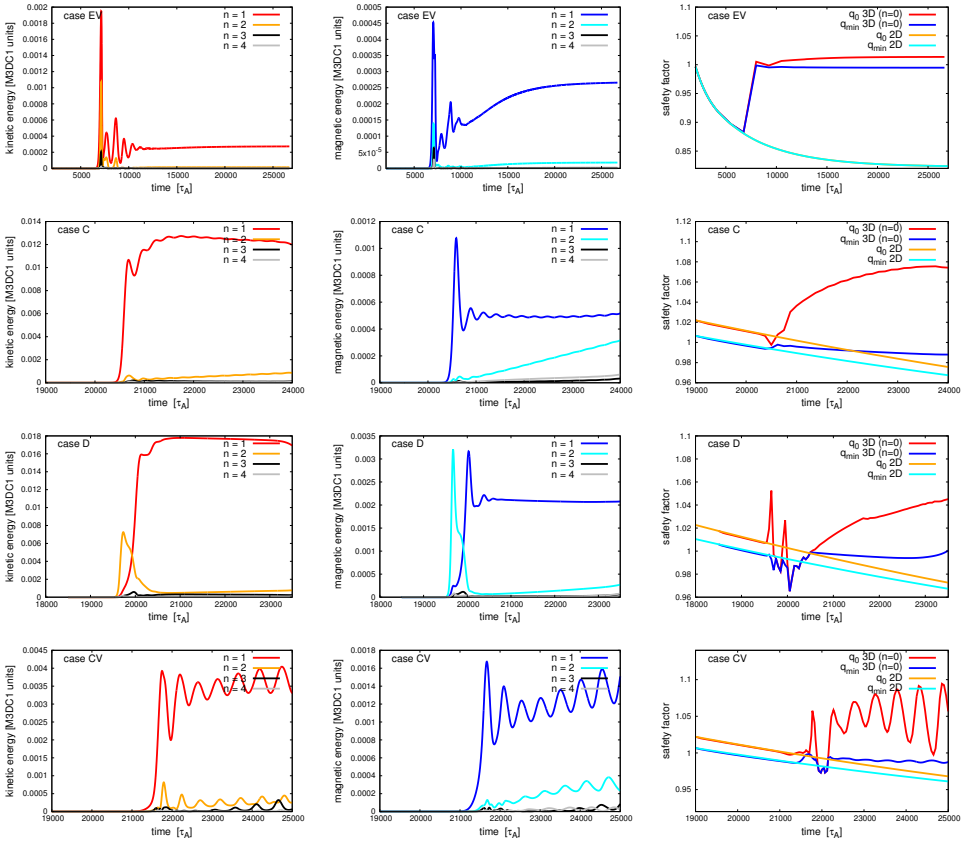

Figure 5.11: Sawtooth-free cases: Plots on the left side and in the center show the time evolution of the kinetic and magnetic energies in the different toroidal harmonics, respectively. The plots on the right side compare the time evolution of the minimum value of the safety factor and its value on axis in the 3D simulation with the respective quantities in the corresponding 2D axisymmetric simulation. Note, that the safety factor profiles of the 3D simulations are calculated from the toroidally averaged magnetic field.

5.2.2 Sawtooth-like behavior

If the central safety factor profile is not prevented from decreasing below unity, repeating reconnection events restore $q_0 = 1$. Figure 5.12 shows the safety factor profile before and after such a sawtooth-like event. The Poincaré plots in Figure 5.13 show how the magnetic field line structure is reorganized during the reconnection process.

Figure 5.14 provides an overview of the cases that exhibit sawtooth-like reconnection events. Note that although the reconnection events share some features with sawteeth, the evolution of the safety factor profiles does not correspond to a typical evolution during experimentally observed sawteeth.

The time evolution of the kinetic and magnetic energies of case 'AV' shows that the plasma becomes entirely axisymmetric after each crash as expected for complete Kadomtsev reconnection. Although, during the reconnection events in case 'A', reconnection does also complete, there is a residual magnetic and kinetic energy left between the crashes. This might be due to the lower viscosity. Flows in the central plasma that are initiated by the crash are damped less and can deform the magnetic field, manifesting itself in the kinetic and magnetic energies. A residual magnetic perturbation after a sawtooth crash might be relevant for the seeding of neoclassical tearing modes [105, 106].

In case 'B', the plasma also exhibits full reconnection events as can be seen for one example on the Poincaré plots in Figure 5.15. However, the time between the individual events is significantly longer than in the other cases. The phases in between feature the characteristics of the sawtooth-free helical states like the important, approximately stationary $n = 1$ kinetic and magnetic

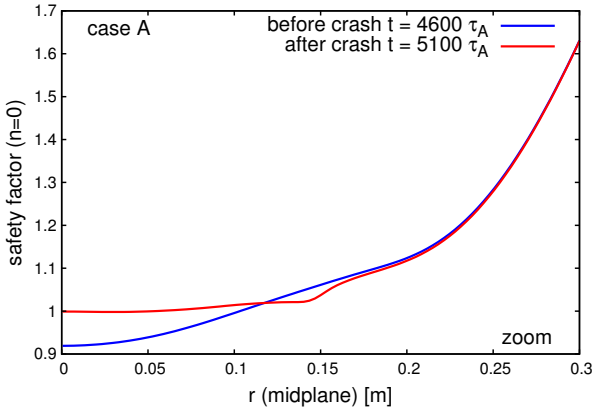

Figure 5.12: Safety factor profile before and after a sawtooth-like crash.

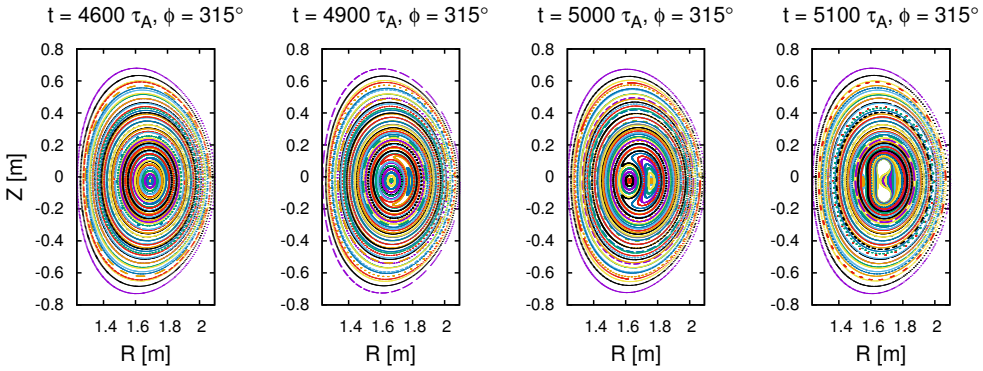

Figure 5.13: Case 'A': Poincaré plots for different points in time during a reconnection event.

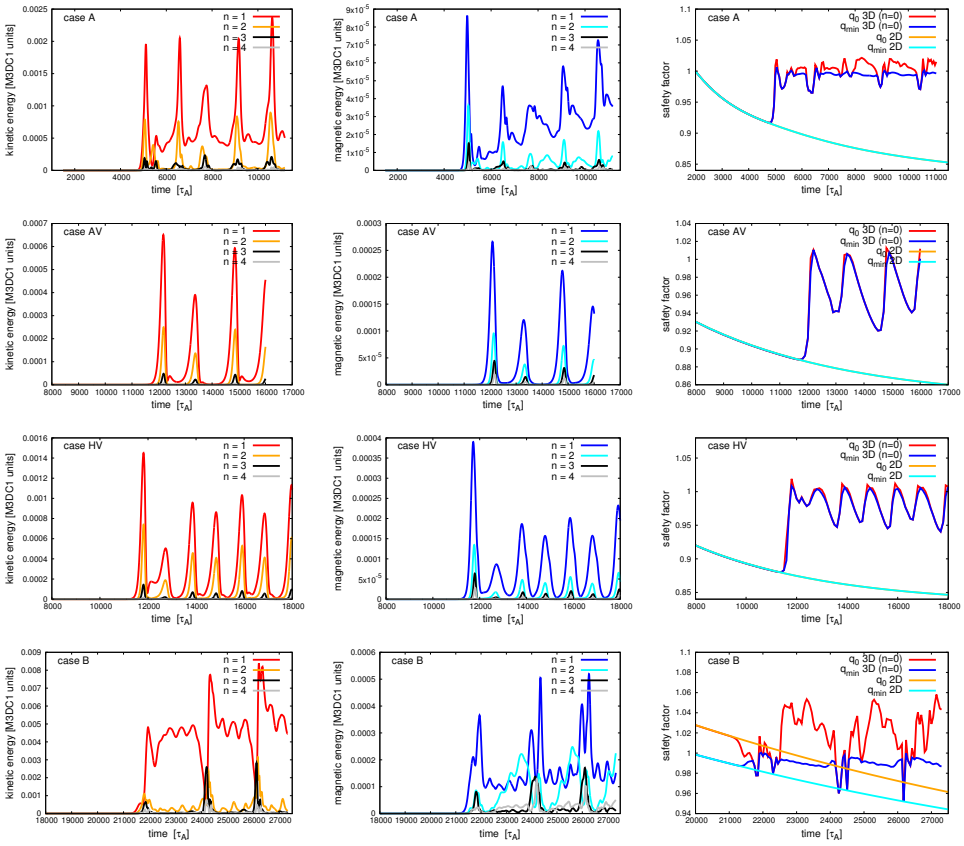

Figure 5.14: Cases that exhibit a sawtooth-like behavior: Plots on the left side and in the center show the time evolution of the kinetic and magnetic energies in the different toroidal harmonics, respectively. The plots on the right side compare the time evolution of the minimum value of the safety factor and its value on axis in the 3D simulation with the respective quantities in the corresponding 2D axisymmetric simulation.

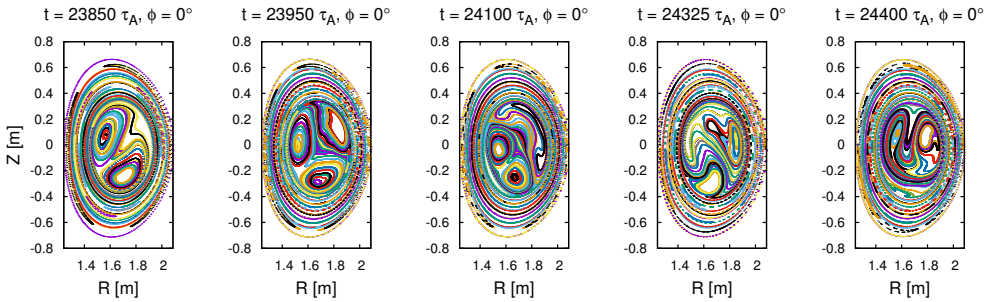

Figure 5.15: Case 'B': Poincaré plots for different points in time during a sawtooth-like reconnection event.

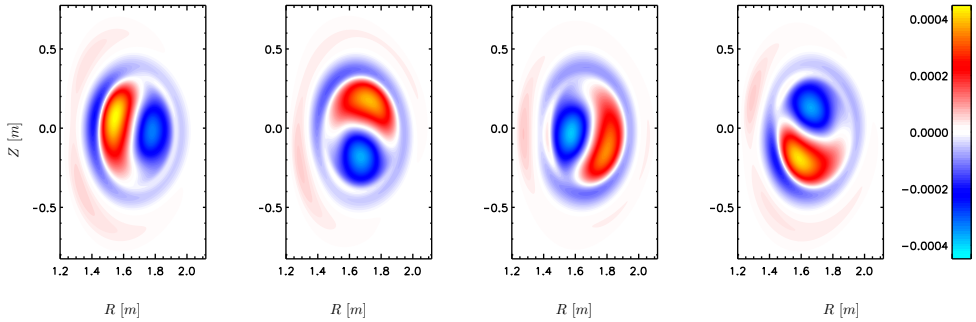

Figure 5.16: Case 'B': $(m = 1, n = 1)$ convection cell. Plots show the difference between the poloidal velocity stream function U in the 3D simulation and the corresponding 2D simulation for toroidal angles $0°, 90°, 180°, 270°$ during the quiescent phase between two reconnection events ($t = 25250\tau_A$, M3D-C^1 units).

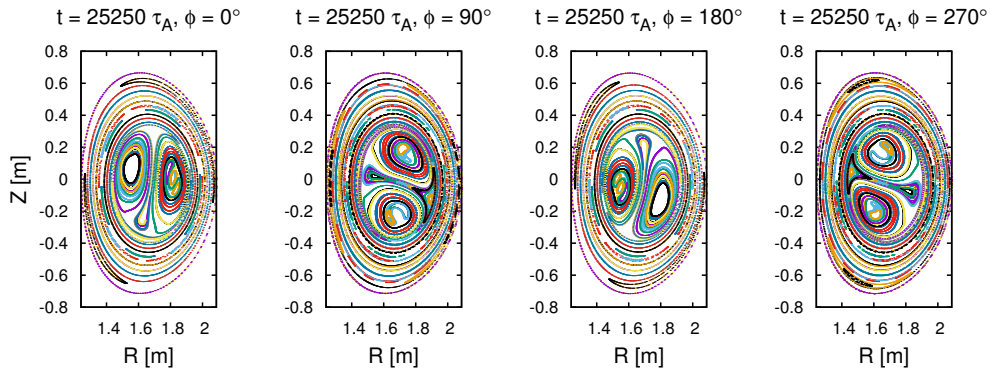

Figure 5.17: Case 'B': Poincaré plots for different toroidal angles during the quiescent phase between two sawtooth events.

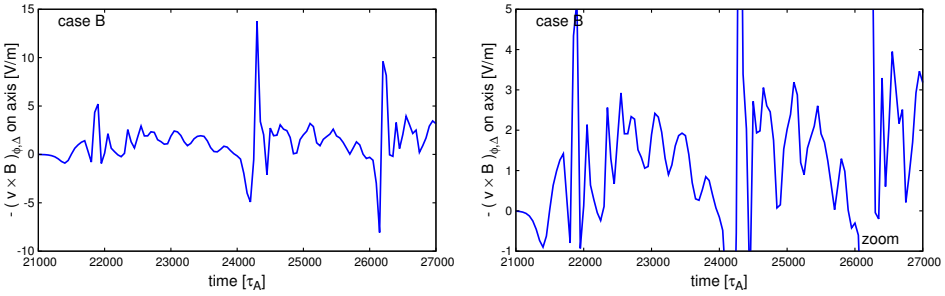

Figure 5.18: Time evolution of the dynamo loop voltage on axis. The plot on the right side shows a close-up.

energies, the typical $(m = 1, n = 1)$ flow pattern shown in Figure 5.16, and a similar magnetic field line structure which is shown in Figure 5.17.

These phases where the central safety factor profile is clamped close to unity might be possible in this case because compared to the other cases with a sawtooth-like behavior described here, it has a lower value of Δ_{2D}, and compared to the sawtoothing cases discussed in Chapter 4, it has a larger value of β_{p1}. The latter strengthens the dynamo loop voltage and the former makes it easier for the dynamo loop voltage to compensate the central current peaking.

The time evolution of the strength of this dynamo loop voltage on axis is traced in Figure 5.18. As seen in other sawtoothing cases discussed in the previous chapter it has a large spike at each crash, but in this case it does not vanish in between the crashes. The dynamo loop voltage rather slowly decreases which might explain why at some point the central safety factor falls and the next reconnection event occurs. Note that from the plot showing the time evolution of q_0 and $q_{\min}$ for case 'B' in Figure 5.14, it can be seen that this decrease of the central safety factor happens on a much faster time scale than the decrease of q in the corresponding 2D simulation. This might be due to the fact that in the 2D simulation the profile changes over the entire plasma radius while in the 3D simulation it only changes significantly inside a midplane minor radius of $r \approx 0.15$. On this shorter length scale resistive diffusion leads to a faster decrease of q.

Why the dynamo loop voltage decreases, needs to be further investigated. Another open question is, if this phenomenon could be related to some cases of extended sawtooth periods in experiments. In any case, this type of behavior would need to be studied by means of more simulations with varying parame-

ters, especially since the presented simulations at low viscosity are at the edge of what the used mesh is able to resolve.

Chapter 6

Summary & Outlook

The aim of this work was to advance the theoretical understanding of magnetic flux pumping in Hybrid tokamak discharges. To this end, 3D nonlinear resistive MHD simulations in toroidal geometry have been performed by means of the high-order finite element code M3D-C[1]. A mechanism that provides magnetic flux pumping in 3D nonlinear MHD simulations of tokamak plasmas has been proposed in [1]. In this reference, a stationary state is described which is characterized by a region in the plasma center where the magnetic shear is very low and the safety factor has a value close to unity. This state features a helical $(m = 1, n = 1)$ perturbation of the plasma core and in particular a strong $(m = 1, n = 1)$ convection cell. It is proposed that this stationary perturbation is the result of a saturated quasi-interchange instability and that it leads to magnetic flux pumping via two different processes. First, the helical flow flattens the central current density profile by flattening the temperature and thus the resistivity profile via convection, a mechanism whose effectiveness depends on the stiffness of the temperature profile. And second, the flow combines with the perturbation of the magnetic field to generate an effective negative loop voltage via a dynamo effect.

Summary

In the first part of this work, it has been analyzed in more detail how this flux pumping mechanism works and under which conditions it sustains itself to prevent sawtoothing in the simulations. An induction equation linearized around its 2D axisymmetric solution is derived in order to illustrate how 3D

effects, namely the resistivity flattening effect and the dynamo loop voltage effect, can alter the central current density. It provides expressions for the strength of the two effects which can be quantitatively compared to each other and to the amount of flux pumping necessary to maintain $q_0 \approx 1$ in a given nonlinear simulation.

3D nonlinear MHD simulations are presented in which a heat source works towards peaking the central current density profile such that in the absence of 3D instabilities, the safety factor profile would have a central value below unity. A large set of such simulations is obtained by varying β, the perpendicular heat diffusion coefficient together with the strength of the applied heat source, and the peakedness of the heat source. It is found that, consistent with previous theoretical findings, above a certain threshold in β, the obtained asymptotic states are stationary (or, for high values of $\mu_0\chi_\perp/\eta$, quasi-stationary oscillating) sawtooth-free states with a 3D helically perturbed core. The threshold in β is due to the fact that the quasi-interchange instability which generates the helical convection cell needed for the flux pumping mechanisms is pressure-driven.

Below this threshold in β, the asymptotic states are characterized by repeating sawtooth-like cycles in each of which q_0 decreases to values significantly below unity before $q_0 \approx 1$ is restored by a Kadomtsev-like magnetic reconnection process. It is shown that simulations develop a sawtooth-free asymptotic state if and only if the combined strength of the two current flattening mechanisms equals or exceeds the amount of flux pumping that is necessary to balance the tendency of the central safety factor profile to decrease below unity.

By separating the two flux pumping mechanisms, it is confirmed that the importance of the resistivity flattening effect decreases with increasing $\mu_0\chi_\perp/\eta$ as the convective flattening of the temperature profile becomes ineffective for stiff temperature profiles. For ratios of the resistive to the heat diffusion time scale that are realistic for typical Hybrid discharges, the dynamo loop voltage effect therefore dominates over the resistivity flattening effect. The strength of the dynamo loop voltage mechanism adapts to the strength of the resistivity flattening effect such that it always provides the amount of flux pumping which is missing to keep $q_0 \approx 1$ (as long as β is sufficiently high). It is proposed that this self-regulation is due to the fact that by providing more flux pumping than necessary, the dynamo loop voltage effect would weaken itself by driving the

central value of the safety factor above unity which would have a stabilizing effect on the quasi-interchange instability.

In order to understand in more detail how the dynamo loop voltage is generated, a linear stability analysis of a 2D equilibrium with $q \approx 1$ and low magnetic shear in the central plasma region has been performed by means of the CASTOR3D code. It is confirmed that the most unstable mode in this configuration can be characterized as a quasi-interchange instability. Furthermore, it is shown that by combining the resulting linear velocity and magnetic field perturbations, a dynamo loop voltage can be calculated which has a comparable shape and strength as the dynamo loop voltage in the 3D nonlinear simulations.

In contrast, it is found that the linear perturbations resulting from an internal kink instability do not combine to a dynamo loop voltage of comparable strength. Similarly, for a quasi-interchange unstable equilibrium with slightly reversed central magnetic shear and two $q = 1$ surfaces, the resulting linear perturbations do not combine to a comparable dynamo loop voltage. Although this finding cannot be directly applied to the interpretation of stationary states in 3D nonlinear simulations as the former is based on a 2D equilibrium while the latter feature a 3D helical core, this might be related to the aforementioned self-regulation mechanism of the dynamo loop voltage effect.

The second part of this work was focused on exploring the path towards more realistic 3D nonlinear MHD simulations of Hybrid discharges. The simulations are based on the geometry of the ASDEX Upgrade tokamak and are set up to mimic the qualitative evolution of the central safety factor profile during the current ramp-up at the beginning of a discharge. Before, the focus was put on the asymptotic states of the simulations, and the conditions for the flux pumping mechanisms to set in, namely low central magnetic shear and $q \approx 1$ in the plasma core, had been set up by a large amplitude reconnection event at the beginning of each simulation. In contrast, the more realistic simulations are started from a safety factor profile that is flat and above unity in the center, which is then ramped down so that the plasma state self-consistently enters the region of instability for $(m = 1, n = 1)$ modes.

Within this set of simulations, again both cases exhibiting sawtooth-like reconnection events and sawtooth-free cases are found. The way these different types of behavior are distributed over the parameter space is consistent with the previous findings. In addition, the results indicate that the critical value

of β for sawtooth-free states depends on how much the current density profile tends to centrally peak due to the central heat source. It is also shown that if the central safety factor profile is sufficiently flat when the stability boundary is approached, which is the case during the current ramp-up phase for a realistic Hybrid discharge, the plasma directly goes into a sawtooth-free state without an initial large amplitude sawtooth-like event.

Regarding the simulations within both sets which develop a sawtooth-like cycling behavior, it should be mentioned that they are not expected to reproduce detailed features of realistic sawteeth, like the long quiescent ramp phase or the fast crash time, as this requires a more realistic value for the heat diffusion anisotropy and a lower value for the resistivity while including two-fluid effects, which was not possible due to numerical reasons and limited computational resources, respectively. Nevertheless, two interesting special types of behavior have been found among these simulations.

First, in a few simulations the reconnection process during the sawtooth-like events does not complete, but the growth of the $(m = 1, n = 1)$ island stops and reverses before the island can entirely replace the plasma core. This behavior is only found in a region of the parameter space where the linear drive for the internal kink instability is particularly small, but in a more complete physics model, additional stabilizing effects might enable a similar behavior in more general cases and might possibly help to understand the phenomenon of incomplete sawtooth reconnection in experiments.

Second, in a simulation at the border between sawtooth-like cycling and sawtooth-free cases within the more realistic set, the full reconnection cycles are separated by quiescent phases that show the characteristic features of sawtooth-free states. This finding might be related to experimental observations like the intermittent recurrence of sawteeth in Hybrid discharges or extended sawtooth periods in sawtoothing discharges.

Outlook

First further steps on the path towards improved, more realistic 3D nonlinear MHD simulations of Hybrid discharges would be the inclusion of sheared toroidal rotation, modeling the realistic evolution of the discharge by switching on the feedback control on the applied loop voltage after the current ramp-up phase, and using even more realistic plasma parameters by making use of fu-

ture extended computational resources and the result of ongoing code efficiency improvements.

In addition, further numerical studies are planned with the aim of examining the effect of an externally excited $(m = 1, n = 1)$ perturbation in the plasma core and the effect of a $(m = 3, n = 2)$ tearing mode which, as indicated by experimental results in DIII-D [86], might play a role in providing magnetic flux pumping in Hybrid discharges.

Moreover, closer comparisons of the obtained theoretical findings to experimental results in ASDEX Upgrade are planned. Based on these findings, it is expected that a threshold in β for flux pumping to occur is observed and that this threshold depends on how low q_0 should be according to the applied loop voltage and the amount of on-axis current drive and heating. This could be verified in a set of discharges using central co-ECCD at various values of β, ideally with the possibility of measuring a $(m = 1, n = 1)$ flow in the plasma center.

Acknowledgments

First of all, I would like to thank my adviser, Sibylle Günter, for guiding me and teaching me so much on the path towards completing this thesis, for the many frank and fruitful discussions, helpful advice and good ideas, for always finding time to care about my work and for all the phone calls the most densely filled with physics possible. In the same way, I would like to thank my co-adviser at PPPL, Steve Jardin, for his uncountable contributions to the work presented in this thesis, for the many valuable physics discussions in which I learned a lot, for always being ready to help and for his indispensable support in questions regarding M3D-C^1. I enjoyed working with my two advisers both on a professional and personal level and I highly appreciate their kindness and sense of humor.

Also, I would like to thank Matthias Hölzl, the person who first explained to me what a tokamak is and has ever since supported me with physics, technical and personal advice, innumerous helpful discussions on important details as well as the big picture and with motivation when it was most needed. I would like to thank Karl Lackner for the many enjoyable and interesting discussions and illuminating ideas which shaped the content of this thesis significantly. Furthermore, I would like to thank Erika Strumberger for her kind, reliable and indispensable help regarding the CASTOR calculations. I would also like to thank Valentin Igochine for interesting discussions on experimental observations in ASDEX Upgrade and for kindly providing me with the data for the figure on sawtooth oscillations. On the PPPL side, I would like to thank Nate Ferraro and David Pfefferlé for helpful physics discussions and great support regarding M3D-C^1, Stuart Hudson for inspiring discussions on the structure of magnetic fields in tokamaks, and Jin Chen for valuable technical support regarding M3D-C^1.

Moreover, I would like to thank Margaret Carideo for taking care of my maximally complicated visa and funding situation with a smile. The simu-

lations presented in this thesis have been run on the local PPPL computing cluster and I gratefully acknowledge the support team responsible for these resources. Financial support for this thesis has been provided through the PhD fellowship of the Max-Planck/Princeton Research Center for Plasma Physics. The Center has enabled many fruitful collaborations and I am very thankful that it has given me the opportunity to spend a significant part of the time I worked on this thesis at PPPL. In particular, I would like to thank Amitava Bhattacharjee for making me feel welcome at PPPL's theory department.

On a personal level, I would like to thank my friends and colleagues in Princeton for the strong support and for making me have a great time, in particular Sofia, Robert, Vinícius, Verena, Stefan, Josefine, Joaquim, Mirjam, David, Lucie, Eero, Sanni, Daniel, Max, Salomon, Pallavi, Luca, Kenan, Caoxiang, Tess, Tim, Katie, Brian and Sören. Also, I would like to thank my family and my friends in Germany and scattered around the world, in particular Matthias, *meine Kölner Mädsche* Johanna, Rita and Henrike, and *meine Liebchenfreundin* Maria Isabel for always being there for me despite a distance of thousands of miles.

I would like to thank my father for being genuinely interested and supporting me most affectionately in whatever I do, and for teaching me resilience by leading as an example. His willingness to cross the ocean so many times in order to be with us has meant a lot to me. Finally, I would like to thank the person whose tireless and loving support has an importance to me which is beyond words, my beloved husband Johannes, *mein Ein und Alles*.

Bibliography

[1] S. C. Jardin, N. Ferraro, and I. Krebs, "Self-organized stationary states of tokamaks," *Physical Review Letters*, vol. 115, Nov 2015.

[2] T. J. Team, "The JET project – Design proposal for the Joint European Torus," tech. rep., Commission of the European Communities, 1976.

[3] J. L. Luxon, T. C. Simonen, R. D. Stambaugh, and the DIII-D Team, "Overview of the DIII-D fusion science program," *Fusion Science and Technology*, vol. 48, pp. 807–827, Oct 2005.

[4] A. Herrmann and O. Gruber, "Chapter 1: ASDEX Upgrade - Introduction and overview," *Fusion Science and Technology*, vol. 44, pp. 569–577, Nov 2003.

[5] S. Wu, "An overview of the EAST project," *Fusion Engineering and Design*, vol. 82, pp. 463–471, Oct 2007.

[6] M. Kwon, Y. K. Oh, H. L. Yang, H. K. Na, Y. S. Kim, J. G. Kwak, W. C. Kim, J. Y. Kim, J. W. Ahn, Y. S. Bae, *et al.*, "Overview of KSTAR initial operation," *Nuclear Fusion*, vol. 51, p. 094006, Aug 2011.

[7] M. Shimada, D. J. Campbell, V. Mukhovatov, M. Fujiwara, N. Kirneva, K. Lackner, M. Nagami, V. D. Pustovitov, N. Uckan, J. Wesley, *et al.*, "Chapter 1: Overview and summary," *Nuclear Fusion*, vol. 47, pp. S1–S17, Jun 2007.

[8] J. Wesson, *Tokamaks*. Oxford: Clarendon Press, 3rd ed., 2004.

[9] R. J. Buttery, S. Gnter, G. Giruzzi, T. C. Hender, D. Howell, G. Huysmans, R. J. La Haye, M. Maraschek, O. Reimerdes, H.and Sauter, *et al.*, "Neoclassical tearing modes," *Plasma Physics and Controlled Fusion*, vol. 42, pp. B61–B73, Dec 2000.

[10] A. C. C. Sips, for the Steady State Operation and the Transport Physics topical groups of the International Tokamak Physics Activity, "Advanced scenarios for ITER operation," *Plasma Physics and Controlled Fusion*, vol. 47, pp. A19–A40, Apr 2005.

[11] O. Gruber, R. C. Wolf, R. Dux, C. Fuchs, S. Günter, A. Kallenbach, K. Lackner, M. Maraschek, P. J. McCarthy, H. Meister, *et al.*, "Stationary H-Mode discharges with internal transport barrier on ASDEX Upgrade," *Physical Review Letters*, vol. 83, pp. 1787–1790, Aug 1999.

[12] A. Staebler, A. C. C. Sips, M. Brambilla, R. Bilato, R. Dux, O. Gruber, J. Hobirk, L. D. Horton, C. F. Maggi, A. Manini, *et al.*, "The improved H-mode at ASDEX Upgrade: a candidate for an ITER hybrid scenario," *Nuclear Fusion*, vol. 45, pp. 617–625, Jun 2005.

[13] C. C. Petty, M. E. Austin, C. T. Holcomb, R. J. Jayakumar, R. J. La Haye, T. C. Luce, M. A. Makowski, P. A. Politzer, and M. R. Wade, "Magnetic-flux pumping in high-performance, stationary plasmas with tearing modes," *Physical Review Letters*, vol. 102, Jan 2009.

[14] J. P. Freidberg, *Ideal Magnetohydrodynamics*. New York: Plenum Press, first ed., 1987.

[15] J. P. Freidberg, *Ideal MHD*. Cambridge University Press, 2014.

[16] D. Biskamp, *Magnetic Reconnection in Plasmas*. Cambridge University Press, 2000.

[17] D. Biskamp, *Nonlinear Magnetohydrodynamics*. Cambridge University Press, 1993.

[18] S. I. Vainshtein and Y. B. Zeldovich, "Origin of magnetic fields in astrophysics (turbulent dynamo mechanisms)," *Soviet Physics Uspekhi*, vol. 15, pp. 159–172, Feb 1972.

[19] T. G. Cowling, "The magnetic field of sunspots," *Monthly Notices of the Royal Astronomical Society*, vol. 94, pp. 39–48, Nov 1933.

[20] D. Lortz, "Exact solutions of the hydromagnetic dynamo problem," *Plasma Physics*, vol. 10, pp. 967–972, Jan 1968.

[21] M. N. Bussac, R. Pellat, D. Edery, and J. L. Soule, "Internal kink modes in toroidal plasmas with circular cross sections," *Physical Review Letters*, vol. 35, pp. 1638–1641, Dec 1975.

[22] F. L. Waelbroeck and R. D. Hazeltine, "Stability of low-shear tokamaks," *Physics of Fluids*, vol. 31, no. 5, p. 1217, 1988.

[23] R. J. Hastie and T. C. Hender, "Toroidal internal kink stability in tokamaks with ultra flat q profiles," *Nuclear Fusion*, vol. 28, pp. 585–594, Apr 1988.

[24] S. C. Jardin, N. Ferraro, J. Breslau, and J. Chen, "Multiple timescale calculations of sawteeth and other global macroscopic dynamics of tokamak plasmas," *Computational Science & Discovery*, vol. 5, p. 014002, May 2012.

[25] S. Jardin, "A triangular finite element with first-derivative continuity applied to fusion MHD applications," *Journal of Computational Physics*, vol. 200, pp. 133–152, Oct 2004.

[26] S. Jardin, *Computational methods in plasma physics*. Chapman & Hall/CRC Computational Science, CRC Press, Taylor & Francis Group, 2010.

[27] C. Strang and G. Fix, *An analysis of the finite element method*. Prentice-Hall, 1973.

[28] V. Igochine, ed., *Active Control of Magneto-hydrodynamic Instabilities in Hot Plasmas*. Springer-Verlag Berlin Heidelberg, 2015.

[29] N. M. Ferraro, S. C. Jardin, L. L. Lao, M. S. Shephard, and F. Zhang, "Multi-region approach to free-boundary three-dimensional tokamak equilibria and resistive wall instabilities," *Physics of Plasmas*, vol. 23, p. 056114, May 2016.

[30] S. Jardin, J. Breslau, and N. Ferraro, "A high-order implicit finite element method for integrating the two-fluid magnetohydrodynamic equations in two dimensions," *Journal of Computational Physics*, vol. 226, pp. 2146–2174, Oct 2007.

[31] N. M. Ferraro, *Non-Ideal Effects on the Stability and Transport of Magnetized Plasmas*. PhD thesis, Princeton University, 2008.

[32] J. Breslau, N. Ferraro, and S. Jardin, "Some properties of the M3D-C1 form of the three-dimensional magnetohydrodynamics equations," *Physics of Plasmas*, vol. 16, p. 092503, Sep 2009.

[33] N. Ferraro and S. Jardin, "Calculations of two-fluid magnetohydrodynamic axisymmetric steady-states," *Journal of Computational Physics*, vol. 228, pp. 7742–7770, Nov 2009.

[34] S. von Goeler, W. Stodiek, and N. Sauthoff, "Studies of internal disruptions and m = 1 oscillations in tokamak discharges with soft-x-ray tecniques," *Physical Review Letters*, vol. 33, pp. 1201–1203, Nov 1974.

[35] R. J. Hastie, "Sawtooth instability in tokamak plasmas," *Astrophysics and Space Science*, vol. 256, no. 1/2, pp. 177–204, 1997.

[36] I. T. Chapman, "Controlling sawtooth oscillations in tokamak plasmas," *Plasma Physics and Controlled Fusion*, vol. 53, p. 013001, Nov 2010.

[37] D. J. Campbell, R. D. Gill, C. W. Gowers, J. A. Wesson, D. V. Bartlett, C. H. Best, S. Coda, A. E. Costley, A. Edwards, S. E. Kissel, *et al.*, "Sawtooth activity in ohmically heated JET plasmas," *Nuclear Fusion*, vol. 26, pp. 1085–1092, Aug 1986.

[38] E. D. Fredrickson, J. D. Callen, K. McGuire, J. D. Bell, R. J. Colchin, P. C. Efthimion, K. W. Hill, R. Izzo, D. R. Mikkelsen, D. A. Monticello, *et al.*, "Heat pulse propagation studies in TFTR," *Nuclear Fusion*, vol. 26, pp. 849–862, Jul 1986.

[39] D. Wróblewski and L. L. Lao, "Determination of the safety factor in sawtoothing discharges in DIII-D," *Physics of Fluids B: Plasma Physics*, vol. 3, no. 10, p. 2877, 1991.

[40] A. Mück, T. P. Goodman, M. Maraschek, G. Pereverzev, F. Ryter, H. Zohm, and the ASDEX Upgrade Team, "Sawtooth control experiments on ASDEX Upgrade," *Plasma Physics and Controlled Fusion*, vol. 47, pp. 1633–1655, Sep 2005.

[41] A. W. Edwards, D. J. Campbell, W. W. Engelhardt, H. U. Fahrbach, R. D. Gill, R. S. Granetz, S. Tsuji, B. J. D. Tubbing, A. Weller, J. Wesson, *et al.*, "Rapid collapse of a plasma sawtooth oscillation in the JET tokamak," *Physical Review Letters*, vol. 57, pp. 210–213, Jul 1986.

[42] Y. Nagayama, K. M. McGuire, M. Bitter, A. Cavallo, E. D. Fredrickson, K. W. Hill, H. Hsuan, A. Janos, W. Park, G. Taylor, *et al.*, "Analysis of sawtooth oscillations using simultaneous measurement of electron cyclotron emission imaging and x-ray tomography on TFTR," *Physical Review Letters*, vol. 67, pp. 3527–3530, Dec 1991.

[43] A. Letsch, H. Zohm, F. Ryter, W. Suttrop, A. Gude, F. Porcelli, C. Angioni, and I. Furno, "Incomplete reconnection in sawtooth crashes in ASDEX Upgrade," *Nuclear Fusion*, vol. 42, pp. 1055–1059, Aug 2002.

[44] F. Porcelli, D. Boucher, and M. N. Rosenbluth, "Model for the sawtooth period and amplitude," *Plasma Physics and Controlled Fusion*, vol. 38, pp. 2163–2186, Dec 1996.

[45] H. K. Park, N. C. Luhmann, A. J. H. Donn, I. G. J. Classen, C. W. Domier, E. Mazzucato, T. Munsat, M. J. van de Pol, and Z. Xia, "Observation of high-field-side crash and heat transfer during sawtooth oscillation in magnetically confined plasmas," *Physical Review Letters*, vol. 96, May 2006.

[46] H. K. Park, A. J. H. Donn, N. C. Luhmann, I. G. J. Classen, C. W. Domier, E. Mazzucato, T. Munsat, M. J. van de Pol, and Z. Xia, "Comparison study of 2D images of temperature fluctuations during sawtooth oscillation with theoretical models," *Physical Review Letters*, vol. 96, May 2006.

[47] V. Igochine, J. Boom, I. Classen, O. Dumbrajs, S. Günter, K. Lackner, G. Pereverzev, H. Zohm, and the ASDEX Upgrade Team, "Structure and dynamics of sawteeth crashes in ASDEX Upgrade," *Physics of Plasmas*, vol. 17, no. 12, p. 122506, 2010.

[48] K. McGuire, V. Arunasalam, C. W. Barnes, M. G. Bell, M. Bitter, R. Boivin, N. L. Bretz, R. Budny, C. E. Bush, A. Cavallo, *et al.*, "High-beta operation and magnetohydrodynamic activity on the TFTR tokamak," *Physics of Fluids B: Plasma Physics*, vol. 2, no. 6, p. 1287, 1990.

[49] D. Wróblewski and R. T. Snider, "Evidence of the complete magnetic reconnection during a sawtooth collapse in a tokamak," *Physical Review Letters*, vol. 71, pp. 859–862, Aug 1993.

[50] TEXTOR Team in *Plasma Physics and Controlled Nuclear Fusion Research (Proc. 12th Int. Conf. Nice (1988)), IAEA Vienna*, vol. 1, p. 331, 1988.

[51] J. Blum, E. Lazzaro, J. O'Rourke, B. Keegan, and Y. Stephan, "Problems and methods of self-consistent reconstruction of tokamak equilibrium profiles from magnetic and polarimetric measurements," *Nuclear Fusion*, vol. 30, pp. 1475–1492, Aug 1990.

[52] M. Yamada, F. M. Levinton, N. Pomphrey, R. Budny, J. Manickam, and Y. Nagayama, "Investigation of magnetic reconnection during a sawtooth crash in a high-temperature tokamak plasma," *Physics of Plasmas*, vol. 1, no. 10, p. 3269, 1994.

[53] B. B. Kadomtsev, "Disruptive instability in tokamaks," *Sov. J. Plasma Phys.*, vol. 1, p. 389, 1975.

[54] B. Kadomtsev and O. Pogutse, "Nonlinear helical perturbations of a plasma in the tokamak," *Sov. Phys.-JETP*, vol. 38, p. 283, 1974.

[55] H. R. Strauss, "Nonlinear three-dimensional magnetohydrodynamics of noncircular tokamaks," *Phys. Fluids*, vol. 19, p. 134, 1976.

[56] J. Wesson in *Theory of fusion plasmas: proceedings of the workshop held at Villa Cipressi, Varenna, Italy, August 24-28, 1987*, 1988.

[57] A. Sykes and J. A. Wesson, "Relaxation instability in tokamaks," *Physical Review Letters*, vol. 37, pp. 140–143, Jul 1976.

[58] B. V. Waddell, M. N. Rosenbluth, D. A. Monticello, and R. B. White, "Non-linear growth of the m = 1 tearing mode," *Nuclear Fusion*, vol. 16, pp. 528–532, Jul 1976.

[59] A. Danilov, Y. Dnestrovski, D. Kostomarov, and A. Popov *Sov. J. Plasma Phys*, vol. 2, p. 93, 1976.

[60] D. Biskamp, "Magnetic reconnection via current sheets," *Physics of Fluids*, vol. 29, no. 5, p. 1520, 1986.

[61] A. Bhattacharjee, Y.-M. Huang, H. Yang, and B. Rogers, "Fast reconnection in high-Lundquist-number plasmas due to the plasmoid instability," *Physics of Plasmas*, vol. 16, no. 11, p. 112102, 2009.

[62] N. F. Loureiro, R. Samtaney, A. A. Schekochihin, and D. A. Uzdensky, "Magnetic reconnection and stochastic plasmoid chains in high-Lundquist-number plasmas," *Physics of Plasmas*, vol. 19, no. 4, p. 042303, 2012.

[63] Q. Yu, S. Günter, and K. Lackner, "Formation of plasmoids during sawtooth crashes," *Nuclear Fusion*, vol. 54, p. 072005, May 2014.

[64] S. Günter, Q. Yu, K. Lackner, A. Bhattacharjee, and Y.-M. Huang, "Fast sawtooth reconnection at realistic Lundquist numbers," *Plasma Physics and Controlled Fusion*, vol. 57, p. 014017, Nov 2014.

[65] J. A. Wesson, "Sawtooth reconnection," *Nuclear Fusion*, vol. 30, pp. 2545–2549, Dec 1990.

[66] L. Zakharov and B. Rogers, "Two-fluid magnetohydrodynamic description of the internal kink mode in tokamaks," *Physics of Fluids B: Plasma Physics*, vol. 4, no. 10, p. 3285, 1992.

[67] X. Wang and A. Bhattacharjee, "Nonlinear dynamics of the m=1 kink-tearing instability in a modified magnetohydrodynamic model," *Physics of Plasmas*, vol. 2, pp. 171–181, Jan 1995.

[68] Q. Qu, "A new theoretical model for fast sawtooth collapse," *Nuclear Fusion*, vol. 35, pp. 1012–1014, Aug 1995.

[69] F. D. Halpern, H. Lütjens, and J.-F. Luciani, "Diamagnetic thresholds for sawtooth cycling in tokamak plasmas," *Physics of Plasmas*, vol. 18, no. 10, p. 102501, 2011.

[70] J. McClenaghan, Z. Lin, I. Holod, W. Deng, and Z. Wang, "Verification of gyrokinetic particle simulation of current-driven instability in fusion plasmas. I. Internal kink mode," *Phys. Plasmas*, vol. 21, p. 122519, Dec 2014.

[71] R. B. White, P. H. Rutherford, P. Colestock, and M. N. Bussac, "Sawtooth stabilization by energetic trapped particles," *Physical Review Letters*, vol. 60, pp. 2038–2041, May 1988.

[72] V. S. Lukin, *Computational study of the internal kink mode evolution and associated magnetic reconnection phenomena*. PhD thesis, Princeton University, 2008.

[73] M. T. Beidler and P. A. Cassak, "Model for incomplete reconnection in sawtooth crashes," *Physical Review Letters*, vol. 107, Dec 2011.

[74] J. Stober, A. C. C. Sips, C. Angioni, C. B. Forest, O. Gruber, J. Hobirk, L. D. Horton, C. F. Maggi, M. Maraschek, P. Martin, *et al.*, "The role of the current profile in the improved H-mode scenario in ASDEX Upgrade," *Nuclear Fusion*, vol. 47, pp. 728–737, Jul 2007.

[75] C. C. Petty, J. E. Kinsey, C. T. Holcomb, J. C. DeBoo, E. J. Doyle, J. R. Ferron, A. M. Garofalo, A. W. Hyatt, G. L. Jackson, T. C. Luce, *et al.*, "High-beta, steady-state hybrid scenario on DIII-D," *Nuclear Fusion*, vol. 56, p. 016016, Dec 2015.

[76] G. Pereverzev and P. Yushmanov, "ASTRA Automated System for TRansport Analysis in a tokamak," tech. rep., Max-Planck-Institut für Plasmaphysik, Garching b. München, 2002.

[77] A. C. C. Sips, R. Arslanbekov, C. Atanasiu, W. Becker, G. Becker, K. Behler, K. Behringer, A. Bergmann, R. Bilato, D. Bolshukhin, *et al.*, "Steady state advanced scenarios at ASDEX Upgrade," *Plasma Physics and Controlled Fusion*, vol. 44, pp. B69–B83, Nov 2002.

[78] T. C. Luce, M. R. Wade, P. A. Politzer, S. L. Allen, M. E. Austin, D. R. Baker, B. Bray, D. P. Brennan, K. H. Burrell, T. A. Casper, *et al.*, "Long pulse high performance discharges in the DIII-D tokamak," *Nuclear Fusion*, vol. 41, pp. 1585–1599, Nov 2001.

[79] T. C. Luce, M. R. Wade, J. R. Ferron, A. W. Hyatt, A. G. Kellman, J. E. Kinsey, R. J. La Haye, C. J. Lasnier, M. Murakami, P. A. Politzer, *et al.*, "Stationary high-performance discharges in the DIII-D tokamak," *Nuclear Fusion*, vol. 43, pp. 321–329, Apr 2003.

[80] M. R. Wade, T. C. Luce, R. J. Jayakumar, P. A. Politzer, A. W. Hyatt, J. R. Ferron, C. M. Greenfield, M. Murakami, C. C. Petty, R. Prater, *et al.*, "Development, physics basis and performance projections for hybrid scenario operation in ITER on DIII-D," *Nuclear Fusion*, vol. 45, pp. 407–416, May 2005.

[81] E. Joffrin, A. C. C. Sips, J. F. Artaud, A. Becoulet, L. Bertalot, R. Budny, P. Buratti, P. Belo, C. D. Challis, F. Crisanti, *et al.*, "The hybrid scenario in JET: towards its validation for ITER," *Nuclear Fusion*, vol. 45, pp. 626–634, Jun 2005.

[82] S. Ide and the JT-60 Team, "Overview of JT-60U progress towards steady-state advanced tokamak," *Nuclear Fusion*, vol. 45, pp. S48–S62, Sep 2005.

[83] S. Günter, G. Giruzzi, A. Gude, R. J. L. Haye, K. Lackner, M. Maraschek, S. Schade, S. Sesnic, R. Wolf, Q. Yu, *et al.*, "MHD modes in regular and reversed shear scenarios and possibilities for their control through current drive," *Plasma Physics and Controlled Fusion*, vol. 41, pp. B231–B241, Dec 1999.

[84] K. McGuire, R. Goldston, M. Bell, M. Bitter, K. Bol, K. Brau, D. Buchenauer, T. Crowley, S. Davis, F. Dylla, *et al.*, "Study of high-beta magnetohydrodynamic modes and fast-ion losses in PDX," *Physical Review Letters*, vol. 50, pp. 891–895, Mar 1983.

[85] L. Chen, R. B. White, and M. N. Rosenbluth, "Excitation of internal kink modes by trapped energetic beam ions," *Physical Review Letters*, vol. 52, pp. 1122–1125, Mar 1984.

[86] N. Z. Taylor, T. C. Luce, R. J. La Haye, C. C. Petty, and P. Piovesan, "Magnetic flux conversion in the DIII-D high-beta hybrid scenario," in *58th Annual Meeting of the APS Division of Plasma Physics*, vol. 61, Oct 2016.

[87] T. A. Casper, R. J. Jayakumar, S. L. Allen, C. T. Holcomb, L. L. LoDestro, M. A. Makowski, L. D. Pearlstein, H. L. Berk, C. M. Greenfield, T. C. Luce, *et al.*, "Evidence for anomalous effects on the current evolution in the tokamak hybrid operating scenarios," *Nuclear Fusion*, vol. 47, pp. 825–832, Jul 2007.

[88] M. S. Chu, D. P. Brennan, V. S. Chan, M. Choi, R. J. Jayakumar, L. L. Lao, R. Nazikian, P. A. Politzer, H. E. S. John, A. D. Turnbull, *et al.*, "Maintaining the quasi-steady state central current density profile in hybrid discharges," *Nuclear Fusion*, vol. 47, pp. 434–442, Apr 2007.

[89] J. Garcia and G. Giruzzi, "Critical behavior of magnetically confined plasma regimes," *Physical Review Letters*, vol. 104, May 2010.

[90] R. E. Denton, J. F. Drake, and R. G. Kleva, "The m=1 convection cell and sawteeth in tokamaks," *Physics of Fluids*, vol. 30, no. 5, p. 1448, 1987.

[91] F. D. Halpern, D. Leblond, H. Lütjens, and J.-F. Luciani, "Oscillation regimes of the internal kink mode in tokamak plasmas," *Plasma Physics and Controlled Fusion*, vol. 53, p. 015011, Nov 2010.

[92] J. A. Breslau, M. S. Chance, J. Chen, G. Y. Fu, S. Gerhardt, N. Gorelenkov, S. C. Jardin, and J. Manickam, "Onset and saturation of a non-resonant internal mode in NSTX and implications for AT modes in ITER," *Nuclear Fusion*, vol. 51, p. 063027, May 2011.

[93] W. Shen, G. Y. Fu, B. Tobias, M. Van Zeeland, F. Wang, and Z.-M. Sheng, "Nonlinear hybrid simulation of internal kink with beam ion effects in DIII-D," *Physics of Plasmas*, vol. 22, p. 042510, Apr 2015.

[94] W. A. Cooper, J. P. Graves, A. Pochelon, O. Sauter, and L. Villard, "Tokamak magnetohydrodynamic equilibrium states with axisymmetric boundary and a 3D helical core," *Physical Review Letters*, vol. 105, Jul 2010.

[95] E. Strumberger, S. Günter, and C. Tichmann, "MHD instabilities in 3D tokamaks," *Nuclear Fusion*, vol. 54, p. 064019, May 2014.

[96] W. A. Cooper, J. P. Graves, and O. Sauter, "Helical ITER hybrid scenario equilibria," *Plasma Physics and Controlled Fusion*, vol. 53, p. 024002, Jan 2011.

[97] D. Brunetti, W. A. Cooper, J. P. Graves, F. Halpern, C. Wahlberg, H. Lütjens, and J. F. Luciani, "MHD properties in the core of ITER-like hybrid scenarios," *Journal of Physics: Conference Series*, vol. 401, p. 012003, Dec 2012.

[98] D. Brunetti, J. P. Graves, W. A. Cooper, and D. Terranova, "Ideal saturated MHD helical structures in axisymmetric hybrid plasmas," *Nuclear Fusion*, vol. 54, p. 064017, May 2014.

[99] F. L. Waelbroeck, "Nonlinear growth of the quasi-interchange instability," *Physics of Fluids B: Plasma Physics*, vol. 1, pp. 499–505, Mar 1989.

[100] Q. Yu, S. Günter, and K. Lackner, "Numerical modelling of sawtooth crash using two-fluid equations," *Nuclear Fusion*, vol. 55, p. 113008, Sep 2015.

[101] S. Migliuolo, "Theory of ideal and resistive m=1 modes in tokamaks," *Nuclear Fusion*, vol. 33, pp. 1721–1754, Nov 1993.

[102] W. Kerner, J. Goedbloed, G. Huysmans, S. Poedts, and E. Schwarz, "CASTOR: Normal-mode analysis of resistive MHD plasmas," *Journal of Computational Physics*, vol. 142, pp. 271–303, May 1998.

[103] E. Strumberger, S. Günter, P. Merkel, S. Riondato, E. Schwarz, C. Tichmann, and H. P. Zehrfeld, "Numerical MHD stability studies: toroidal rotation, viscosity, resistive walls and current holes," *Nuclear Fusion*, vol. 45, pp. 1156–1167, Sep 2005.

[104] E. Strumberger and S. Günter, "CASTOR3D: linear stability studies for 2D and 3D tokamak equilibria," *Nuclear Fusion*, vol. 57, no. 1, p. 016032, 2017.

[105] V. Igochine, A. Gude, S. Günter, K. Lackner, Q. Yu, L. Barrera Orte, A. Bogomolov, I. Classen, R. M. McDermott, N. C. Luhmann, *et al.*, "Conversion of the dominantly ideal perturbations into a tearing mode after a sawtooth crash," *Physics of Plasmas*, vol. 21, p. 110702, Nov 2014.

[106] V. Igochine, I. Classen, M. Dunne, A. Gude, S. Günter, K. Lackner, R. M. McDermott, M. Sertoli, D. Vezinet, M. Willensdorfer, *et al.*, "Tearing mode formation induced by internal crash events at different β_N," *Nuclear Fusion*, vol. 57, p. 036015, Jan 2017.